PhD Thesis

WAVELET ANALYSIS OF ULTRASONIC SIGNALS IN SOFT TISSUE STRUCTURE CHARACTERIZATION

Olga DOUBROVINA

Supervisor: dr. hab., prof. IPPT Barbara Gambin

Assistant supervisor: dr. inż Hanna Piotrzkowska–Wróblewska

Department of Ultrasound

Institute of Fundamental Technological Research,
Polish Academy of Sciences

Warsaw, 2019

I would like to express my sincere gratitude to

- *my supervisor, professor IPPT Barbara Gambin for the possibility of this work, for her extreme inspiration, comprehensive knowledge and research assistance;*
- *assistant supervisor dr. inż Hanna Piotrzkowska–Wróblewska for conducting joint experiments and for my new experience of problem solving as an engineer;*
- *professor Andrzej Nowicki, professor Janusz Wójcik, dr. Eleonora Kruglenko and the staff of the IPPT Ultrasound Department for the constructive discussions, possibility to use their experimental data in my investigations, new experience, and friendly atmosphere;*
- *professor Sergei V. Rogosin (Belarussian State University, Minsk, Belarus) for my research experience basics;*
- *professor Władimir Mitiuszew (Pedagogical University of Krakow) for the initial idea of this project;*
- *my husband and my parents for general optimism and believing in me.*

Abstract

The main thesis of the presented dissertation was to show that thanks to the use of the wavelet decomposition of the raw ultrasonic backscattered signals (called RF, radio frequency signals), several new markers characterizing the soft tissue scattering microstructure can be found. In addition, it should be emphasized that these markers were found not only from signals backscattered from phantoms made of tissue mimicking materials and from the signals backscattered from ex vivo tissue samples, but one of them was determined for signals backscattered from liver tissue in vivo. It is shown how this marker distinguished the healthy area of the liver tissue from the tumor area.

Two different ways of using the collected RF signals for wavelet analysis were used. The first way was based on the use of wavelet decomposition of the signal envelopes. The new markers associated with the different number of scatterers were found in the different wavelet decomposition levels of backscattered signals envelope statistical parameters. The studied echo signals were obtained from tissue mimicking materials made from agar-gel with glass microbeads. The relationship between changes in statistics of wavelet decomposition of signal envelope and the number of scatterers has been than used to develop a method for tracking temperature changes. So a new method of tracking temperature increase/decrease using statistical parameters of wavelet decomposition of the envelope of the backscattered signals was proposed. This method significantly reduces the amount of data processed in comparison with the analogous method using signal envelope statistics without wavelet decomposition.

In the second way, the wavelet decomposition of the RF signals themselves were used. It has been shown that determining the MSS parameter (mean scatterer spacing) from the wavelet decomposition of the RF signals clearly improves accuracy of other MSS estimates that directly use the signals properties. Additionally, it was shown that thanks to wavelet decomposition of signals the introduction of a "scale index" — a novel very fine measure of chaoticity degree of a structure — was possible. I shown that the scale index provided to the classification based on the increasing values of the parameter from the exact periodicity to the chaos hidden in the signal. In particular, by using this index regular pseudo-periodic structure in healthy human liver tissue in vivo was distinguished from the more chaotic tumor structure. It was done by the comparing of values of this index calculated from RF signals collected by radiologists for the healthy and the cancerous liver tissue areas. The result means, that this index treated as a new parameter in QUS

parametric maps constructions can be vitally useful in improving of cancer diagnostics and monitoring treatment response.

Streszczenie

Główną tezą prezentowanej rozprawy było pokazanie, że dzięki zastosowaniu dekompozycji falkowej ultradźwiękowych sygnałów RF (radio frequency) wstecznie rozproszonych w tkance mona znaleźć nowe markery (znaczniki, parametry) charakteryzujące mikrostrukturę tkanek miękkich. Należy podkreślić, że markery te znaleziono wykorzystując sygnały ultradźwiękowe rozproszone w fantomach wykonanych z materiałów naśladujących tkankę, sygnały rozproszone w próbkach tkanek ex vivo, a jeden z markerów został określony dla sygnałów rozproszonych w tkance wątroby in vivo. W tym ostatnim przypadku, pokazano jak marker ten odróżniałzdrowy obszar tkanki wątroby od obszaru guza.

Zastosowano dwa różne sposoby wykorzystania zebranych sygnałów RF do analizy falkowej. Pierwszy sposób polegałna wykorzystaniu dekompozycji falko-wej obwiedni sygnału. Nowe markery, czułe na liczbę rozpraszaczy w badanym materiale, zostały znalezione z parametrów statystycznych obwiedni sygnału wyznaczonych dla różnych poziomów dekompozycji falkowych.

W tym przypadku, badane sygnały echa otrzymano z materiałów naśladujących tkanki, wykonanych z żelu agarowego z mikro-kulkami szklanymi. Związek między zmianami w statystykach dekompozycji falkowej obwiedni sygnału a liczbą rozpraszaczy zostałużyty do opracowania metody śledzenia zmian temperatury. Zaproponowano nową metodę śledzenia wzrostu / spadku temperatury za pomocą parametrów statystycznych dekompozycji falkowej sygnałów rozproszonych. Ta metoda znacznie zmniejsza ilość przetwarzanych danych w porównaniu z analogiczną metodą wykorzystującą statystyki obwiedni sygnału bez rozkładu falkowego.

W drugim sposobie użyto dekompozycji falkowej samych sygnałów RF. Wykazano, że dokładność parametru MSS (mean scatterer spacing), oznaczającego średni odstęp między rozpraszaczami, wyznaczanego z sygnałów RF, wyraźnie rośnie po zastosowaniu dekompozycji falkowej. Dodatkowo wykazano, że dzięki dekompozycji sygnałów falkowych wprowadzenie "indeksu skali" — nowatorskiej bardzo dokładnej miary stopnia chaotyczności struktury — jest możliwe. Pokazano, że indeks skali opiera się na rosnących wartościach parametru, od dokładnej okresowości do chaosu ukrytego w sygnale. W szczególności, stosując ten wskaźnik, regularna pseudo-okresowa struktura w zdrowej ludzkiej tkance wątroby in vivo została odróżniona od bardziej chaotycznej struktury guza. Dokonano tego przez porównanie wartości tego wskaźnika obliczonych z sygnałów RF zebranych aparatem USG przez radiologów dla zdrowych i nowotworowych obszarów tkanki wątroby. Wynik oznacza, że ten wskaźnik traktowany jako nowy parametr w konstrukcjach map

parametrycznych tkanki, używanych w metodach ilościowych ultradźwięków QUS (quantative ultrasound), może być niezwykle przydatny w ulepszaniu diagnostyki raka i monitorowaniu odpowiedzi na leczenie.

Contents

List of Figures

List of Tables

Introduction

When an ultrasonic wave penetrates soft tissue, the local structure of tissue interacts with the mechanical energy of the wave so that, the energy absorption, reflection, and scattering appear. The energy propagated back toward the ultrasonic transducer constitutes the ultrasonic echo signal called the radiofrequency (RF) signal, [53]. The RF signal contains information about ultrasound and tissue interaction and a processing method must be used that can encode this information.

The amplitude is related to the distribution of mechanical impedance (density, elastic characteristics) of the backscattering medium, the scatterer concentration and the ratio between the sizes of the microstructure and the wavelength. The phase information, related to the interference, depends on the geometrical configuration of the tissue microstructure scatterers. These interference and reflectivity variations are registered in the time domain of received backscattered signals and are responsible for spectral amplitude modulation in the frequency domain. In this context, over the last thirty years quantitative ultrasound (QUS) techniques have been developed to improve tissue characterization for diagnostics made with the help of interpretation of B-mode (brightness mode) images, which is popular classical ultrasonography techniques [60]. Indeed, in order to gain further information for tissue characterization and differentiation purposes, it is essential not only to analyze the amplitude spatial distribution but also use the information given by the shape of the RF signal spectrum to identify the spectral parameters that are best correlated with the investigated structures.

Parametric ultrasonic imaging allows to choose characteristic features in echo signals dispersed backwards from different soft tissue structures, e.g. differentiation between neoplastic changes and other changes in soft tissues. Most of the research related to the determination of parameters for ultrasonic parametric imaging is based on a detailed analysis of B-mode images, which are normally available in commercial USG apparatus used for medical ultrasound diagnostics. The use of raw ultrasonic echo signals requires access to the special ultrasonic research equipment that allows acquisition of these signals in parallel with the simultaneous registration of classic, 2-dimensional B-mode images. The parametric maps corresponding to the specific properties of soft tissue areas created by the parameter values determined from the RF echo signal from these areas are built to improve the quality of diagnostics, i.e. the classification of tissue changes made by the physician. The next goal of using the maps is to create an automatic diagnostic system

(CAD) that eliminates human participation and at the same time improves the speed of cancer screening. Research based on the analysis of available RF signals collected in the Institute of Fundamental Technological Research with cooperation of physician radiologists thanks to possessing of research ultrasound equipment were the subject of three doctoral dissertations made in recent years in the Department of Ultrasound in the Institute. In the thesis of dr. inż H. Piotrzkowska-Wróblewska [56] based on RF signals recorded by dermatologists, in examination of the patients who were diagnosed with basal cell carcinoma and actinic keratosis, the shape parameter of K-distribution of echo signals envelopes were determined from areas of healthy tissue and tissue lesions. The differences in the value of this parameter were compared with the diagnosis made by physicians. In the thesis of dr. Z. Klimonda [41] the method of attenuation parameter determination was proposed and the attenuation coefficient values as the parameter of tissue differentiation was used. Tissue attenuation was estimated from backscattered echoes by tracking mean frequency changes with depth under assumption of linear relation between attenuation and frequency. The experimental data used for evaluation of the method in the thesis was numerically generated or collected from commercial phantoms with known material properties. In the thesis of dr. inż M. Byra [9] the homodyned K-distribution related to the tissue scattering properties was used for breast tissue characterization. The obtained breast lesion parametric maps were segmented to extract areas exhibiting similar scattering properties. Author showed that it was possible to improve the breast lesion classification performance by combining scattering and morphological features of areas of healthy tissue and lesions.

These three thesis, as they are available in the Internet and contain exhaustive number of references connected with ultrasound parametric imaging allow us to avoid the repeating a detailed discussion of the topic of ultrasonic parametric imaging.

Motivation of research. In the past, the author of the dissertation successfully dealt with the determination of changes in the fetal echo signal confirming the disease state, [10], [84]. At that time, the author used the method of wavelet analysis of collected signals and by identifying the statistical features of various levels of wavelet approximation features that optimally classify the fetus's condition were found.

Main idea of the thesis. This practically important result lay at the basis of main idea of this thesis, namely the use of wavelet analysis to look for a relationship between the properties of the tissue scattering structure, i.e. tissue morphology, with backscattered ultrasound echoes from this tissue. The improvement of the previously proposed QUS methods consists in im-

proving the accuracy of determining the already used parameters or finding new, hitherto unknown parameters related to the nature of the scattering of ultrasound signals in the tissues. Both approaches have been taken up in this thesis thanks to wavelet signal analysis application.

Calculations performed by mathematical software for engineers and scientists MatLab [48], release Matlab R2016a, lisence 282639-ACADEMIC) and by its efficient tool for wavelet analysis WaveToolbox [82].

Aims and arrangements of thesis

Basing on the two facts that

- ultrasound beams interact with scatterers in the tissue and
- backscattered signals contain information about weak diffuse subresolution scatterers (e.g. in liver tissue cells) and stronger non-diffuse scatterers (e.g. pseudo-periodic structure of lobule in liver tissue)

the thesis of this dissertation is formulated as following:

Thesis. To prove that by using wavelet distributions of the ultrasonic backscattered RF signals new markers (quantative parameters) characterizing the soft tissue scattering microstructure can be found.

The thesis is arranged in the following way:

Chapter 1 contains a general theoretical background of ultrasound signals generated by ultrasound transducers to study tissue structure properties. The nonlinear and linear theory of wave propagation: equation of wave propagation in inhomogeneous materials modelling soft tissues, absorption and problem of its non-classical description, formula of analytic signal, Hilbert transform of signal etc. are given. Because the wavelet transform in QUS methods are used rather for filtering the speckles from ultrasound images and it is very rarely used in QUS methods, we decided to include into the thesis elements of of wavelet theory, like discrete and continuous wavelet transforms, Daubechies wavelet family, and MRA (multiresolution analysis) which are applied in the dissertation. Simple examples of two signals containing two combinations of sine functions, their wavelet transform for comparison of wavelet decomposition and Fourier analysis was also added. The mathematical definition of chaoticity measure, a "scale index" based on a signal wavelet decomposition will be introduced. This Chapter also contains several formulae of statistical distributions: Gamma, K- and Nakagami, their PDF (probability density functions) which are used in this dissertation.

It should be remarked that Chapter 1 shows author's point of view as a mathematician on of the physical modelling. In particular, the chapter 1.3 about non-classical absorption contains the contribution in the form of proposing a new general equation containing fractional Laplace operators. This result (made with B. Gambin) ent. Viscosity and non-classical absorption of soft tissue described by fractional derivatives, was presented as a lecture during Ultrasound Imaging 31, Warsaw April 110-13, 2011. The theory of fractional derivatives was also the initial field of author's research activity ended with three published papers two in Russian journals and one in Springer journal [16].

In Chapter 2 a method of differentiating the density of scatterers by using the statistical properties of different wavelet approximation levels and the details coefficients of the Daubechies 6 family is used. The backscattered signals collected from three types of tissue mimicking agar-gel phantoms with glass beads with low density (6 items per mm^3), and high density (30 balls per mm^3) are compared. The parameters of different statistical distributions Gamma and Nakagami will be used to find the best possible way of differentiation of the scatterers densities. Additionally, the mean and standard deviation values of details coefficients of Daubechies 6th wavelet decomposition will be used to achieve the same goal.

Based on the result presented in Chapter 2 the statistical properties of the wavelet approximation of the signal envelope will be used to measure temperature changes in Chapter 3. As the temperature changes in tissues cause the spatial scatterers distribution variation the backscattered signals collected during heating reflect this variation. The statistical properties of backscattered signal envelope amplitudes modelled by K-distribution was already applied to track the temperature variations. The aim of wavelet approximations application to the temperature tracking is improving the method of temperature tracking by statistical parameter changes.

Chapter 4 will be devoted to the problem of the differentiation of scatterers' randomness type through numerical model of random structures. Because the inverse problem of wave propagation in random media cannot be solved analytically, only the numerical models containing generation of random media are the way which can be used for study the markers of scatterers distribution character from the known randomness structure. It was used used the MathCad software written by J. Wójcik to simulate different random media types and to obtain the backscattered signals from these media. The goal is to separate the randomness types of the media by the methods due to wavelet decomposition of the numerically simulated random signals. To this end I will use the scalograms of wavelet decompositions, simple statis-

tics of wavelet approximations and the values of a scale index introduced in subsection 1.4.4 for every random media type, i.e. for every scatterers distributions.

In Chapter 5 It will be shown how the collected RF signals backscattered from self-made "threads" phantom with periodic structure can be used for validation the improvement of accuracy of MSS (mean scatterer spacing) parameter determined from a special wavelet approximation level of RF signals. The treads are in three different environments, water, oil and the starch gel. The RF echo signals from these phantoms will be also used to validation of the scale index, the quantitative parameter introduced by us for the first time to ultrasound signal chaoticity analysis in Chapter 1.

Data sets containing signals from the the human liver samples, collected by radiologist in vivo, will be used in the analysis in Chapter 6. One dataset consists the regions of tumor, the second dataset consists from the other regions with the healthy tissue. The tumor area loses the regular structure that is usual for normal liver tissue, so this loss of regularities should be "visible" in the backscattered ultrasonic signals. It will be applied the "scale index" to classify the tissue areas as healthy or cancerous.

The bibliography contains 86 items.

Appendix A is devoted to the introduction to integral and discrete transforms and describes the procedure of multiresolution analysis.

Appendix B contains the introduction to the theory of wave propagation in random medium, namely, its mathematical model, stationary random process description, introduction to periodic and quasiperiodic media and waves propagation in randomly inhomogeneous medium.

Appendix C contains the author's list of publications and her scientific background.

Flowchart from Input-Information to Output-Area of Applications of Wavelets

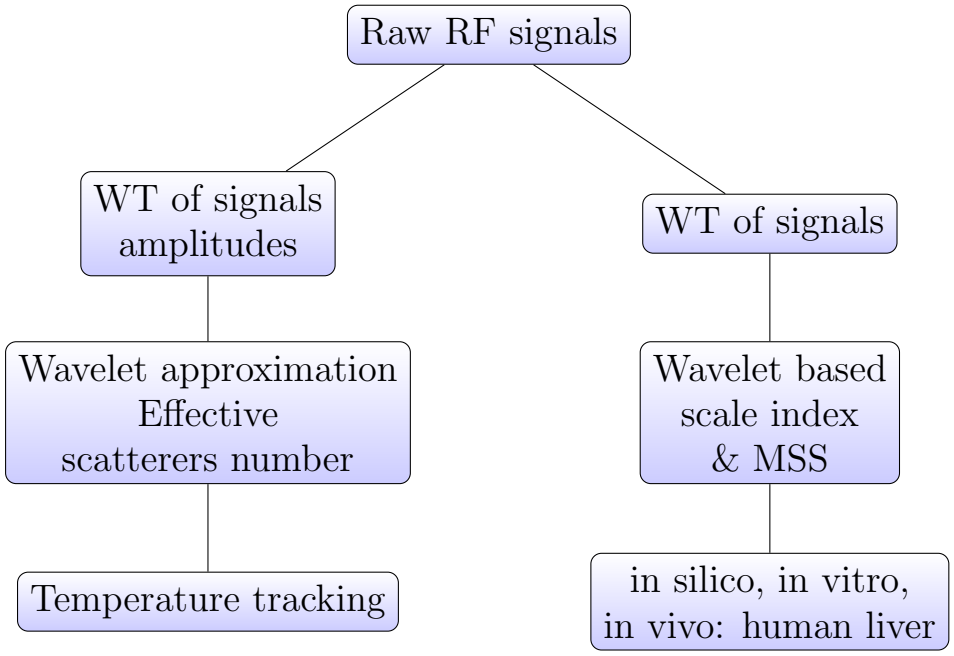

The following abbreviations are used:
RF — radio frequency,
WT — wavelet transform,
MSS — mean scatterer spacing.

1 General Theoretical Background

1.1 Acoustic Waves

In the thesis we analyze ultrasound signals, backscattered from soft tissues or from tissue mimicking materials (TMMs). Both of this media are randomly heterogeneous in their nature, the tissues contain huge number of components on different level of magnitudes, besides they contain more than 80% of water, TMMs are usually produced as a continuous matrix, e.g. agar-gel with oil, also containing more that 80% of water, with added dispersed different microparticles to ensure the TMM samples backscattering and other acoustical properties similar to the soft tissues. non-linear fluid dynamics is the starting point for the derivation of the acoustic wave equation in the soft tissue modeling fluid. The derived from general nonlinear equation the linearized equation of acoustic pressure waves will be further generalized to take into account the non-classical absorption and dispersion terms. The special mathematical notion of fractional derivative is introduced to obtain compatibility with the specific ultrasound attenuation frequency dependent properties characterizing tissue medium. Additionally, to describe the ultrasound backscattering pressure wave from the weakly inhomogeneous random medium two main assumptions are made: propagation is a linear one and the scattering is a "weak" scattering. We will obtain linear hyperbolic equation with "small" variable variable coefficients, which leads to the Born approximation valid. So, the scattered pressure can be obtained as a convolution of Green function for homogeneouse wave equation (with constant coefficients) and of a "source term". The source function is due to the presence of spatial local weak fluctuations in compressibility κ and density ρ of the medium.

1.1.1 A Nonlinear Acoustic Equation

We follow [44] to derive a nonlinear acoustic equation for scalar potential of velocity.

The fluid movement is defined as stationary movement relatively to the unperturbed medium coordinate system x, y, z and t, velocity field $\mathbf{u}(x, y, z)$ and the fields of the thermodynamic characteristics of the medium: pressure field $p(x, y, z, t)$, density $\rho(x, y, z, t)$, temperature $T(x, y, z, t)$ and entropy $s(x, y, z, t)$.

The system of equations of the dynamic of continuous media consist of four equations. First of them is the balance of mass equation

$$\frac{\partial \rho}{\partial t} + \nabla \cdot (\rho \mathbf{u}) = 0, \tag{1.1}$$

where $\cdot$ denotes the scalar product, ∇ is a gradient operator. The second is the motion equation

$$\rho\left(\frac{\partial \mathbf{u}}{\partial t}+(\mathbf{u}\cdot\nabla)\,\mathbf{u}\right)=-\nabla p+\eta\Delta\mathbf{u}+\left(\frac{\eta}{3}+\xi\right)\nabla\nabla\cdot\mathbf{u}, \tag{1.2}$$

where η and ξ are correspondent coefficients of shear and volume viscosity. The third one is the heat equation

$$\rho T\left(\frac{\partial s}{\partial t}+\mathbf{u}\cdot\nabla s\right)=\frac{\eta}{2}\left(\nabla\mathbf{u}+(\nabla\mathbf{u})^{T}-\frac{2}{3}\mathbf{I}\,(\nabla\cdot\mathbf{u})\right)^{2}++\xi\,(\nabla\mathbf{u})^{2}+\varkappa\nabla\nabla T, \tag{1.3}$$

where $\varkappa$ is a thermal conductivity coefficient and $\mathbf{I}$ denotes the unit tensor of the second order. And the last is the equation of state which for ideal gas has the form

$$p=\rho RT, \tag{1.4}$$

or, in terms of ρ and s it can be written as

$$p=\rho^{\gamma}R\exp\left(\frac{s-s_0}{C_v}\right), \tag{1.5}$$

where $\gamma=\dfrac{C_p}{C_v}$ is the ratio of the heat capacities of constant pressure and constant volume respectively, $R=C_p-C_v$ is a gas constant for the mass unit.

We will assume that the perturbations which are characterized by the fields of the pulsations of the hydrodynamic terms are small, i.e. $\dfrac{\rho-\rho_0}{\rho_0}\varepsilon$, $\dfrac{p-p_0}{p_0}\sim\varepsilon$, $\dfrac{u}{c_0}\sim\varepsilon$ and $\varepsilon<1$. Here ρ_0, p_0 and c_0 are correspondent nonperturbated quantities.

Using the linearization method it can be shown that all the media movements decay in the first-degree assumption to the three non-interacting components, namely incompressible vortical component which is described by the vortex field $\Omega(x,y,z,t)=\nabla\times\mathbf{u}(x,y,z,t)$, the entropy component $s(x,y,z,t)$ and potential or acoustic component which is connected with the pulsations of the potential part of velocity field $D(x,y,z,t)=\nabla\mathbf{u}(x,y,z,t)$, and the pressure pulsations $p(x,y,z,t)$.

We take into consideration only the potential (or acoustic) motions, i.e. that the condition $\nabla\times\mathbf{u}(x,y,z,t)=0$ is true. In such a way the vortex component and its interaction with other components are eliminated.

Under this assumption the equation (1.2) can be rewritten in a following form

$$\rho\left(\frac{\partial \mathbf{u}}{\partial t}+\frac{1}{2}\nabla u^2\right)=-\nabla p+\left(\frac{4}{3}\eta+\xi\right)\Delta\mathbf{u}. \tag{1.6}$$

This equation may be simplified by introducing a new variable δ which is connected viscous and thermal coefficients. If we assume that all the fields are periodic functions depending on space variables with given wave vector $\mathbf{k}$, then the linearized equations will have the dimensionless quantities $\delta = \frac{k}{c_0\rho_0}\left(\frac{4}{3}\eta+\xi\right)\equiv\frac{k}{c_0\rho_0}b_1$, $\pi=\frac{c_p}{\varkappa}b_1$. We take into account the members ε, ε^2, $\delta\varepsilon$ and neglect the other. In the heat equation (1.3) we omit $\mathbf{u}\nabla s$ and all the members which have viscous coefficients of the third order of $\delta\varepsilon^2$ and exclude the temperature using (1.4). In that case the equation (1.3) has the form

$$\frac{\partial s}{\partial t}=\frac{p}{\varkappa}\Delta\left(\frac{p}{\rho}\right) \tag{1.7}$$

For the small changes of the state we may have only the following terms of the series

$$p-p_0=c_0^2(\rho-\rho_0)+\frac{\gamma-1}{2\rho_0}c_0^2(\rho-\rho_0)^2+c_0^2\frac{\rho_0}{\gamma C_v}(s-s_0)+\cdots, \tag{1.8}$$

where $c_0=\sqrt{\frac{\gamma p_0}{\rho_0}}$ is the adiabatic velocity of sound. The entropy changing has the second order of $\delta\varepsilon$, as it follows from (1.7).

Now we will exclude the pressure form the formulae (1.6) and (1.7), preserving only the terms of the second order of ε^2 and $\delta\varepsilon$.

$$\begin{aligned}\frac{\partial \mathbf{u}}{\partial t}=-\frac{1}{2}\nabla u^2-\frac{c_0^2}{\rho_0}\nabla\left((\rho-\rho_0)+\frac{\gamma-2}{2\rho_0}(\rho-\rho_0)^2+\frac{\rho_0}{\gamma C_v}(s-s_0)\right)+\\ \frac{1}{\rho_0}\left(\frac{4}{3}\eta+\xi\right)\Delta\mathbf{u},\end{aligned} \tag{1.9}$$

$$\frac{\partial s}{\partial t}=\frac{\varkappa(\gamma-1)}{\rho_0^2}\Delta\rho. \tag{1.10}$$

Differentiating the equation (1.9) by time and substituting there expression (1.10) we obtain

$$\begin{aligned}\frac{\partial^2 \mathbf{u}}{\partial t^2}=-\frac{1}{2}\nabla\frac{\partial}{\partial t}u^2-\frac{c_0^2}{\rho_0}\nabla\left(\frac{\partial\rho}{\partial t}+\frac{\gamma-2}{2\rho_0}\frac{\partial}{\partial t}(\rho-\rho_0)^2+\right.\\ \left.+\frac{\varkappa}{\rho_0}\left(\frac{1}{C_v}-\frac{1}{C_p}\Delta\rho\right)\right)+\frac{1}{\rho_0}\left(\frac{4}{3}\eta+\xi\right)\frac{\partial}{\partial t}\Delta\mathbf{u},\end{aligned} \tag{1.11}$$

After introducing the scalar potential $\mathbf{u}(x,y,z,t) = -\nabla\Phi(x,y,z,t)$ the equation (1.11) can be derived to the form

$$\begin{aligned}\frac{\partial^2\Phi}{\partial t^2} = \frac{1}{2}\frac{\partial}{\partial t}(\nabla\Phi)^2 + \frac{c_0^2}{\rho_0}\frac{\partial\rho}{\partial t} + c_0^2\frac{\gamma-2}{2\rho_0}\frac{\partial}{\partial t}(\rho-\rho_0)^2 + \\ + \frac{c_0^2\varkappa}{\rho_0^2}\left(\frac{1}{C_v}-\frac{1}{C_p}\right)\Delta\rho + \frac{1}{\rho_0}\left(\frac{4}{3}\eta+\xi\right)\frac{\partial}{\partial t}\Delta\Phi.\end{aligned} \tag{1.12}$$

Then, using equalities (1.1) and (1.2) we will obtain the equation

$$\frac{\partial^2\Phi}{\partial t^2} - c_0^2\Delta\Phi = \frac{\partial}{\partial t}\left(b\Delta\Phi + (\nabla\Phi)^2 + a\left(\frac{\partial\Phi}{\partial t}\right)^2\right), \tag{1.13}$$

where $a \equiv \dfrac{\gamma-1}{2c_0^2}$, $b \equiv \dfrac{1}{\rho_0}\left(\dfrac{4}{3}\eta + \xi + \varkappa\left(\dfrac{1}{C_v}-\dfrac{1}{C_p}\right)\right)$.

The above equation (1.13) is called a nonlinear acoustic equation. The examples of such equations in one-dimensional case and the forms of their solutions are given in [44].

J. Wójcik proposed a transition to dimensionless quantities [81] by the substitutions

$$t = \omega_0 t',\ \mathbf{x} = k_0\mathbf{x}',\ \partial_t = \frac{1}{\omega_0}\partial_t',\ \nabla = \frac{1}{k_0}\nabla',$$

$$k_0 = \frac{\omega_0}{c_0},\ q = \frac{P_0}{\rho_0 c_0^2},\ \mathbf{v} = \frac{\mathbf{v}'}{v_0},$$

$$v_0 = \frac{P_0}{\rho_0 c_0} = qc_0,\ \Phi = \frac{\Phi'}{\Phi'_{nor}},\ \Phi'_{nor} = \frac{P_0}{\rho_0\omega_0},$$

$$\omega_0 = \frac{2\pi}{T_0} = 2\pi f_0.$$

Modifying equation (1.13) we have

$$\omega_0^2\frac{\partial^\Phi}{\partial t^2}\left(\frac{P_0}{\rho_0}\omega_0\right) - c_0^2\frac{\omega_0 P_0}{\rho_0 c_0^2}\Delta\Phi =$$

$$= \omega_0\frac{\partial}{\partial t}\left[b\frac{P_0}{\rho_0\omega_0}\frac{\omega_0^2}{c_0^2}\Delta\Phi + \frac{\omega_0^2}{c_0^2}\frac{P_0^2}{\rho_0^2\omega_0^2}(\nabla\Phi)^2 + a\frac{P_0}{\rho_0}\omega_0^2\frac{\partial\Phi}{\partial t}\right].$$

As $\dfrac{\omega_0 P_0}{\rho_0} \neq 0$, $q = \dfrac{P_0}{\rho_0 c_0^2}$, and $a\omega_0 = \dfrac{\gamma-1}{2}q$ we obtain

$$\frac{\partial^2\Phi}{\partial t^2} - \Delta\Phi = \frac{\partial}{\partial t}\left[b\frac{\omega_0}{c_0^2}\Delta\Phi + (\nabla\Phi)^2 + q\frac{\partial\Phi}{\partial t}\right]. \tag{1.14}$$

1.1.2 Linear Acoustic Waves and Background of Ultrasound Pulse Scattering in Tissue

The linearization of state equation of fluid and assuming that we exclude the heating generation due to sound effects (lossless model) the equation (1.13) can be linearized. If we assume that the inhomogeneous medium is infinite and it is of constant compressibility and density with embedded inside a scattering region V where the inhomogenities are concentrated, it can be modelled by the following equation [36]

$$\nabla^2 p - \frac{1}{c_0^2}\frac{\partial^2 p}{\partial t^2} = \frac{1}{c_0^2}\frac{\partial^2 p}{\partial t^2}\gamma\left(\mathbf{r}\right)) + \nabla \cdot \left(\mu\left(\mathbf{r}\right)\nabla p\right), \tag{1.15}$$

where $\gamma\left(\mathbf{r}\right) = \dfrac{\kappa(\mathbf{r}) - \kappa_0}{\kappa_0}$, $\kappa(\mathbf{r})$ is variable compressibility for $\mathbf{r} \in V$, $\kappa\left(\mathbf{r}\right) = \kappa_0$ for $\mathbf{r} \notin V$, $\mu\left(\mathbf{r}\right) = \dfrac{\rho(\mathbf{r}) - \rho_0}{\rho_0}$, $\rho(\mathbf{r})$ is variable density and $\mathbf{r} \in V$, $\rho\left(\mathbf{r}\right) = \rho_0$ for $\mathbf{r} \notin V$, c_0, κ_0, ρ_0 are acoustic velocity, constant compressibility and constant density in the embedding region respectively, $\kappa_0 = \dfrac{1}{\rho_0 c_0^2}$, $p = p\left(\mathbf{r}, t\right)$ is the pressure field, ∇ denotes gradient in a space variable, ∇^2 denotes Laplacian operator and $(\cdot)$ denotes full contraction.

In this section we repeat the ideas given in paper [36]. Equation (1.15) can be written in an equivalent form of integro-differential equation with the use of 3D Green function $g(\mathbf{r}, t)$, i.e. a solution to the wave equation with the impulsive point source. If we denote by R_{hs} the differential operator acting on the pressure in the right hand side of Eq. (1.15) the integro-differential equation takes the form

$$p\left(\mathbf{r}, t\right) = -\int\int g\left(\mathbf{r}, t; \mathbf{r}', t'\right) R_{hs}\left(p\left(\mathbf{r}', t'\right)\right) d^3\mathbf{r}' dt'. \tag{1.16}$$

Strongly reflecting surfaces are excluded from region of interest (ROI). Besides assuming the "weak" inhomogenities, i.e. coefficients γ and μ are both small in comparison to unity, the assumption of weak scattering, i.e. excluding multiple scattering effects (Born approximation), is made. So, the total pressure can be split into sum of incident and scattering field $p = p_i + p_s$, where p_i and p_s denotes incident and scattered pressure, respectively. It implies that the incident pressure may be used as a source function in the right hand side of the integro-differential equation (1.16) which now stands as the equation for the backscattered pressure field:

$$p_s(\mathbf{r},t) = -\int\int g(\mathbf{r},t;\mathbf{r}',t')\, R_{hs}(p_i(\mathbf{r}',t'))\, d^3\mathbf{r}'dt'. \tag{1.17}$$

For the well known form of 3D Green function

$$g(\mathbf{r},t;\mathbf{r}',t') = \frac{\delta\left(t-t'-\frac{1}{c_0}|\mathbf{r}-\mathbf{r}'|\right)}{4\pi|\mathbf{r}-\mathbf{r}'|},$$

the equation (1.17) takes the form

$$\begin{aligned} p_s(\mathbf{r},t) = -\int\int & \frac{\delta\left(t-t'-\frac{1}{c_0}|\mathbf{r}-\mathbf{r}'|\right)}{4\pi|\mathbf{r}-\mathbf{r}'|}\cdot \\ \cdot & \left[\frac{1}{c_0^2}\frac{\partial^2 p_i(\mathbf{r}',t')}{\partial t'^2}\gamma(\mathbf{r}') + \nabla\cdot(\mu(\mathbf{r}')\nabla p_i(\mathbf{r}',t'))\right] d^3\mathbf{r}'dt'. \end{aligned} \tag{1.18}$$

A representation of the incident pressure p_i generated by a pulse-echo ultrasonic scanner, for a pulse propagation with fixed shape and group velocity v in the direction Oz using a cylindrical coordinate system (h,θ,z) located in the origin at $t=0$ is

$$p_i(\mathbf{r}',t) = a(z-vt)b(h)e^{ik_0(z-vt)}, \tag{1.19}$$

where a describes the axial pulse shape, $b(h)$ describes the beam profile which is assumed to be axially symmetric, and k_0 is the magnitude of the wave vector corresponding to the carrier frequency of the pulse. A Gaussian pulse of the form $a(z) = \begin{cases} a_0\frac{z}{\alpha}e^{-\frac{z}{\alpha}}, & z>0, \\ 0, & \text{otherwise} \end{cases}$, where a_0 and α are constants, $b(h) = e^{-\beta^2h^2}$, $\beta>0$ is constant, is a good approximation for pulse emitted by a clinical scanner.

Alternatively, it may be considered that the incident pulse is a superposition of travelling plane waves spread about the carrier wave vector $\mathbf{k_0}$:

$$p_i(\mathbf{r}',t) = \int\int G(\mathbf{k}'-\mathbf{k_0})e^{i(\mathbf{k}'\cdot\mathbf{r}-\omega' t)}d^3\mathbf{k}'d\omega'. \tag{1.20}$$

Using a cylindrical coordinate system with axis Oz oriented along $\mathbf{k_0}\equiv(0,0,k_0)$, and assuming the axial symmetry and a separable spectrum factorized by two functions of scalar variables k and η

$$G(\mathbf{k}-\mathbf{k}_0) = A(k-k_0)B(\eta),$$

the following correspondence may be obtained: $v = c_0$, $a(z) = \int\limits_{-\infty}^{\infty} A(k)e^{ikz}dk$, $b(h) = 2\pi \int\limits_{0}^{\infty} B(\eta)J_0(\eta h)d\eta$, where $J_0(\cdot)$ is zero-order Bessel function of the first kind. Substitution of the expression for the incident pressure into the scattering integral (1.18) enables to find the backscattered pressure. Next, it is also assumed that the observation point R is distant from the scattering region and a Fraunhofer approximation holds, so that $|\mathbf{R} - \mathbf{r}'| \sim R + z$ and $\dfrac{1}{|\mathbf{R} - \mathbf{r}'|} \sim \dfrac{1}{R}$. In the further used software (see Chapter 5), the scatterers properties differs in density and in compressibility from properties of the host medium. If variations in compressibility of scatterers are larger than the variation in density, what is often assumed for the real soft tissue properties, than ignoring the second-order terms in the right-hand side of equation (1.18) depending on the density, i.e. to take $\mu(h, \theta, z) = 0$, the integral (1.18) can be evaluated to find a backscattered pressure

$$p_s(R,t) = \frac{1}{4\pi R}\int_0^{\infty} \eta d\eta \int_0^{2\pi} d\phi \int_{-\infty}^{\infty} dk \int_0^{\infty} hdh \int_0^{2\pi} d\theta \cdot$$

$$\int_{-\infty}^{\infty} dz A(k-k_0)\cdot B(\eta)k^2\gamma(h,\theta,z)e^{i\eta h\cos(\phi-\theta)}e^{2ik(R+z)-c_0kt} =$$

$$= \frac{1}{4\pi R}\int k^2dk \int hdh \int dz \int d\theta A(k-k_0)b(h)\gamma(h,\theta,z)e^{ik(2z+2R-c_0t)}.$$

By introducing the notation $\Gamma(2k) = \int_{-\infty}^{\infty} \dfrac{1}{2\pi}\int_0 2\pi d\Theta \int_0^{\infty} dh\, hb(h)\gamma(h,\theta,z)$, the reduced equation is obtained

$$p_s(R,t) = \frac{1}{2R}\int_{-\infty}^{\infty} dkA(k-k_0)k^2\Gamma(2k)e^{ik(2R-c_0t)}.$$

The Fourier transform of the backscattered wave is

$$P_s(R,k) = \frac{1}{2Rc_0}k^2A(k-k_0)\Gamma(2k)e^{2ikR}.$$

The backscattered echoes depend not only on the intrinsic properties of the tissue itself but also on the interrogating pulse. Insight into this problem can be gained by assuming a specific model for the compressibility fluctuation $\gamma(h, \theta, z)$, and then determining what information about γ can be derived

from the backscattered echo train $p_s(R,t)$. The model is array of N discrete scatterers with $\gamma(h,\theta,z) = \sum_{i=1}^{N} \gamma_i \delta(h-h_i, \theta-\theta_i, z-z_i)$ thus

$$p_s(R,t) = \frac{1}{4\pi R} \sum_{i=1}^{N} \gamma_i b(h_i) \int A(k-k_0) e^{iR\phi_i} dk.$$

For tissues having a structural organization the order of ultrasonic wavelength $\lambda = \dfrac{2\pi}{k_0}$ it is used the model of an isotropically semi-regular array of point scatterers. For a regular array of scatterers with separation d, the phase difference between two adjacent scatterer is $\phi = k \cdot \Delta r = 2kd$. For $\phi = n\pi$ or $n\lambda = 2d$ where n is an integer, there will be constructive interference where the total scattered wave will be N (the number of scatterers per sample volume) times the wave scattered by a single inhomogenity. If the insonification is by a pulse of ultrasonic energy, then there is no longer a single wavelength λ_0, but rather a distribution of wavelengths $P_\Lambda(\lambda)$ and a corresponding distribution of frequencies $P_F(f)$. There will still be constructive interference for λ such that $\lambda = \dfrac{2d}{n}$ and varying amounts of constructive and destructive interference for other wavelength. The frequency spectrum of the backscattered signal will show peaks at frequencies $f = \dfrac{nc}{2d}$. That is, the resulting spectrum will have periodic peaks with period $\Delta f = \dfrac{c}{2d}$. We get

$$P_s(R,k) = \frac{1}{2Rc_0} A(k-k_0)\Gamma(2k) e^{2ikR},$$

where $\Gamma(2k) = \sum_i \gamma_i b(h_i) e^{2ikd_i}$, and i denotes the index of the scatterers in the volume.

This may be modelled as the superposition of peaks and nulls on the frequency spectrum of the ultrasonic scanner system, i.e.

$$P_s(f) = \Gamma(f) F_s(f) = \sum_i e^{(2\pi i/c) d_i 2f} \gamma_i b_i F_s(f),$$

where $P_s(f)$ is the system of frequency spectrum including the effect of overlying tissue and i indexes the scatterers in the sample volume.

We have not succeeded in totally separating out the system effects from the tissue in $\Gamma(2k)$ since it includes weighting from the scatterer's position in the beam profile but, as we will not be attempting to estimate the γ_i; values but only the separations d_i, we can lump the γ_i and b_i together. Periodic

peaks in the returned spectrum can be assigned to spatial structure in tissue since the system response is a smooth function and the effect of overlying tissue is an exponential attenuation of the form $e^{-\alpha f^x R}$ where f is frequency, α and x are constants, and R is the distance traveled through the overlying tissue. In the case of a regular array of scatterers it is clear that only the magnitude of the frequency spectrum $|P(f)|$ is required to determine the spatial separation d from the periodic peaks in the spectrum. Autocorrelation of $|P(f)|$, denoted by $|P(f)| \star |P(f)|$, will result in a function having a first peak at $\frac{c}{2d}$, corresponding to the frequency interval of the peaks in $|P(f)|$. In the case of a semiregular array of scatterers, as one would expect for some actual tissues, there is a distribution of spacings $Po(d)$ and a resultant broadening of the autocorrelation peaks. In tissue, the function $Po(d)$ may be expected to vary spatially. As the sample volume is moved throughout the tissue, the resulting $|P(f)| \star |P(f)|$ will vary accordingly. As it was already noticed the above section was rewritten from the paper [36] to give among others the main idea how to deal with scatterer periodic organization if the distance between scatterers is of the wave length order, we follow the idea in section 1.4.5 Improvement of Mean Scatterer Spacing Parameter.

1.2 Non-Cassical Absorption

The phenomenon of absorption of an acoustic energy carried by the ultrasonic wave in living soft tissue has a different character than in inanimate matter — solids or in liquids. Some acoustic energy, like in other viscous materials, turns into heat due to the so-called internal friction. However, some energy is consumed in the processes of biochemical reactions continuously present in a living organism or is converted into kinetic /electromagnetic energy of substractures. The internal structure of the tissue material is random and extremely complicated on infinitely many levels, indeed has a fractal nature. It is extremely interesting question of what part of energy is dissipated into heat and what part is involved in biological processes. To find the answer to the question one should know firstly, details of acoustic wave propagation and secondly, one should evaluate the amount of heat which, in principle, can be measured during ultrasound sonification by e.g. MR (magnetic resonance) technique. Modelling and evaluation of thermal processes during ultrasonic irradiation of soft tissue are studied inter alia in [23], [24], [49], [50]. Also in Chapter 3, Temperature Changes Differentiation, one of a ultrasonic method of temperature tracking is used.

Let us remind some biological facts of the complexity of tissue structure

which starts from the level of a cell dimension. Cell is the jelly-like matrix, called cytoplasm, that is bounded by the cell membrane. Cytoplasm is surrounding the nucleus of a cell. The cells includes also other organelles as well as the sugars, amino acids, and proteins that the cell uses for growth and reproduction. Organelles have themselves internal structures, the biggest of them is the nucleus, which is spheroidal in shape and separated from the cytoplasm by a double-membrane structure called the nuclear envelope. The cell membrane itself consists of a lipid bilayer with embedded proteins, etc. On the nano level the cytoplasm appears as a three-dimensional lattice of thin protein-rich strands known as the microtrabecular lattice (MTL), which serves to interconnect and support the other solid structures in the cytoplasm. Cytoplasm is also the home of the cytoskeleton, a network of cytoplasmic filaments responsible for the movement of the cell and which gives the cell its shape. The proper model for the acoustic wave propagation in such complicated structure of tissue needs a special attention. Let us underline that the wavelength of material particles movement under the action of ultrasound of MHz frequency pressure waves is of the order of nanometers, it means that such a mechanical "nano - movement" may be important in explaining the beneficial effects of ultrasound on healing processes or pain treatment by ultrasound sonication.

Absorption of acoustical energy in living tissues is due to:

1. viscosity of particles movement;

2. heat losses caused by heat conductivity;

3. conversion of energy into biochemical type.

The wave attenuation during tissue penetration loss their amplitude as a function of the direction of propagation like $A(t) = e^{-\overline{\alpha(\omega)}z}$, where $\overline{\alpha}(\omega) = \alpha(\omega) + b(\omega)$. The absorption power low in soft tissue is $\alpha(\omega) = \alpha_0(\omega^y)$, where $\alpha(\omega)$ is absorption coefficient measured in $Np\left(\frac{rad}{s}\right)^{-y} m^{-1}$, $b(\omega)$ is a scattering coefficient and ω is radial frequency measured in $\frac{rad}{s}$, $1 \leq y \leq 1.5$.

To take into account the special absorption power law J. Wócik [81] had introduced a new type of term by substitution in equation (1.14) the term $-b\frac{\omega_0}{c_0^2}\Delta$ by the non-local operator $\mathcal{A}$ and investigated the equation

$$\frac{\partial^2 \Phi}{\partial t^2} - \Delta\Phi = \frac{\partial}{\partial t}\left[2\mathcal{A}\Phi + q\left(\nabla\Phi\right)^2 + q\frac{\gamma - 1}{2}\left(\frac{\partial\Phi}{\partial t}\right)^2\right]. \tag{1.21}$$

One-dimentional example from [81] reads

$$\mathcal{A}\Phi = -\alpha_1 \frac{1}{\pi}\partial_z \int_{-\infty}^{\infty} \frac{\Phi(s,t)}{s-z} ds = -\alpha_1 \partial_z \hat{H}[\Phi], \tag{1.22}$$

here $\hat{H}[\Phi]$ defines a Hilbert transform. For a plane wave we get the dispersion equation

$$K_z^2 - \omega^2 - i2\omega\alpha_1 K_z sgn(k_z) = 0.$$

Dispersion relation can be obtained by two approaches.

The first approach. Let us define a more general form of the operator $\mathcal{A}$ in equation 1.14

$$\frac{\partial^2 \Phi}{\partial t^2} - \Delta\Phi = \frac{\partial}{\partial t}\left[D^y \Phi + q\left(\nabla\Phi\right)^2 + q\frac{\partial \Phi}{\partial t}\right]. \tag{1.23}$$

using Liouville fractional derivatives on half-axis and whole real axis [67] of order y introduced below:

$$\left(D_+^y \varphi\right)(x) = \frac{1}{\Gamma(1-y)}\frac{d}{dx}\int_{-\infty}^{x} \frac{\varphi(x')}{(x-x')^y} dx', \ -\infty < x < \infty \tag{1.24}$$

$$\left(D_-^y \varphi\right)(x) = -\frac{1}{\Gamma(1-y)}\frac{d}{dx}\int_{x}^{\infty} \frac{\varphi(x')}{(x-x')^y} dx', \ -\infty < x < \infty \tag{1.25}$$

$0 < y < 1$.

$$\left(D_\varphi^y\right)(x) = \frac{1}{\Gamma(1-y)}\frac{d}{dx}\int_{-\infty}^{\infty} \frac{\varphi(x')}{(x-x')^y} dx', \ -\infty < x < \infty. \tag{1.26}$$

If $y \geq 1$ then we assume correspondingly

$$\left(D_\pm^y \varphi\right)(x) = \frac{(-1)^n}{\Gamma(n-y)}\frac{d^n}{dx^n}\int_{0}^{\infty} x'^{n-y-1}\varphi(x \mp x') dx', \ \ n = [y]+1 \tag{1.27}$$

$$\left(D_\pm^y \varphi\right)(x) = \frac{(-1)^n}{\Gamma(n-y)}\frac{d^n}{dx^n}\int_{-\infty}^{\infty} x'^{n-y-1}\varphi(x \mp x') dx', \ \ n = [y]+1 \tag{1.28}$$

Function φ here belongs to the Lebesque class $L^p(R^1)$ (or to the weighted class $L^p(R^1;\rho)$), $1 < p < \dfrac{1}{y}$ or to the Holder class vanishing in $\pm\infty$.

These operators (1.24) – (1.26) will be bounded acting from the space $L^p(R^1)$ to the $L^q(R^1)$ ([67]), where $1 < p < \dfrac{1}{y}$ and $q = \dfrac{p}{1-yp}$.

We consider the linear reduced equation (1.14) in the form

$$\frac{\partial^2 \Phi}{\partial t^2} - \Delta \Phi = \frac{\partial}{\partial t} D^y \Phi. \tag{1.29}$$

Only linear parts use the properties of Fourier transforms fractional derivatives ([67]):

$$\mathcal{F}\left(D_{\pm}^{y} \varphi\right) = (\mp ix)^y \, \hat{\varphi}(x), \quad Re\, y \geq 0, \tag{1.30}$$

$$\mathcal{F}\left(D_{\infty}^{y} \varphi\right) = (\mp ix)^y \, \hat{\varphi}(x), \quad Re\, y \geq 0. \tag{1.31}$$

We obtain the nonlinear dispersion equation

$$k^2 - \omega^2 = 2i\alpha_1 \omega (ik)^y \tag{1.32}$$

or

$$k_r^2 - k_i^2 + 2ik_r k_i - \omega^2 = 2i\alpha_1 \omega k_r^y \left(i + \frac{k_i}{k_r}\right)^y.$$

After linearization of (1.32)

$$k_r^2 - k_i^2 + 2ik_r k_i - \omega^2 = 2i\alpha_1 \omega k_r^y \left(i + \frac{k_i}{k_r}\right).$$

This equation may be reduced to a system

$$\begin{cases} k_r^2 - k_i^2 - \omega^2 = -2\alpha_1 \omega k_r^y, \\ k_r k_i = \alpha_1 \omega k_r^y \dfrac{k_i}{k_r}. \end{cases}$$

Thus

$$k_r = \frac{1}{(\alpha_1 \omega)^{2-y}}, \;\; k_i^2 = 2(\alpha_1 \omega)^{(2-y)^2} + (\alpha_1 \omega)^{2(2-y)} - \omega^2.$$

where k_r is a real part of wave vector and k_i is an imaginary part.

The second approach. Let us define a more general form of the operator $\mathcal{A} = (-\Delta^2)^{y/2}$, than equation 1.14 reads

$$\frac{\partial^2 \Phi}{\partial t^2} - \Delta \Phi = \frac{\partial}{\partial t} \left[(-\Delta^2)^{y/2} \Phi + q \left(\nabla \Phi\right)^2 + q \frac{\partial \Phi}{\partial t} \right]. \tag{1.33}$$

Here $(-\Delta^2)^{y/2}$ is defined as a Riesz integro-differential operator [67]

$$(-\Delta)^{-y/2} = \mathcal{F}^{-1}|x|^{-y}\mathcal{F}\varphi = \begin{cases} I^y(\varphi), & Re\, y > 0, \\ D^{-y}(\varphi), & Re\, y < 0, \end{cases} \tag{1.34}$$

In one-dimensional case the operator $(-\Delta)^{y/2}$ is written as follows

$$(-\Delta)^{y/2} = \\ = \begin{cases} I^y(\varphi) = \dfrac{1}{\Gamma(y)} \displaystyle\int_x^{+\infty} \frac{\varphi(x')}{(x-x')^y} dx', -\infty < x < \infty, \ Re\, y > 0, \\ D^{-y}(\varphi) = \dfrac{1}{\Gamma(1-y)} \dfrac{d}{dx}, \displaystyle\int_x^{+\infty} \frac{\varphi(x')}{(x-x')^y} dx', -\infty < x < \infty, \ Re\, y < 0, \end{cases} \tag{1.35}$$

Using the following property of Fourier transform

$$\mathcal{F}\left(\left(-\frac{\partial^2}{\partial x^2}^{y/2}\right)\right) = \left(-(-ik)^2\right)^{y/2} = k^y,$$

we get the dispersion relation

$$k^2 - \omega^2 = 2i\alpha_1 \omega k^y \tag{1.36}$$

or

$$k_r^2 - k_i^2 + 2ik_r k_i - \omega^2 = 2i\alpha_1 \omega {k_r}^y \left(1 + i\frac{k_r}{k_i}\right)^y.$$

Assuming $k_r >> k_i$ and linearize it we will have

$$k_r^2 - k_i^2 + 2ik_r k_i - \omega^2 = 2i\alpha_1 \omega k_r^y \left(1 + i\frac{k_r}{k_i}\right).$$

which may be reduced to a system

$$\begin{cases} k_r^2 - k_i^2 - \omega^2 + 2\alpha_1 \omega {k_r}^y \dfrac{k_i}{k_r} = 0, \\ k_r k_i = \alpha_1 \omega k_r^y. \end{cases}$$

$$k_i = \alpha_1 k_r^{y-1},$$

k_r may be found from the equation

$$2\alpha_1^2 \omega^2 k_r^{y-2} - \alpha_1^2 \omega^2 k_r^{2(y-1)} + k_r^2 = \omega^2.$$

Now, let show the other than previously presented methodology of modeling the lossy medium. In the paper of [14] general form of linear wave equation in lossy medium (lossy wave equation) was proposed

$$\frac{1}{c_0}\frac{\partial^2 p}{\partial t^2} = \nabla^2 p + \tau \Pi p. \tag{1.37}$$

Here p is acoustical pressure, c_0 is wave velocity, Π is differential operator of the order $y-1$ (y is exponent in the power low), τ coefficient of the proportionality (delay time).

Different types of Π operators and in consequence different frequency dependence were proposed, what is summarized in the paper of [14] in the form of repeated below the table

	Damped	Blackstock	Szabo	Stokes	Chen&Holm	Caputo& Wismer
		1985	2003		2004	1967/2006
Π	$\frac{\partial}{\partial t}$	$\frac{\partial^3}{\partial t^3}$	$\frac{\partial^{y+1}}{\partial t^{y+1}}$	$\frac{\partial}{\partial t}\nabla^2$	$\frac{\partial}{\partial t}\left(-\nabla^2\right)^{y^2}$	$\frac{\partial^{y-1}}{\partial t^{y-1}}\nabla^2$
α	ω^0	ω^2	ω^y	ω^0	ω^y	ω^y

Table 1.1: Different form of non-classical operators proposed in literature

In [11], [12] there were proposed the following forms of the equations that model different effect:

- Absorption but no dispersion:

$$\frac{1}{c_0}\frac{\partial^2 p}{\partial t^2} = \nabla^2 p + \tau \frac{\partial}{\partial t}\left(-\nabla^2\right)^{\frac{y}{2}} p, \tag{1.38}$$

  where $\tau = -2\alpha_0 c_0^{y-1}$, $\tilde{k}^2 = \frac{\omega^2}{c_0^2} + \tau\eta\tilde{k}^{y+1}$, $1 < y < 2$.

- Dispersion without absorption:

$$\frac{1}{c_0}\frac{\partial^2 p}{\partial t^2} = \nabla^2 p + \tau \Pi p. \tag{1.39}$$

  If $\Pi = \left(\nabla^2\right)^{y+1/2}$ then from Kramers-Krönig relations it follows that $\frac{1}{c_p} = \frac{1}{c_0} + \alpha_0 \tan\frac{\pi y}{2}\omega^{y-1}$.

- The most general equation with absorption and dispersion terms:

$$\frac{1}{c_0}\frac{\partial^2 p}{\partial t^2} = \nabla^2 p + \left[\tau \frac{\partial}{\partial t}\left(-\nabla^2\right)^{y/2)} + \eta\left(-\nabla^2\right)^{(y+1)/2} p\right], \tag{1.40}$$

$$\tau = -2\alpha_0 c_0^{y-1},\ \eta = 2\alpha_0 c_0^y \tan\frac{\pi y}{2}.$$

At the end of this chapter it will be presented a new type of equation modelling acoustic waves in lossy medium with non-classical dispersion and absorption, even more general than equation (1.40). It is the equation for the velocity potential Φ in the following form:

$$\beta\Delta^{y_1}\Phi - \frac{\partial^2\Phi}{\partial t^2} = \frac{\partial\Phi}{\partial t}\left[2\Delta^{y_2}\Phi + q\frac{\gamma-1}{2}\left(\frac{\partial\Phi}{\partial t}\right)^2 + q(\nabla\Phi)^2\right], \tag{1.41}$$

where $1 < y_1,\ y_2 < 2.$ and β, q and γ are material properties.

1.3 Analytic Signal

The mathematical background of analytic signal notion given below are repeated after the paper [68]. Many natural and man-made signals exhibit time-varying frequencies (e.g., chirps, FM radio waves). Characterization and analysis of such a signal $u(t)$ is based on instantaneous amplitude $a(t)$, instantaneous phase $\phi(t)$, and instantaneous frequency $\omega(t) = \phi'(t)$:

$$u(t) = a(t)\cos\phi(t). \tag{1.42}$$

It is convenient to use a complexified version of the signal whose real part is a given real-valued signal $u(t)$. Given $u(t)$ there are infinitely many ways to define the instantaneous amplitude and phase pairs so that (1.42) holds. This is due to the arbitrariness of the complexified version of u, i.e., $f(t) = u(t)+iv(t)$, where $v(t)$ is an arbitrary real-valued signal; yet this yields the representation of $u(t)$ via $a(t) = \sqrt{u^2(t)+v^2(t)}$, $\varphi(t) = \arctan\dfrac{v(t)}{u(t)}$. The instantaneous frequency is defined as $\omega(t) = \dfrac{d\varphi}{dt} = \dfrac{u(t)v'(t) - u'(t)v(t)}{u^2(t)+v^2(t)}$.

The usage of the analytic signal $f(t)$ as Hilbert transform of $u(t)$ as $v(t)$ had been proposed by D. Gabor in 1946.

Vakman (1972) proved that $v(t)$ must be of the Hilbert transform of $u(t)$ if there are imposed some apriori physical assumptions:

- $v(t)$ must be derived from $u(t)$,
- amplitude is continuous, i.e a small change in u causes a small change in $a(t)$,
- phase is independent of scale: if $cu(t)$, $c \in \mathbb{R}$ is arbitrary scalar, then the phase does not change from that of $u(t)$ and its amplitude becomes c times that of $u(t)$,
- harmonic correspondence: if $u(t) = a_0 \cos(\omega_0 t + \phi_0)$, then $a(t) \equiv a_0$, $\phi(t) \equiv \omega_0 t + \phi_0$.

Let us assume for simplicity that signals are 2π-periodic in $\theta \in [-\pi, \pi]$. Then we have the unit circle and unit disk $\mathbb{D}$ in $\mathbb{C} = \mathbb{R}^2$. Signals over $\mathbb{R} = (-\infty, \infty)$ can be treated similarly by considering the real axis and the upper half plane of $\mathbb{C}$.

The *analytic signal* of a given signal $u(\theta) \in \mathbb{R}$ is obtained via Hilbert transform $f(\theta) = u(\theta) + iH(u(\theta))$,

$$H(x) = \frac{1}{\pi} p.v. \int_{-\pi}^{\pi} u(\tau) \cot \frac{\theta - \tau}{2} d'\tau,$$

where $u(\tau) = \frac{}{a_0} 2 \sum_{k \leq 1} (a_k \cos k\theta + b_k \sin k\theta)$, so $H(u(\theta)) = \sum_{k \leq 1} (a_k \sin k\theta - b_k \cos k\theta)$.

Furthermore,

$$f(\theta) = \frac{a_0}{2} + \sum_{k \leq 1} (a_k - ib_k) e^{ik\theta}.$$

The boundary value of an analytic function $F(z) := U(z) + i\tilde{U}(z)$, $z \in \mathbb{D}$ where

$$U(z) = U\left(re^{i\theta}\right) = P_r \star u(\theta) = \frac{1}{2\pi} \int \frac{1 - r^2}{1 - 2r\cos(\theta - \tau) + r^2} u(\tau) d\tau,$$

$$\tilde{U}(z) = \tilde{U}\left(re^{i\theta}\right) = Q_r \star u(\theta) = \frac{1}{2\pi} \int \frac{2r\sin(\theta - \tau)}{1 - 2r\sin(\theta - \tau) + r^2} u(\tau) d\tau.$$

The original signal $u(\theta) = U(e^{i\theta})$ is the boundary value of the harmonic function U on $\partial\mathbb{D}$, which is constructed by the Poisson integral. $\tilde{U}$ and $Q_r(\theta)$ are referred to as the conjugate harmonic function and the conjugate Poisson kernel, respectively.

Hilbert (or RF) envelope was constructed with respect to the variable x. Let $\tilde{f}(x,y,z) = \tilde{f}_{y,z}(x)$, then the Hilbert envelope represents $\tilde{f}_{y,z}(x)$, $x \in X$, the absolute value of the Hilbert transform of real-valued function $H(x) = \frac{1}{\pi} p.v. \int\limits_{-\infty}^{\infty} \frac{f_{y,t}(x')}{x - x'} dx'$:

$$\tilde{s}(x,y,t) = \tilde{s}_x(y,t) = |f_{y,t}(x) + iH(x)|.$$

1.4 Wavelet Transform

The idea of the application of wavelet transforms in signal processing is widely used as this method gives more information of the signal behaviour (see e.g. [3], [7], [47]) and allows

- to figure the most characteristic features,
- to have localization in time and frequency domain simultaneously,
- to see the changes in time.

Nowadays wavelet-based technique are widely used in signal processing, approximation, time-series analysis and predicting, computer graphics and image processing. It is also an efficient tool for analysing the medical information. The usage of wavelet-based methods to study USG signals or other medical images for diagnosis are described in [62], [72]. The huge survey on the applications of wavelet methods for cancer diagnosis in soft tissues is given in [61] and [73].

The wavelet function $\psi(x)$ such that $\int\limits_{-\infty}^{\infty} \psi(x)dx = 0$ generates the detail coefficients. Its sense is to describe the signal. It also compose the basis by time shift with $\psi(t-b)$ the real parameter b and scaling $\frac{1}{a}\psi\left(\frac{t}{a}\right)$ with the positive real parameter a. The parameter b gives the wavelet position and a is the scale parameter in time. In the frequency domain the small values of a represent the high frequencies, the large values — the low frequencies. Scaling function $\varphi(x)$ such that $\int\limits_{-\infty}^{\infty} \varphi(x)dx = 1$ generates the approximation coefficients.

1.4.1 Discrete Wavelets. Approximation and Detail Coefficients

In the case of the discrete signal the corresponding discrete wavelet transform is used [27].

For the scale coefficient a it is used the dyadic discretization scale $a_j = 2^{-j}$, where $j \in \mathbb{Z}$ is a scale index. The coefficient b is discretized linearly so that $b_{j,i} = i2^{-j}$, $i \in \mathbb{N}$.

The formula for discrete wavelets in general case may be written as follows

$$\psi_{j,i}(x) = \frac{1}{\sqrt{a_j}}\psi\left(\frac{x - b_{ji}}{a_j}\right) \tag{1.43}$$

and the discrete decomposition formula

$$w_{ji} = \int_{-\infty}^{\infty} f(x)\overline{\psi_{ji}(x)}dx. \tag{1.44}$$

The corresponding discrete reconstruction formula is

$$f(x) = C\sum_{j=-\infty}^{\infty}\sum_{j=-\infty}^{\infty} w_{ji}\psi_{ji}(x) + R(x). \tag{1.45}$$

Here C is a constant and $R(x)$ is a residual which depends on the choice of wavelet [35].

This technique in general is concludes is the signal's representation consists of two parts. The fist one is rude and is called approximation, the second is more refined, it is called detail. These process is iterative and it stops when the required accuracy is reached. The described method supposed the usage of two required functions ψ and φ for the wavelet decomposition and following signal reconstruction [7].

The detail coefficients d_{ji} are calculated as follows:

$$d_j = \sum_{i\in\mathbb{Z}} w_{ji}\psi_{j,i}(x), \tag{1.46}$$

and the approximation coefficients a_j for the fixed level j:

$$a_j = \sum_{j>J} d_j. \tag{1.47}$$

Thus the reconstruction formula for the signal f at the nth level is

$$f(x) = a_n + \sum_{i=1}^{n} d_i, \tag{1.48}$$

where a_n denotes the approximation at the nth level and d_i are the detail coefficients for the levels from 1 up to nth. The formulae for construction the wavelet and scaling functions and the procedure of MRA are described in Appendix A

These coefficients allow to make the high-pass and low-pass filter for initial signal function. The result of the high-pass filter is detailed coefficient d_1 and the result of the low-pass filter is approximate coefficient a_1. Later a_1 is filtered again and this process is repeated until the required accuracy or pre-defined features are reached. As an example, let us consider the 3-levels decomposition of some signal function $f(x)$. At first level, an original signal is processed by the high-pass and low-pass filter [80]. The final result is approximate coefficient a_3 and the entire detail coefficient d_1, d_2, d_3. Hence, $f(x)$ as reconstructed signal can be expressed in the following

$$f(x) = a_3 + d_3 + d_2 + d_1, \tag{1.49}$$

see Fig. 1.1.

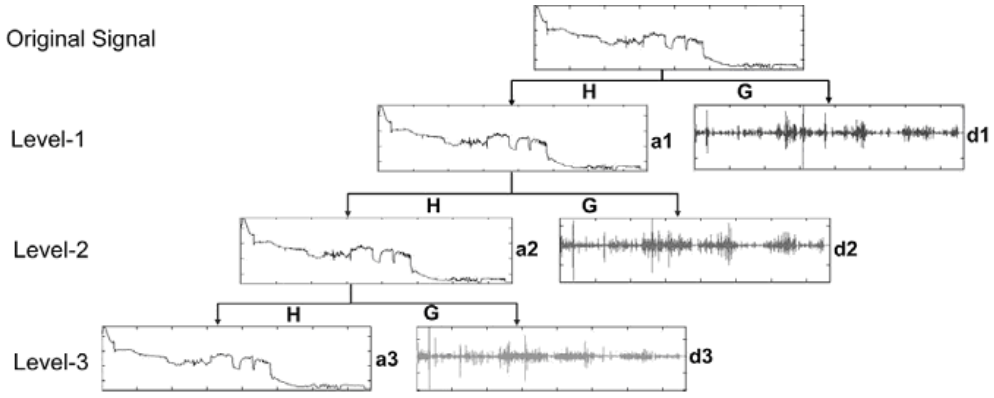

Figure 1.1: Visualization of the example signal's decomposition into levels

The problem to decide is that is how these discrete wavelet coefficients can reduce the noise level and reconstruct a signal without losing the essential information. In general, an inappropriate wavelet function and decomposition level lead to the signal defect and losing of essential information. In [80] there was proposed a metric based on information quality ratio to determine the best-suited wavelet function.

1.4.2 Time-Frequency Localization

Many studies using wavelet analysis have suffered from an apparent lack of quantitative results. The wavelet transform has been regarded by many as

an interesting diversion that produces colorful pictures, yet purely qualitative results. This misconception is in some sense the fault of wavelet analysis itself, as it involves a transform from a one-dimensional time series (or frequency spectrum) to a diffuse two-dimensional timefrequency image. This diffuseness has been exacerbated by the use of arbitrary normalizations and the lack of statistical significance tests. The purpose of the paper [5] was to provide an easy-to use wavelet analysis toolkit, including statistical significance testing.

We follow some part of the paper [80], where the differences between windowed Fourier transform and wavelet transform are demonstrated.

The Windowed Fourier transform (WFT) represents one analysis tool for extracting local-frequency information from a signal. The Fourier transform is performed on a sliding segment of length T from a time series of time step δt and total length $N\delta t$, thus returning frequencies from $\frac{1}{T}$ to $\frac{1}{2\delta t}$ at each time step. The segments can be windowed with an arbitrary function such e.g. as a Gaussian window. The WFT represents an inaccurate and inefficient method of timefrequency localization, as it imposes a scale or "response interval" T into the analysis. The inaccuracy arises from the aliasing of high- and low-frequency components that do not fall within the frequency range of the window. The inefficiency comes from the $\frac{T}{2\delta}$ frequencies, which must be analyzed at each time step, regardless of the window size or the dominant frequencies present. In addition, several window lengths must usually be analyzed to determine the most appropriate choice. For analyses where a predetermined scaling may not be appropriate because of a wide range of dominant frequencies, a method of time-frequency localization that is scale independent, such as wavelet analysis, should be applied.

The wavelet transform can be used to analyze time series that contain nonstationary power at many different frequencies. Assume that one has a time series, x_n, with equal time spacing $\delta_n = 0, \ldots, N-1$. Also assume that one has a wavelet function, $\psi_0(\eta)$, that depends on a nondimensional "time" parameter η. To be admissible as a wavelet, this function must have zero mean and be localized in both time and frequency space.

Next examples display the features of the acoustics signals that cannot be noticed using usual Fourier analysis but may be detected be wavelet spectrum and coefficients. The idea to study the combinations of sine-functions was taken from the paper [7], but the calculations and comments are given by author.

Example 1. We consider the signal of the form

$$s_1(t) = \sin\frac{2\pi t}{t_1} + \sin\frac{2\pi t}{t_2}, \tag{1.50}$$

having two frequencies at the same time interval.

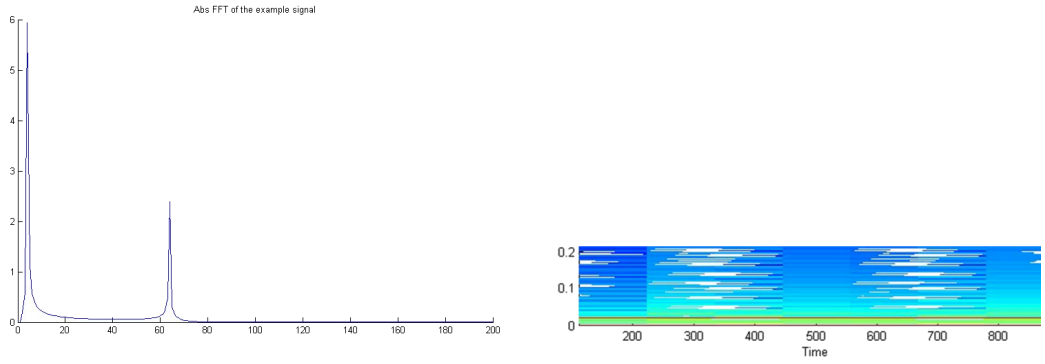

Figure 1.2: Spectrum and spectrogram of the signal, example 1

Figure 1.2 represents on the left the absolute value of fast Fourier transform and on the right the spectrogram of this signal. It is obvious that there are two main frequencies in the examined signal but their changes in time are not visible.

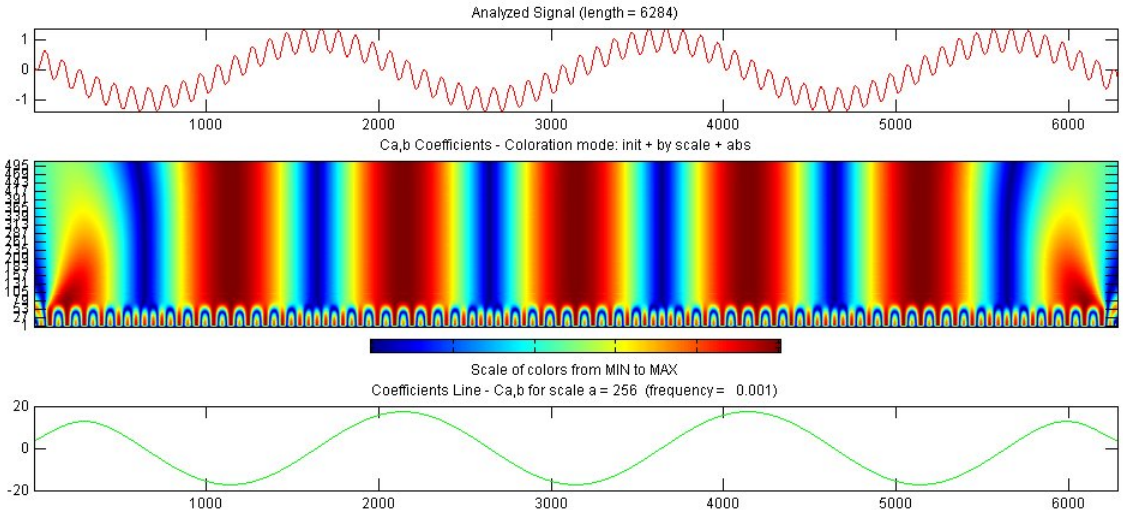

Figure 1.3: Coefficient distribution of the signal, example 1

Making the wavelet transform using MatLab Wavelet Toolbox [82] is is possible to observe the wavelet spectrum of one-dimensional signal as 3-dimensional surface which may be visualized as coordinate system amplitude-frequency–time (Fig. 1.3) and the set of the amplitude and detail coefficients of (Fig. 1.4).

The wavelet spectrum has periodically repeating fragments that are result of convolution of the high-frequency signal's component and wavelet functions

of the small scale values. The lager scales are the example of noise removal, so finally the summand of the smaller frequency is reduced and we have as in the third graph of the Fig. 1.4. The periodical structure of signal preserves, moreover, it is clearly visible how the energy changes in time.

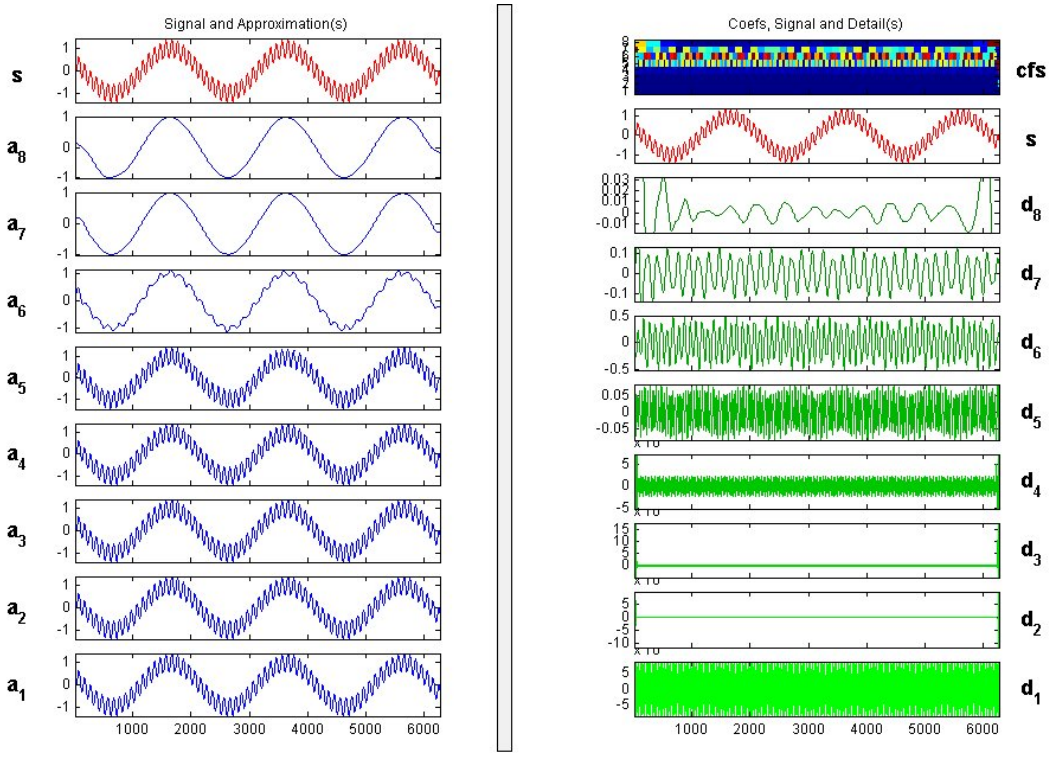

Figure 1.4: Amplitude and detail coefficients of the signal, example 1

Fig. 1.4 shows the full decomposition of the signal up to the 6th level. Here the red graph represents the signal itself, blue graphs correspond to the amplitude coefficients a_j and green correspond to the detail coefficient d_j. The evolution of a_j coefficients shows how the higher frequency component may be reduced from the signal. The detail coefficients of the lower levels may be treated as a noise, so the procedure of noise removal means taking off the detail coefficients from the lower levels i.e. of high frequency.

Example 2. Let us consider the signal of the form

$$s_2(t) = \begin{cases} t_1 \sin \dfrac{2\pi t}{t_1} & t \in [-10\pi, 0] \\ t_2 \sin \dfrac{2\pi t}{t_2} & t \in [0, 10\pi] \end{cases} \tag{1.51}$$

that also has two main frequencies but they are located in the different regions with respect to time variable. These frequencies are also well seen in the one-

side spectrum's amplitude graph (Fig. 1.5, left image) and its spectrogram (Fig. 1.5, right image).

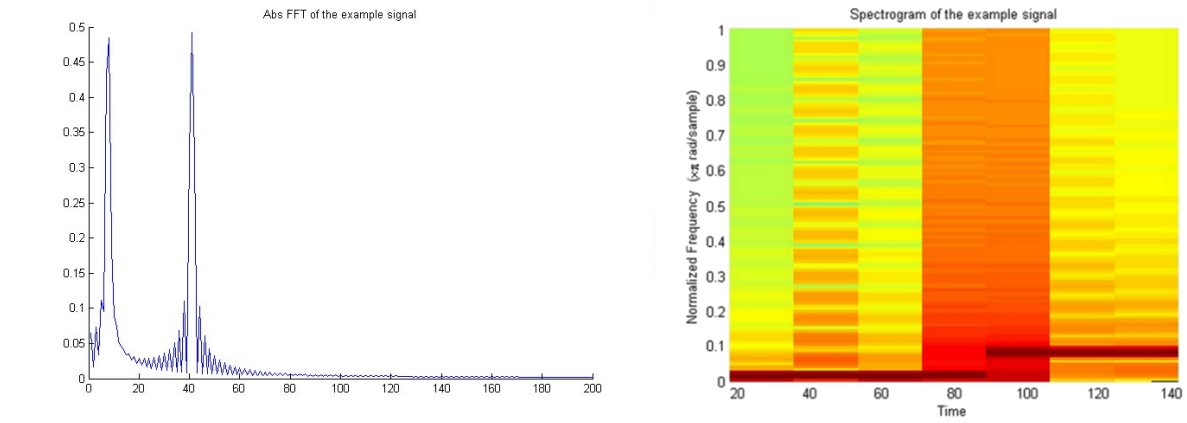

Figure 1.5: Spectrum and spectrogram of the signal, example 2

Performing the wavelet decomposition we may observe the periodical changes of each part of the signal and the changes of these parts (see Fig. 1.6).

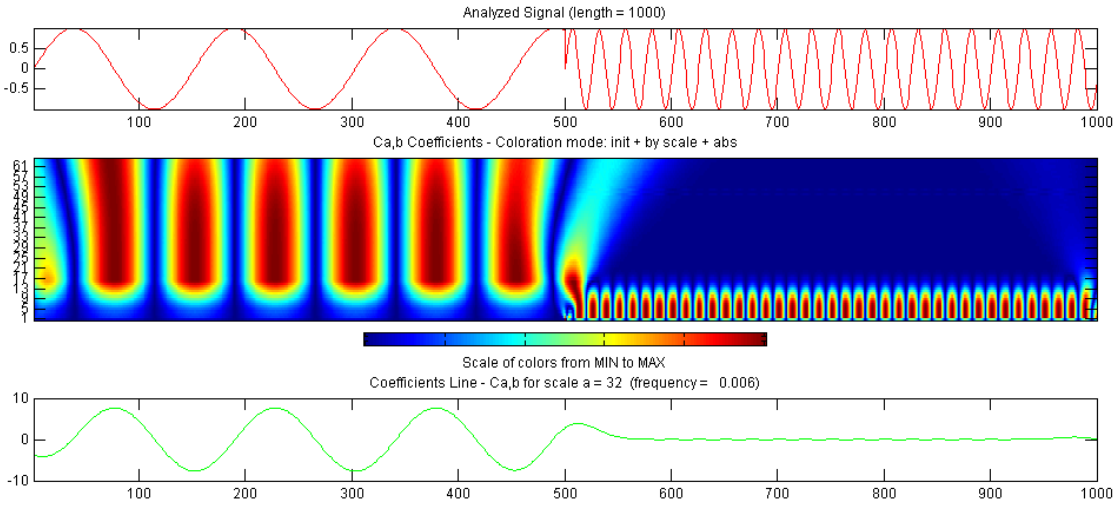

Figure 1.6: Coefficient distribution of the signal, example 2

1.4.3 Daubechies Wavelet Family

One of the problems in wavelet's application is to select the analyzing wavelet or family as there is no general algorithm to solve it, because different basis would show different signal's features. It is proposed to use the special wavelet function if there is known about the signal's particularities or the

form of the periodical patterns to find [3]. In the QUS the Daubechies wavelet family is used rather often as these functions match the reflection impulse [39]. That is why the Daubechies 6 family had been chosen as analyzing wavelet. The left image Fig. 1.7 presents the form of the initial impulse used in the experiments described in the thesis, right image shows the Daubechies 6 wavelet function.

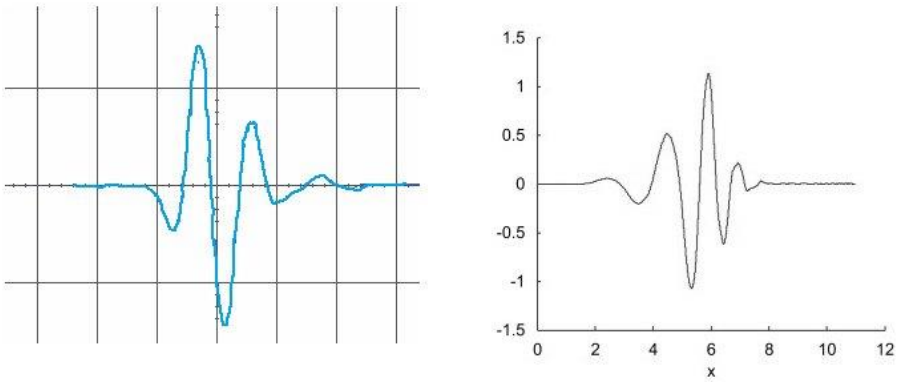

Figure 1.7: Initial impulse and Daubechies 6 wavelet function

The Daubechies wavelet family is a family of orthonormal wavelets ([27]) with compact support which are frequently used for analyzing real signals. These wavelet and scaling functions have no analytic representation, they are constructed recurrently by the equalities (A.7).

In our investigation the Daubechies 6 family was chosen as the analyzing wavelets. The motivation of the choice was the following. The corresponding wavelet function ψ_k have compact support namely the k-level wavelet function has support $[0, 2k+1]$, and they have also 6 vanishing moments. The coefficients for scaling function ψ h_k are obtained from the system of equations (A.8) – (A.12) from Appendix A and their values values are $h_1 = 0.47046721$, $h_2 = 1.14111692$, $h_3 = 0.650365$, $h_4 = -0.1909344$, $h_5 = -0.1208322$, $h_6 = 0.0498175$. Coefficients g_k may be obtained from the equality (A.9).

In Fig. 1.8 on there are shown the scaling function φ (left) and wavelet function ψ for Daubechies 6 family.

The are some mathematical properties that also allow to use Daubechies wavelets of order p for the analysis of analytic signals:

- they are orthogonal;
- have compact support;
- there is no symmetry for $p > 1$;

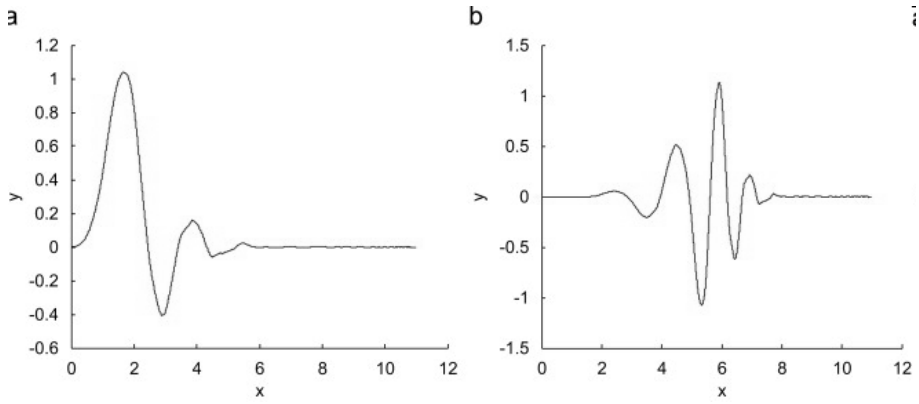

Figure 1.8: Daubechies 6 scaling and wavelet functions

- they have p vanishing moments;
- the filter length is equal to $2p$.

1.4.4 Scale Index as a Tool for Periodicity Detecting

The idea of the investigation of the periodicity of backscattered acoustic signals comes from the dynamic systems theory [8]. Here the theorem connecting the wavelet decomposition level and the periodical structure of signal is proved and there is introduced an index ind_{sc} depending on the wavelet approximation level which allows to identify the periodical signals. As there may arise a boundary effects, the inner part of the wavelet coefficients distribution called scalogram will be used. It is underlined that usage of continuous wavelet transform is preferable.

The general idea of this method is based on the energy of approximated signal calculated for each scale a:

$$E(a) = \left(\int_{-\infty}^{\infty} |Wf(a,b)|^2 db \right)^{1/2}, \tag{1.52}$$

where a is supposed to change continuously in $\mathbb{R}$.

Despite of the localization properties of integral wavelet transform the boundary effects still exist. They may be seen, for example, at the coefficients distribution in figure (1.3) and they influence the energy distribution of $E(a)$. To avoid the boundary effects the set of possible values is narrowed down to the interval $[t_1(a), t_2(a)]$, which may be different for different scale.

$$E^{in}(a) = \left(\int_{t_1(s)}^{t_2(s)} |Wf(a,b)|^2 db \right)^{1/2}. \tag{1.53}$$

Interval $[t_1(a), t_2(a)]$ should contain all the wavelets $\psi_{a,b}$ for all $a \in [t_1(a), t_2(a)]$. To compare the energy values for different scales the normalized energy is considered

$$E^{in}_{norm}(a) = \frac{E^{in}(a)}{\sqrt{t_2(a) - t_1(a)}}. \tag{1.54}$$

Figure 1.9 demonstrates the $E^{in}_{norm}(a)$ for the numerically modelled signal consisting of 1200 points and its central part obtained by cutting some parts of signal from both sides. The black graph shows the $E^{in}_{norm}(a)$ for the full signal $f(x)$, the blue graph corresponds to the $E^{in}_{norm}(a)$ for $f_{95}(x)$ containing 95% of $f(x)$, the green graph corresponds to the $E^{in}_{norm}(a)$ for $f_{90}(x)$ containing 90% of $f(x)$, the red graph corresponds to the $E^{in}_{norm}(a)$ for $f_{80}(x)$ containing 80% of $f(x)$. As these graph do not coincide, it may be concluded that boundary effect really takes place.

The difference of $E^{in}_{norm}(a)$ for initial and reduced signals is shown in Fig. 1.10, the color of curve corresponsd Fig. 1.9. It may be noticed that the smallest difference is $f(x) - f_{80}(x)$.

For the detection of the periodicity there is applied a special marker called index and proposed in [8]. In this paper it is also proved the theorem that for complex-valued periodical function $f \in L^2([0,T])$ with period T and compactly supported wavelet ψ the wavelet transform $Wf(t, 2T) = 0$ for all $u \in \mathbb{R}$. That is why for compactly supported wavelet function the normalized energy $E_{norm} = 0$ at scale $a = 2T$.

The energy is studied on the in scale interval $[a_1, a_2]$ and the scale index is calculated

$$ind_{sc} = \frac{E(a_{min})}{E(a_{max})}. \tag{1.55}$$

Here $E(a_{max})$ is the smallest scale in for energy maximal value $[a_1, a_2]$ and $E(a_{min})$ is the minimum of energy in the interval $[a_{max}, a_2]$.

The index coefficient $ind_{sc} \in [0, 1]$. For periodic signals it is zero and it is equal to 1 for highly non-periodic signals (see [8]).

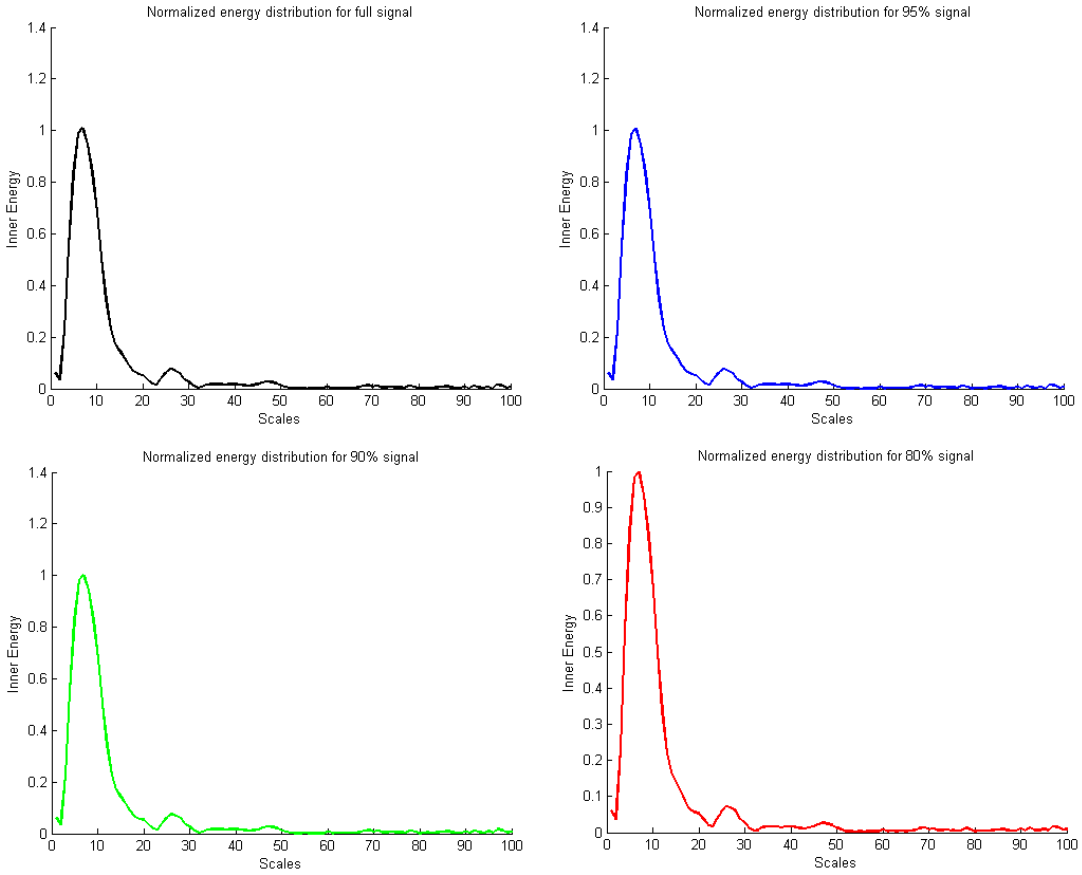

Figure 1.9: $E^{in}_{norm}(a)$ for initial and reduced signals

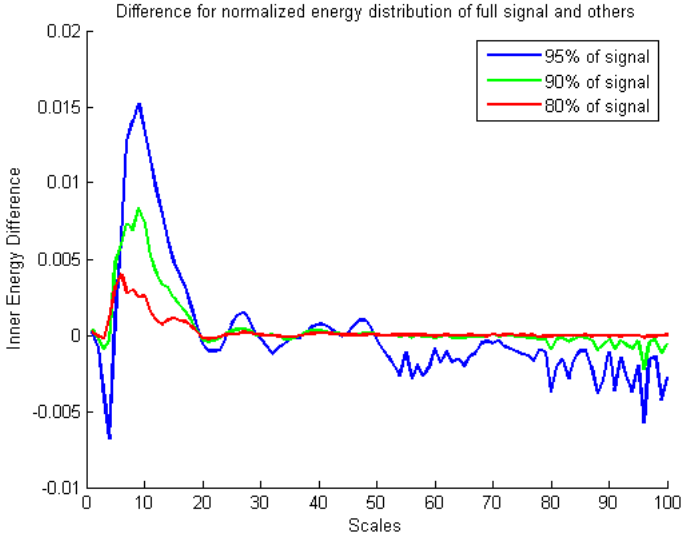

Figure 1.10: Difference of $E^{in}_{norm}(a)$ for initial and reduced signals

1.4.5 Improvement of Mean Scatterer Spacing Parameter

As RF echo signal $y(t)$ is a result of the interaction of ultrasound pulse with the scattering structure [86], it may be represented as the convolution of the impulse response $h(t)$ and the scattering function $x(t)$

$$y(t) = h(t) \cdot x(t),$$

where $\cdot$ represents the convolution operator, and t is a time axis related to the radial distance by the propagation of the ultrasound pulse. The impulse response $h(t)$ integrates the characteristics of the transducer, diffraction, and frequency-dependent attenuation. The scattering function $x(t)$ can be written as

$$x(t) = \sum_{m=1}^{N_D} \alpha_m \left(t - \gamma_m\right) + \sum_{n=1}^{N_C} \beta_n \left(t - \nu_n\right),$$

where N_D is the total number of diffuse scatterers; α_m denotes the scattering function of the mth diffuse scatterer with delay γ_m corresponding to its effective scattering center; N_C is the total number of coherent scatterers; β_n denotes the scattering function of the nth coherent scatterer with delay ν_n corresponding to its effective scattering center.

The discrete variant of the RF echo $y(t)$ is called the A-scan $y(n)$ is obtained, its power spectrum of the may be calculated by Fourier transform

$$Y(f) = FT\left[y(n)\right], \;\; P_{FT} = E\left[\left|Y(f)\right|^2\right],$$

where $E[\,]$ denotes the expectation operator [86].

To characterize the periodicity in tissue it is used a special parameter called *mean scatterer spacing (MSS)*. It shows the average periodicity in RF signal caused by the periodical structure of scattering media. The idea of measuring the distance of the peaks of signal's transformation had been proposed in [40]. There are several approaches in computing the MSS.

The first approach is based on the detecting the peaks in the Fourier transform spectrum and the fact that the peaks in A-scan $y(n)$ correspond to the peaks in its power spectrum $P(f)$, so they may be found. The peaks in the time domain domain occur at $2d = \Delta t c$ and the corresponding peaks in the spectrum domain occur at

$$d = \frac{c}{2\Delta f}, \tag{1.56}$$

where c is speed of sound, Δt is time interval, Δf is frequency interval, d is MSS.If the largest peak occurs at (f_{p_1}, f_{p_2}) then $\Delta f = |f_{p_1} - f_{p_2}|$. The $[y(n)]^2$ may be also used for Fourier spectrum MSS estimate.

This method had been used, fpr example, to investigate the mean scatterer spacing in bovine liver ex vivo samples (see [66], [28]).

The second approach suggests using the wavelet transform instead of Fourier spectrum (see, e.g. [74], [86]) by studying modulus maxima at different decomposing scales corresponding to the location of coherent scatterers, so, the distance between modulus maxima is may be treated as MSS.

As wavelet decomposition may be performed into different scales, there is a problem of choosing the best level for the wavelet transform. In this work it will be used the formula [45]

$$\log_2\left(\frac{f_s}{f}\right) - 1 < J < \log_2\left(\frac{f_s}{f}\right). \tag{1.57}$$

Here J is a wavelet decomposition level, and f_s is a sampling frequency and f the fundamental frequency that may be obtained from formula (1.56). Thus thw MSS may be calculated as follows:

$$MSS = \max_{i\in[1,N]} |W_J s(z_i) - W_J s(z_{i-1})|. \tag{1.58}$$

where $W_J s(z_i)$ is wavelet approximation of signal s at the point z_i, N is number of sampling points.

The percentage error of the MSS is obtained by the relation

$$e = \frac{|MSS_e - MSS_r|}{MSS_e} \cdot 100\%, \tag{1.59}$$

where MSS_e and MSS_r and are measured and calculated approximate values of mean scatterers spacing correspondingly.

1.5 Statistical Distributions

1.5.1 Effective Number of Scatterers

The effect of absorption and scattering on the amplitude of the echo signal (attenuation) received by the ultrasonic head is measured collectively as a decrease in amplitude during propagation. Absorption in the tissue, as explained in the introduction to the section 1.1, it is not a classic absorption and modeling this phenomenon requires the generalization of classical models of sound propagation in liquids.

In this chapter we will present simple models of scattering in order to show how from the information contained in the echo envelope statistics can be used to get the numerical parameters describing scatterers number

and their spatial distribution. Scattering is a phenomenon of reflection from objects smaller than the wavelength. Tissue is not a homogeneous medium, the sources of the ultrasound scattering assuming a linear propagation model are in the changes of density and compressibility

The scattering depends on many geometrical factors, such as the size, shape or spatial distribution of the scattering objects, and on the physical factors such as the compressibility and density of the material from which these objects are built. The simplest model of scattering is the discrete model, in which the wave propagates in a homogeneous medium with inclusions (scatterers) of others than properties of this medium. The ability of a point object to disperse the wave it is coded with a single parameter, the scattering cross-section. A backscatter coefficient is also introduced, which is a measure of the power dissipated by the object in the opposite direction to the direction of incident wave. This is implicitly the part of the scattered signal that has to return to the source of the wave, which in the case of considered signals used in medical imaging, means to the scanning head.The so-called point model of the signal $s(t)$, in which we assume point sources as scatterers can be treated as a random walk due to the random location of the scatterers in the resolution cells [71]:

$$s(t) = \sum_{n=1}^{N} \alpha_n \cos\left(\omega_0 t + \phi_n\right),$$

where ω_0 is the mean frequency of excitation pulse and N is the number of scatterers in the resolution cell. Ift the phases ϕ_n is modeled as uniformly distributed in $[0, 2\pi]$ and the amplitude is usually considered to be normally distributed. The fully diffusive scattering model assumes a high number of scatterers, so the Central Limit Theorem applies and the backscattered echo can be expressed as

$$s(t) = X \cos\left(\omega_0 t)\right) + Y \sin\left(\omega_0 t)\right),$$

where X and Y are zero mean identically distributed Gaussian distributions.

1.5.2 Rayleigh and Rician Distributions

Then, the envelope of the backscattered signal echo, $R = \sqrt{X^2 + Y^2}$ is Rayleigh distributed [77]:

$$f_R(r) = \frac{r}{\sigma^2} e^{-\frac{r^2}{2\sigma^2}} u(r), \tag{1.60}$$

where $u(\cdot)$ is the Heaviside step function defined as $u(x) = \begin{cases} 0, & x < 0, \\ 1, & x \geq 0. \end{cases}$

Under the same as previously made assumption of a high number of effective scatterers but with the presence of resolvable structures in the resolution cell (specular component, C), X and Y become nonzero Gaussian distributions. The envelope does no longer follow a Rayleigh distribution but a Rician one

$$f_{Rician}(r) = \frac{r}{\sigma^2} e^{-\frac{r^2 + C^2}{2\sigma^2}} I_0\left(\frac{rC}{\sigma^2}\right) u(r), \tag{1.61}$$

where $I_0(\cdot)$ is the modified Bessel function of first kind [67].

1.5.3 K-distribution

When the number of scatterers decreases and the Central Limit Theorem cannot be applied, more complicated distributions are proposed to model the distribution of the backscattered signal envelope. Concretely, the K-distribution models the case when the number of scatterers is a random variable itself, which is modeled as a Poisson distribution whose local mean is Gamma distributed.

The K-distribution is formed by compounding two separate probability distributions, one representing the radar cross-section, and the other representing speckle that is a characteristic of coherent imaging. The model used to represent the observed intensity X, involves compounding two gamma distributions. In each case a reparametrization of the usual form of the family of gamma distributions is used, such that the parameters are: the mean of the distribution, and the usual shape parameter.

The probability density function of the amplitude of the Hilbert envelope, which fits K-distribution with parameters $(\alpha, b) \in (0, +\infty) \times (0, +\infty)$ is given by

$$f_K(x) = \frac{2b}{\Gamma(\alpha)} \left(\frac{bx}{2}\right)^{\alpha} K_{\alpha-1}(bx) \tag{1.62}$$

for any $x \in (0, +\infty)$.

Here $\alpha \in (0, +\infty)$, $b \in (0, +\infty)$, Γ is a real-valued Gamma-function, $K_{\alpha-1}$ is a modified Bessel function of second kind of the order $\alpha - 1$ [67]:

$$K_\gamma(z) = \frac{\pi}{2 \sin \gamma\pi} \left[I_{-\gamma}(z) - I_\gamma(z)\right],$$

$$I_\gamma(z) = \sum_{k=0}^{\infty} \frac{(z/2)^{2k+\gamma}}{\Gamma(\gamma + k + 1) + k!}.$$

The parameter α of K-distribution is a shape parameter which is proportional to the actual density of scatterers because of its practical meaning. Parameter b is a scaling parameter of distribution, $b = \sqrt{\frac{4\alpha}{E(x^2)}}$ where $E(A^2)$ is the second moment of the envelope amplitude.

The normalized fourth moment r_4 of the K-distribution are functions of α. It leads to the following estimator α_0 for the density of scatterers, also called "effective number of scatterers"

$$\alpha_0 = \frac{2}{r_4 - 2} = \frac{2}{\frac{E(x^4)}{(E(x^2))^2} - 2}, \tag{1.63}$$

the corresponding formula for the scale parameter is

$$b_0 = 2\sqrt{\frac{4\alpha_0}{E(x^2)}}. \tag{1.64}$$

The two parameters of this distribution, namely size and scale parameters, together provide information on the number density of scatterers, the variation in the scattering amplitudes within the range cell and mean scattering amplitudes. In the case of a medium where the scatterers are not regularly spaced, the resulting echo is a coherent sum of reflected waves from randomly distributed scatterers. If the number of scatterers per resolution cell is greater than 10, the amplitude of the envelope of the signal is Rayleigh distributed. For densities less than 10 the envelope is modeled with a K-distribution (cf. [2], [63], [70]).

1.5.4 Nakagami Distribution

The PDF for K-distribution has no closed expression and this limits its use. On a completely different approach, P.M. Shankar in [71] proposed a Nakagami distribution as a "simpler universal model for tissue characterization". Unlike the previously reviewed models, the Nakagami is not based on physical arguments or on a bottom-up modeling of the scattering process. However, it has empirically shown a better performance than the Rayleigh and Rice distributions The Nakagami distribution is related to the gamma distribution. In particular, given a random variable X which is Gamma distributed, than random variable Y obtained by taking square root of X, i.e. $Y = \sqrt{X}$ is Nakagami distributed.

The probability density of Nakagami distribution has the form ([52])

$$f_{Nak}(x;\mu,\omega) = \frac{2\mu^{\mu}}{\Gamma(\mu)\,\omega^{\mu}} x^{2\mu-1} e^{\frac{\mu}{\omega}x^2}. \tag{1.65}$$

Parameter $\omega = E\left(X^2\right)$ is a positive parameter controlling spread, $\mu = \frac{E^2\left(X^2\right)}{D\left(X^2\right)}$ is a shape parameter, $\mu > \frac{1}{2}$.

1.5.5 Gamma Distribution

The power of backscattered echo from tissues is often assumed as being Gamma-distributed, as it was assumed in the definition of Nakagami distribution. The probability density function of Gamma-distribution is

$$f(x;a,b) = x^{a-1}\frac{1}{b^a\Gamma(a)}e^{-\frac{x}{b}}, \tag{1.66}$$

where $\Gamma(x)$ is a real-valued Gamma-function $\Gamma(x) = \int_0^{-\infty} t^{x-1}e^{-t}dt$ for $x > 0$. Parameter a may be treated as a shape parameter and b as scale parameter.

Summing up the values of shape parameters of K-distribution and Nakagami distributions are directly connected with effective scatterer number, if the values are grater the scatterers number is greater. The shape parameter of Gamma distribution is also dependent on the scatterer density, but not in a linear way.

2 Scatterers' Density Differentiation

The aim of this Chapter is to find quantitative parameters connected with effective scatterers numbers by studying envelopes of the raw RF (radio frequency) backscattered signals from agar-gel samples with different number of scatterers. The content and the results of this Chapter were partially repeated from published papers [19] and [43].

2.1 Experiments Description

During the performed experiment, cf. [43], three types of phantoms were fabricated, which simulate well a soft tissue properties. The first phantom was "pure", it will be named further as Phantom A, the second one (called Phantom B) has inside glass beads with density 6 items per mm^3, the third one has density 30 balls per mm^3 (Phantom C). The balls were uniformly distributed and had diameter 755 μm and density 3000 kg/m^3. We have the aim of distinguishing these phantoms by the structural quantitative parameters which can "counting" the number of beads. The differences in the acoustical characteristics between phantoms were discussed in [43].

For the generation and reception of ultrasonic pulses the transmitter-receiver JSR Ultrasonics DPR 300 Pulser/Receiver was used and Imasonic head (center frequency 6MHz, diameter 9 mm, the focal length 62 mm). The received RF signals were recorded with oscilloscope (Agilent Technologies type DS09104A). The collection of RF signals, obtained from sonication of phantoms, had been registered. The number of signals was 10 in the experiment 1 and of 25 signals in the experiment 2. The difference between these experiments was in in the acoustic beam focus locations that was situated at the mirror lying on the bottom of phantom in experiment 1 and at the center of samples in the experiment 2.

Characteristics of the obtained phantoms represented in the table 2.1. Fig. 2.1 displays the two types of phantoms, Phantom A (pure) on the left and Phantom C on the right.

Phantom type	**A**	**B**	**C**
Glass beads concentration [psc/mm^3]	0	6	30
Glass beads volume fraction [%]	0	0.13	1.66

Table 2.1: Phantoms' characteristics

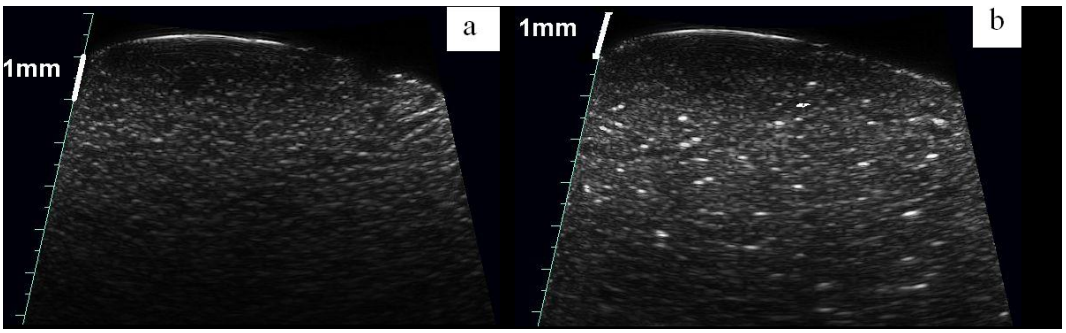

Figure 2.1: B-modes of phantoms without inclusions and with glass balls inside

2.2 Calculation Algorithm

2.2.1 Pre-transformations

1. The initial dataset consisted of 10000 points (sampling points of RF signal) for the experiment 1 and of 13000 points for the experiment 2. In Fig. 2.2, left images shows the examples of the RF backscaterred signals that correspond to each type of phantom: the signal on top corresponds to Phantom A, next one — to Phantom B and the signal at the bottom corresponds to Phantom C.

   For both experiments there were determined regions of interests (ROIs) obtained by cutting areas of the amplitude growth caused by the mirror metal plate located on the bottom of phantoms and boundary effect on the starting point of initial impulse. Thus signals were cut off form the left and right hand sides. For experiment 1 the cut signal has 5200 points and for experiment 2 — 9000 points. In Fig. 2.2 images on the right there are given the examples of cut signals.

2. The frequency filter had been applied, so all frequencies higher than 12 mHz were cut off, because of the transducer band.

3. Hilbert transform which defines a signal envelope has been calculated and this envelope afterwards is called and is used as a "signal": $\tilde{S}(x) = |S_{x,y}(x) + iH(x)|$, $H(x) = \text{p.v.} \int\limits_{-\infty}^{\infty} \frac{S(x)}{x - x'} dx'$.

4. For experiment 2 data were normalized with respect to variable amplitude x: $S_i(x) = \frac{\overline{S}_i(x)}{\max_{x \in X'} \left\{ \overline{S}_i x \right\}}$, $i = \overline{1, 25}$.

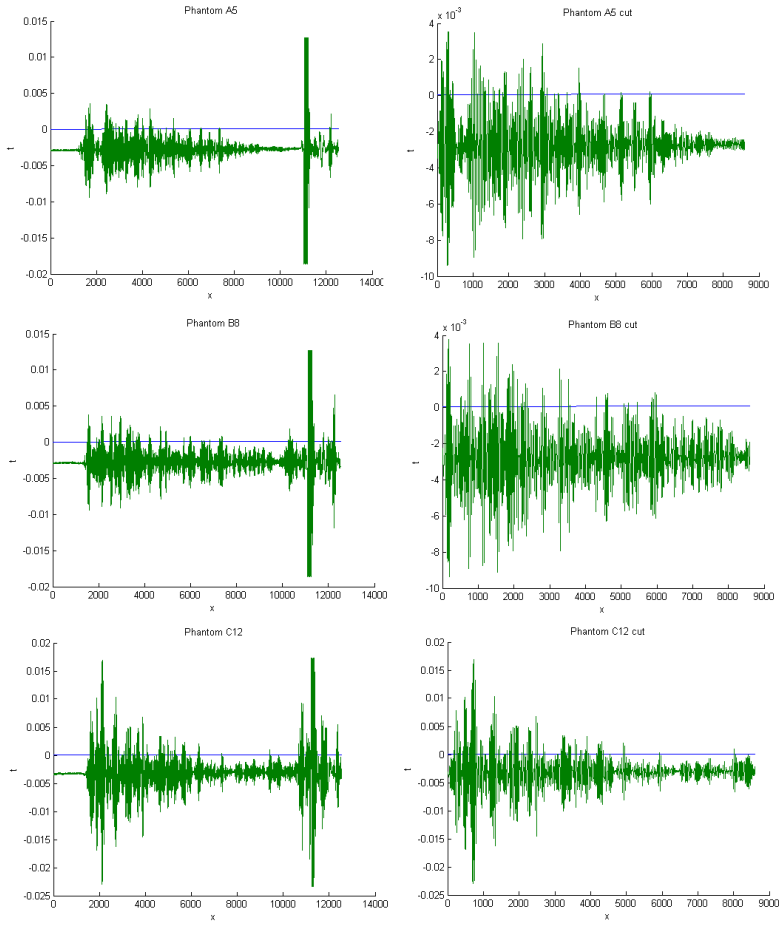

Figure 2.2: Examples of backscattered and cut RF signals

In the experiment 1, in addition to normalized signals, the raw initial data from ROI (region of interest) here, the shortened domain of signal, was also used.

2.2.2 Wavelet Decomposition

For further analysis a discrete wavelet transform (1.44) was performed by using the Daubechies 6 wavelets introduced in section 1.4.3. The approximation and reconstruction (A.3) of signals was made, approximation (1.47) and detail (1.46) coefficients were calculated. Using the raw signals in experiment 1 the wavelets decomposition of signals is analyzed. The decomposition of original signals for 12 levels is calculated. The example is shown on the Fig. 2.3.

In the Fig. 2.3 s denotes the original signal, graphics a_1 – a_{12} denote approximations and d_1 – d_{12} details coefficients, respectively for levels from 1 to 12, the coefficient distribution is presented on the top right of the graph.

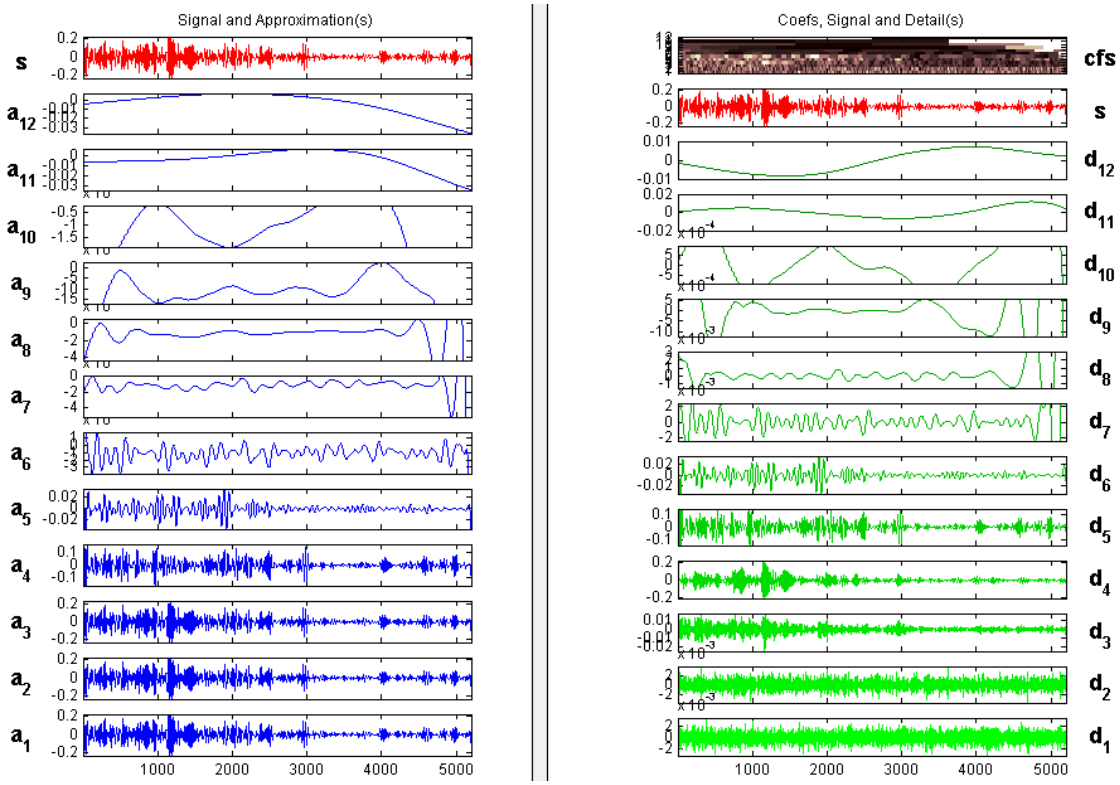

Figure 2.3: Example of RF signal's decomposition for 12 levels

Let us notice that because matrix material is the same in the three phantoms the differences arising in analysis are due only to the different number of scatterers. It has been observed that on the 9-level of approximation there appear similarities between Phantom A and Phantom C, while Phantom B is qualitatively different. This fact is even stronger on the 12th-level of approximation. In the matrix material (gel) we have rather uniformly distributed weak scatterers and the amplitude of reflected wave fluctuations are also not high.

The comparatively large number of glass beads can be considered to be also distributed uniformly and they dominate in the backscattered signal amplitude fluctuations but with higher amplitude values than in the case of pure matrix Phantom A, giving rise to similarities in character of scattering. Contrary, comparatively low density of strong scatterers in Phantom B, and, at the same time the noise coming from weak scatterers in the gel matrix, introduce the "double structure" of randomness preserved in the the backscattered signal properties. It is probably the difference visible in wavelet form of 12th level approximation. To discover other differences in what follows we apply wavelet analysis and analyze statistical properties of the envelopes of signals. It should be noticed that for the experiment 1 we will perform the analysis

without any kind of receiver–transducer and attenuation compensations.

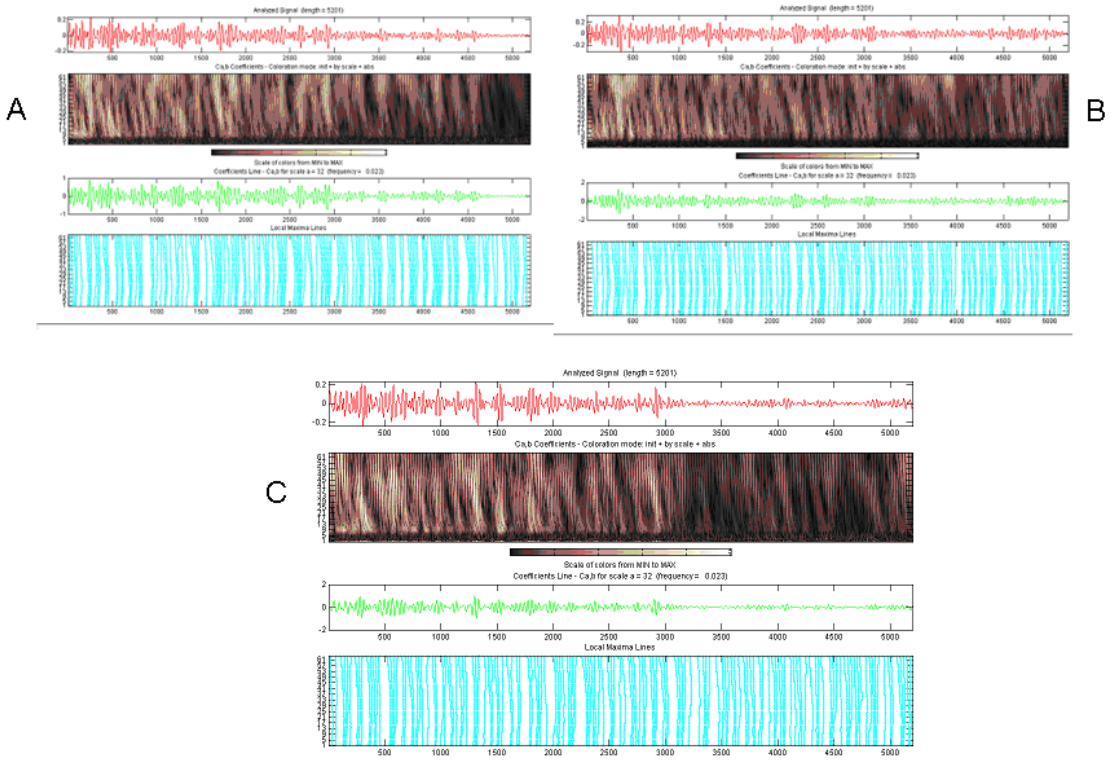

Figure 2.4: Signal's decompositions for three phantoms

The large number of scatterers (Phantom C) are "visible" on the two-dimensional picture of wavelet coefficient distributions - stronger fluctuations in the left side of pictures (the right side is less visible because we did not compensate the attenuation). The tendency to differentiate between "columns" in the pictures i.e. the same values of coefficients on successive scales, one can also notice in the case of moderately number of scatterers (Phantom B).

Fig. 2.4 represents the coefficients distribution of three types of signals' Hilbert envelopes from experiment 1. Red line on the top shows the envelope and the colored graph shows the intensity of wavelet coefficients. Horizontal axis corresponds to the time or to the shift parameter b of wavelet transform vertical axis corresponds to the scale parameter a (1.43). The intensity of coefficients connected with the energy are denoted by color scale, the brightest parts are the regions with the maximal energy and the darkest areas are the regions with minimal energy. The envelope and its coefficients on the top of Fig. 2.5 are obtained from type A signals, in the middle — to the type B signals and in the bottom — to type C signals.

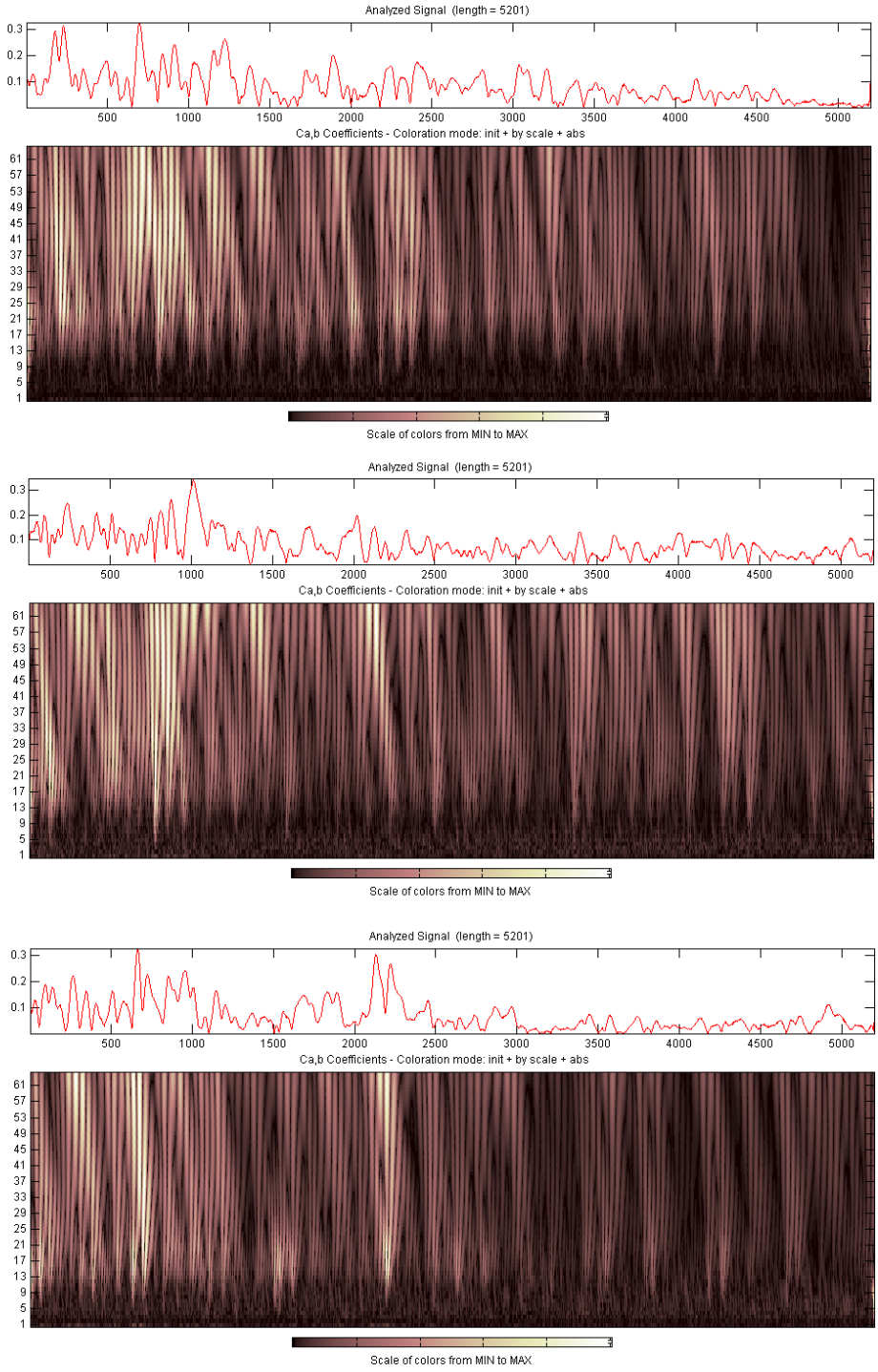

Figure 2.5: Examples of the coefficient distribution of signal's envelopes

2.2.3 Statistical Approach

Different statistical distributions may be used to estimate the RF signals (e.g. [2], [83] and others). As a proximity measure there was chosen mean squared error

$$MSE = \frac{1}{n}\sum_{i=1}^{n}\left(S(x_i) - PDF(x_i)\right)^2, \tag{2.1}$$

representing the square of distance between probability density function and our signal. In formula 2.1 $S(x)$ is initial signal taken in every sampling point x_i, $PDF(x_i)$ is a probability density function calculated in the same point. Table 2.2 shows the MSE value for Gamma, K and Rayleigh PDFs calculated for 5 level of signal's wavelet approximation for each type of phantom. The last part of table shows the mean value for each distribution and approximation level.

Phantom	Fitting to PDF	Pure signal	Level 1	Level 2	Level 3	Level 4	Level 5
A	Gamma	0.152	0.131	0.102	0.116	0.132	0.14
	K	0.156	0.133	0.103	0.117	0.131	0.137
	Rayleigh	0.646	0.388	0.233	0.197	0.169	0.161
B	Gamma	0.182	0.134	0.112	0.119	0.123	0.127
	K	0.200	0.144	0.116	0.122	0.124	0.128
	Rayleigh	0.372	0.237	0.164	0.148	0.139	0.136
C	Gamma	0.135	0.090	0.102	0.084	0.105	0.097
	K	0.146	0.095	0.103	0.085	0.104	0.098
	Rayleigh	0.358	0.203	0.162	0.116	0.125	0.139
Mean	Gamma	0.156	0.118	0.105	0.107	0.12	0.121
	K	0.167	0.124	0,107	0.108	0.12	0.121
	Rayleigh	0.458	0.276	0.186	0.153	0.144	0.134

Table 2.2: MSE for fitting to PDF functions

It follows from table 2.2 than the lowest values of mean MSE for each approximation level correspond to the PDF of Gamma distribution. That is why these parameters were calculated for each decomposition level for both experiments. Their dependence is shown in Fig. 2.6 for experiment 1 for approximation levels from 1st till 9th and in Fig. 2.7 for approximation levels from 3rd till 8th. Red points correspond to the RF signals obtained from phantom A, green points correspond to the RF signals obtained from phantom B, and blue points correspond to the RF signals obtained from

phantom C. On the horizontal axis there is shape parameter, on the vertical axis there scale parameter of Gamma distribution (1.66).

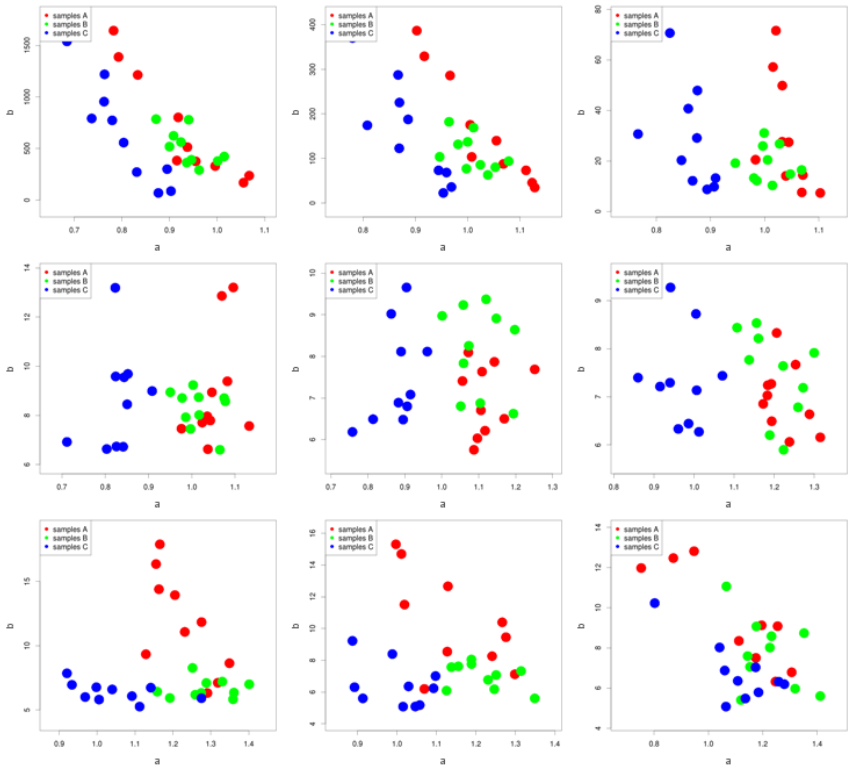

Figure 2.6: Parameters dependence of Gamma distribution for 9 wavelet approximation levels for signals of experiment 1

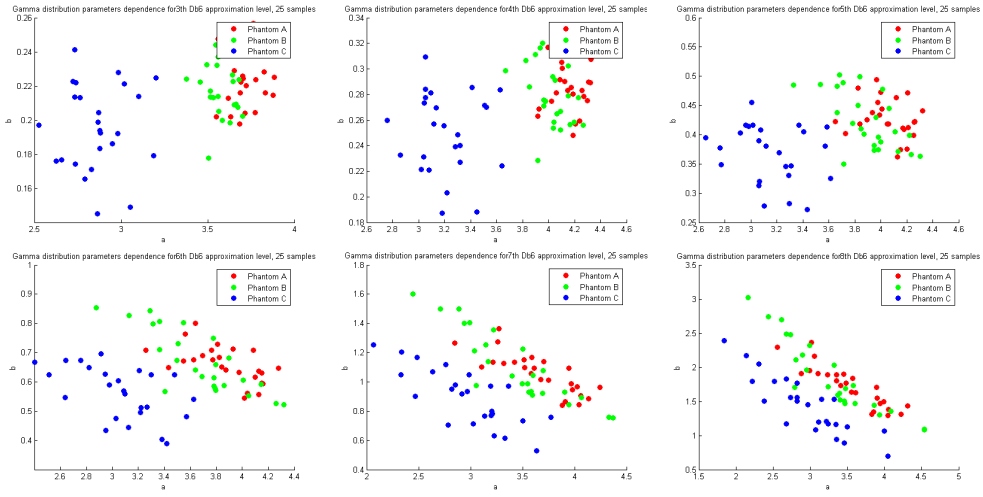

Figure 2.7: Parameters dependence of Gamma distribution for wavelet approximation levels from 3 to 8 for signals of experiment 2

The dependence of the parameters of Gamma distribution (1.66) had been used to see the difference between these phantoms. Similarities visible on the 2D plane of distribution the values of scale and shape parameters for both experiments. It may be noticed that the area of the points for phantom C (having the largest density of included particles) may be separated form others for levels from 3 to 6 for experiment 1 and for levels 3 and 4 for experiment 2. Thus, parameters location is a candidate for classification feature.

In Fig. 2.8 it is presented the pair-wise difference of the scale parameter a of Gamma distribution, its largest values are shown in the table. As it follows from Fig. 2.8, the maximal value this quantity reaches at the 4th approximation level, so it may be taken as an optimal one.

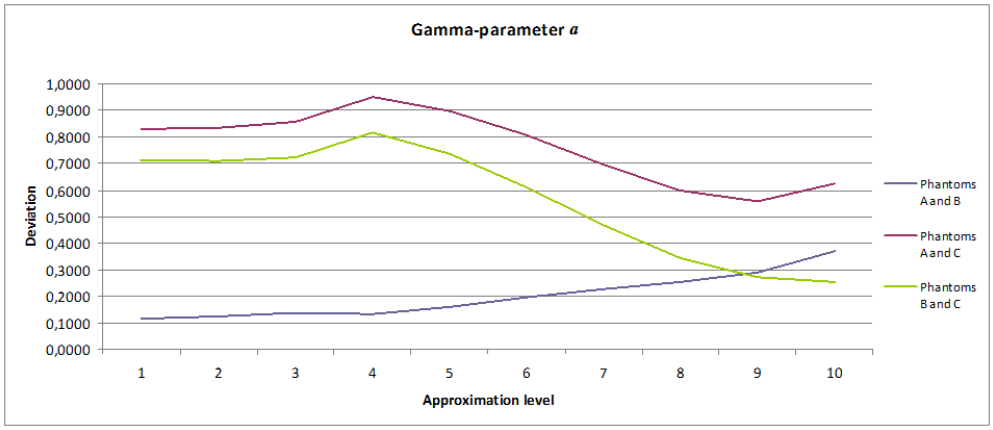

Figure 2.8: Pairwise deviation of Gamma parameter a

Maximal distance of Gamma parameter a is shown in the table 2.3.

Phantom A and B	Phantom A and C	Phantom B and C
0.13	0.95	0.81

Table 2.3: Maximum distance of pairwise deviation of Gamma parameter a

Similarly there were visualized the parameters dependence for spread parameter ω and shape parameter μ of Nakagami distribution (1.65) for wavelet approximation levels from 3 till 8 for signals from experiment 2 (see fig. 2.9):

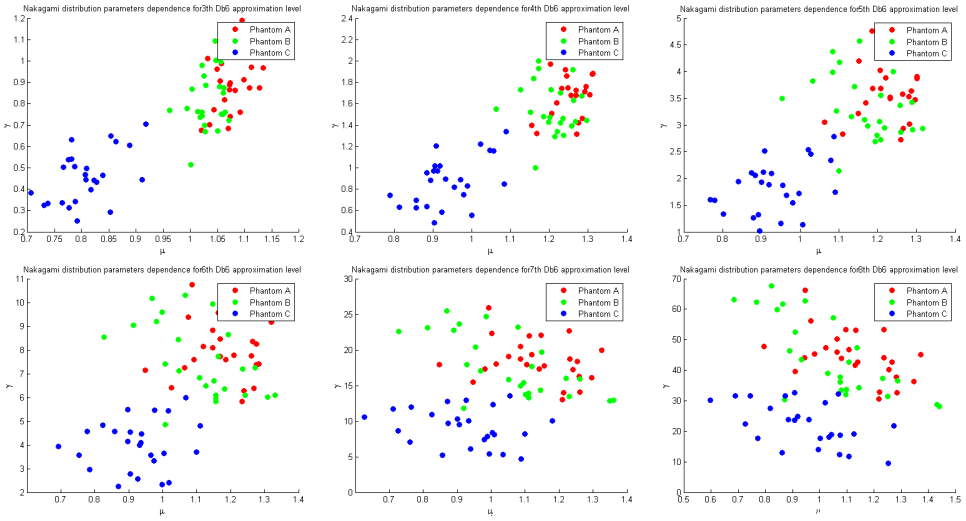

Figure 2.9: Parameters dependence of Nakagami distribution for wavelet approximation levels from 3 to 8 for signals of experiment 2

There it should be also possible to define the area of parameters values' separation, at least for 3th level approximation.

To summarize, the delimiting values of the shape parameters for Gamma and Nakagami distributions are given in the table 2.4. The measured data having the value of shape parameter that is less than the corresponding value form table 2.4 the for the chosen wavelet approximation level may be treated as RF signal obtained form the experiment of a phantom with the largest number of inclusions. Otherwise it may be concluded that the RF signal is obtained with low concentration of glass balls.

	Level 3	Level 4
Experiment 1, Gamma parameter a	0.92	0.99
Experiment 2, Gamma parameter a	3.30	3.65
Experiment 2, Nakagami parameter μ	0.95	–

Table 2.4: Delimiting values for distributions' scale parameter

Thus these parameters may be treated as a markers that allow to separate the RF signals obtained from the phantom with the highest concentration of scattering particles (Phantom C) from others (Phantom A and Phantom B).

2.2.4 Order Statistics

As the different technique there were also used the methods of nonparametric statistics that usually may be applied to the datasets with low quality

of data [55]. The idea of using the order statistics for detail coefficients of wavelet discrete transform was used in [51] for determination the breast lesion regions.

1. Each from 25 signals were decomposed into 10 levels by Daubechies 6 wavelets.

2. The detail coefficients for each decomposition level from 1 to 10 were calculated, $D_{j_n,i} = \sum\limits_{j>j_n} d_{j,i}\psi_{j_n,i}$.

3. Detail coefficients were collected for each type of signal (i.e. A, B, C) and for each decomposition level $D_{j_n} = \{D_{j_n,i}\}_{i=1}^{25}$.

4. The obtained datasets were normed with respect to its standard deviation (square root of the variance) $\overline{D}_{j_n} = \dfrac{D_{j_n}}{\sqrt{\mathrm{var}\,(D_{j_n})}}$.

5. The set were divided into 20 intervals to perform order statistics.

6. Quantiles for each type of signal A,B, C for the absolute value of approximation (1.47) and detail (1.46) coefficients of the decomposition levels from 1 to 10 were calculated.

   Quantiles are defined in statistics as points that divide the range of a probability distribution areas of with equal probabilities (see, e.g. [55]). A p-quantile z_p for the given probability density function $PDF(x)$ is may be obtained form the equation $PDF(z_p) = p$, where $0 < p < 1$ is fixed probability value.

Figure 2.10 shows the example of the quantiles for approximation (left image) and detail coefficients (right image) 6th approximation level. Horizontal axed denotes the probability values p, vertical axed denotes the quantiles. As it may be noticed, for detailed coefficient the difference of the the curves may visible only in the probability intervals for $p_{app} \in [0.1, 0.2]$ and $p_{app} \in [0.7, 0.9]$ while for approximation coefficients this interval is $p_{det} \in [0.4, 0.9]$. The read line correspond to the RF signal obtained from phantom A, the green line — from phantom B and the blue line — from phantom C.the

On Fig. 2.11 there are presented the mean values of obtained quantiles for each type of RF signals. Horizontal axis denotes the intervals defined at the step 5 of the algorithm. The whole area included 20 intervals, but on the graphs there are depicted only area with visible differences, i.e. intervals from

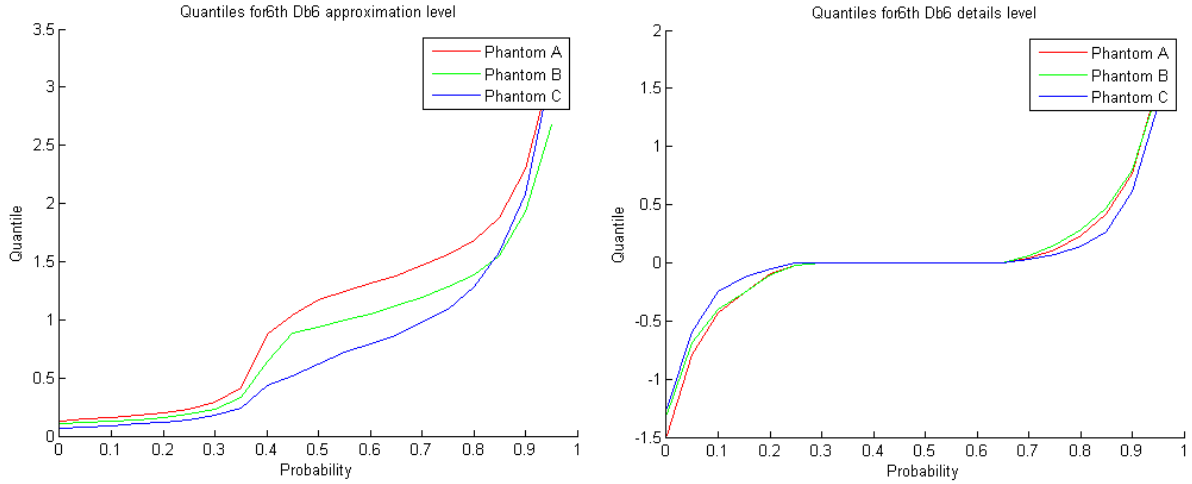

Figure 2.10: Quantiles for approximation and detail coefficients for 6th approximation level

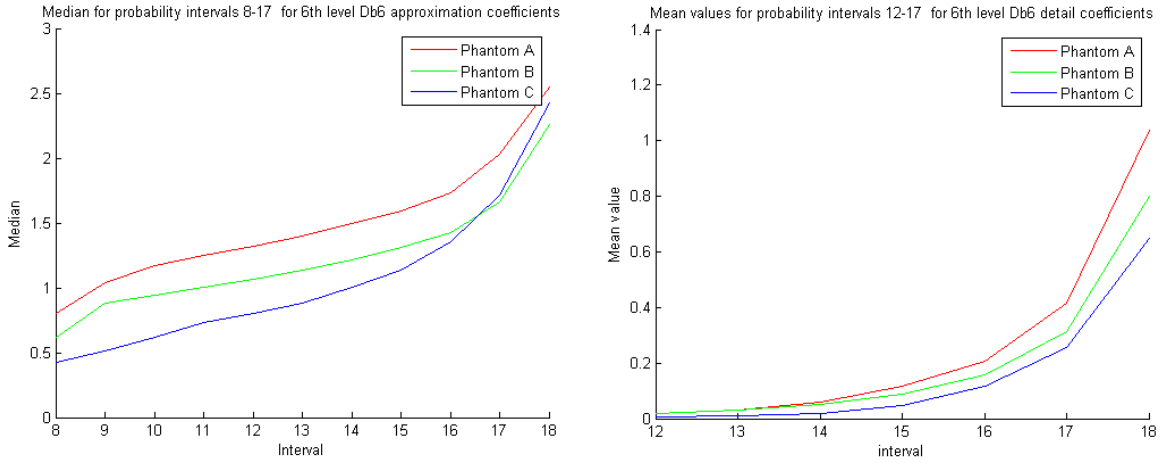

Figure 2.11: Mean values for probability intervals for approximation and detail coefficients of 6th level

8 to 18 for approximation coefficients and from 12 to 18 for detail coefficients. The RF signals are denoted by the same colors as in Fig. 2.10.

It may be concluded that the possibility to differ the RF signals for each type of phantom occurs for the intervals from 8 to 16 or for quantile order $p_{app} \in [0.4, 0.8]$ for approximation coefficients and for intervals from 16 to 18 or for quantile order $p_{det} \in [0.8, 0.9]$ for detail coefficients. the obtained

2.3 Results

1. Values of shape parameters of Gamma and Nakagami distribution may be treated as the quantitative parameter, i.e. a marker which able to separate the phantom with the largest concentration of included particles from others:

   - for 3rd approximation level:
     - for experiment 1 and Gamma parameter $a < 0.92$,
     - for experiment 2 and Gamma parameter $a < 3.3$,
     - for experiment 2 and Nakagami parameter $\mu < 0.95$,
   - for 4th approximation level:
     - for experiment 1 and Gamma parameter $a < 0.99$,
     - for experiment 2 and Gamma parameter $a < 3.65$.

2. Additionally, the mean vales of quantiles for approximation and detail coefficients for 6th level wavelet approximation are also the quantitative markers of separating the each type of phantom, namely:

   - the quantile for approximation coefficients $z_{p_{app}}$ of order $p_{app} \in [0.4, 0.8]$,
   - the quantile for detail coefficients $z_{p_{det}}$, of order $p_{det} \in [0.8, 0.9]$.

3 Temperature Changes Differentiation

The main idea of this chapter is to examine the temperature changes in tissue during the heating process by the registering the changes in the ultrasound echo signals. The research is in area of modern ultrasonic thermometry which is a non-invasive tool concurent to very expensive and not always possible to be used magnetic resonance temperature imaging. Ultrasound thermometry will also be used in ultrasonic hyperthermia to monitor the level of tissue heating within the patient's body during the course of e.g. ablation of cancerous tumors. Also the mild hyperthermia used in immunotherapy needs the precise temperature control, made in [6], [75], [76].

During our investigation special phantom of soft tissue was fabricated to examine the temperature changes of the backscattered acoustic signal under the heating process [23]. We explore the fact that the changes in texture of material during heating appear. The ultrasonic acoustic signals, being recorded during the heating of samples (made from a soft tissue in vitro or soft tissue phantom), should be associated with the local temperature increase.

The aim of the chapter is to display that using wavelet transformation of ultrasound echo signals we are able to find parameters which in a quite precise way are markers of temperature increase. The ultrasound backscattered signal also this which is registered during heating has a statistical nature as it is formed from the backscattering signals scattered from spatially randomly distributed scatterers located inside the medium. As a result statistical properties of a signal should be strongly connected with the variations of in random scatterers distribution in agreement with temperature variations.

Standard clinical B-scan imaging uses the properties of envelope of RF (radio frequency) signal rather than a signal itself, because a phase is assumed to be uniformly distributed, for details see Chapter 1.3., so the phase does not contain in any significant information.

In what follows we look for statistical parameters of signals envelopes which are sensitive for temperature increase using wavelet methods. It is already known that the statistical distribution parameters modeling the envelope statistics preserves information about so called "effective density of scatterers". The signal's envelope values is modelled as random variable distributed as K-distribution if the empirical histogram of the envelope signal is close to the probability distribution function of K-distribution (cf. [57], [58]). One can to proof it by statistical testing with performing e.g. Kolmogorov-Smirnov test [55]. The parameter proportional to the "effective

density of scatterers" is just the size parameter of K-distribution and can be approximated from the first four moments of random envelope signal, cf. Section 1.5.3. It is stated the hypothesis that this parameter is sensitive for temperature changes, so correlated with structural changes of the sample, and hence correlated to the changes of K-distribution shape parameter. The proof of the hypothesis will be given by performing numerical calculations on real signals collected during experiment described below. It will be also shown that the temperature rise can be described by changes of the size parameter of 5th level of wavelet approximation of the envelope. The resulting relationship i.e. temperature rise curve during heating is more close to temperature rise curve measured by thermocouple than the same relationship calculated directly from the signal envelope itself.

The sample datasets were obtained from two experiments that were performed independently and have the similar general technique and described in details in papers [21] and [42]. Backscattered RF Signals registered by Transmitter-receiver JSR Ultrasonics DPR 300 Pulser/Receiver and US head of central frequency 6MHz, diameter 9 mm, the focal length 62 mm. The temperature within the sample has been measured along the beam axis at different distances from the ultrasonic head by thermocouples.

3.1 Experiment 1. PVA Phantom

3.1.1 Experiment Description and Pre-transformations

The sample which has been used in experiment was a tissue phantom made from PVA (Polyvinyl Alcohol Cryogel). This material consisted of 10% (by weight) aqueous solution of polyvinyl alcohol. Samples produced from PVA are widely used in clinical ultrasound and MR (magnetic resonance) imaging, see [57] as the acoustic properties of the material are similar to the acoustic properties of soft tissue. The cylindrical sample of radius 40 mm, thickness of 18 mm with metal reflector at one end was immersed in a water bath, which was kept in a thermostat whose temperature was regulated. The thermostat was set so that within one hour the temperature of the bath increased linearly from $T_0 = 20.6°\text{C}$ to $T_1 = 48.8°\text{C}$. Next heating was switched off and after 2 hours temperature of water reached $T_3 = 25.8°\text{C}$ (table 3.1). Data

Start	After 1 hour of heating	In 3 hours
20.6°C	48.8°C	25.8°C

Table 3.1: Temperature values in experiment 1

were collected by ULTRASONIX L14-5/38 head at a frequency of 8 MHz.

Transmitted pulse comprises 2 periods of the sine wave pulse duration of 0.25 microseconds. At the time of 1 hour and 2 hours of heating/cooling RF (Radio Frequency) signals were recorded every half minute (361 times). Identification of temperature scale and time scale has been performed with data from finite element method numerical simulation using Abaqus software (see [21]). The obtained dependence of temperature versus time is shown in Fig. 3.1.

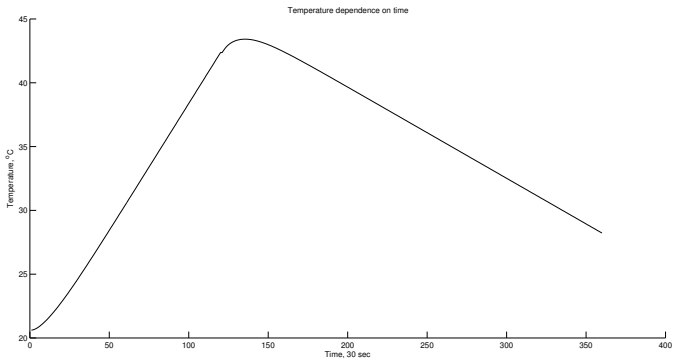

Figure 3.1: Abaqus-simulated dependence of temperature on time

It may be noted from Fig. 3.1 that after switching off the heating ($t = 120$) the temperature of the phantom still increases for some period.

The recorded data had frequency of signals acquisition 30 frames per second. Data RF signal has the form of the analytical signal (complex values), which module gives the envelope the RF signal as a matrix $1001 \times 501 \times 361$.

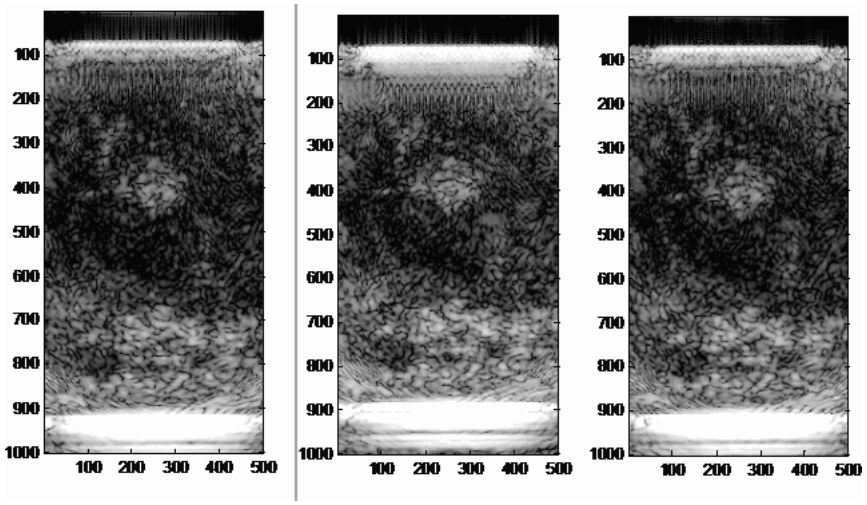

Figure 3.2: B-mode of the phantom in 3 different temperature phases

Figure 3.2 represents the three pictures (UGS B-modes) of the phantom at initial moment, after first hour of heating and at the end of the experiment. The temperature increase in not visible here.

Before performing the wavelet decomposition and its statistical analysis the data set was modified by following transformations:

1. The experiment data array of size $1001 \times 501 \times 361$ had been reduced to the array $601 \times 501 \times 361$ by removing 200 points from each side. We

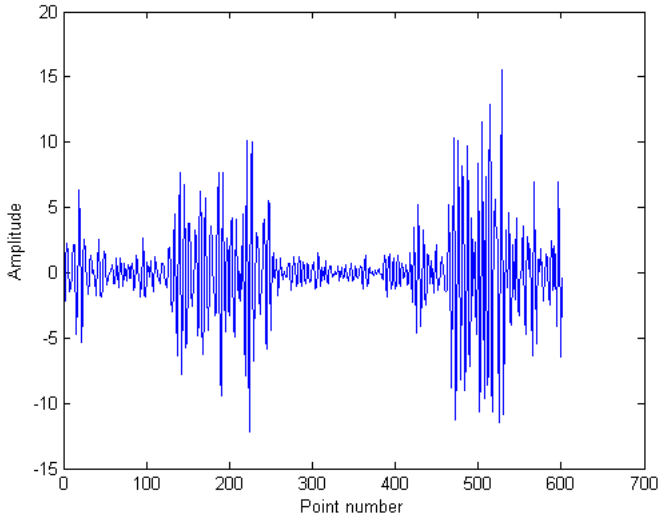

Figure 3.3: Example of RF signal, image 160 line 250

assume the initial data as a discrete function $f(x, y, t)$, where $x \in X$, $X = \{0, \cdots, 600\}$ represent points, $y \in Y$, $Y = \{0, \cdots, 500\}$ represent lines of data, $t \in T$ is a time variable or a number of image, $T = \{0, \cdots, 360\}$. Fig. 3.3 represents the example of the signal function $f(x, y_0, t_0)$ for $y_0 = 160$, $t_0 = 250$.

2. Zero-phase digital filtering with the Butterworth filter had been performed. Additionally a filter, which reduces a tendency of the changes with depth, was used. The compensated signal will be denoted as $\tilde{f}(x, y, z)$. We consider the obtained signal as a function $f(x, y, t) = f_{y,t}(x) = f_y(x, t)$, $x \in X$, $y \in Y$, $t \in T$.

3. Hilbert (or RF) envelope was constructed with respect to the variable x. Let $\tilde{f}(x, y, z) = \tilde{f}_{y,z}(x)$, then the Hilbert envelope represents $\tilde{f}_{y,z}(x)$, $x \in X$, the absolute value of the Hilbert transform of real-valued function

$$H(x) = \frac{1}{\pi} p.v. \int_{-\infty}^{\infty} \frac{f_{y,t}(x')}{x - x'} dx':$$

$$\tilde{s}(x, y, t) = \tilde{s}_x(y, t) = |f_{y,t}(x) + iH(x)|.$$

The signal example together with its Hilbert envelope (red line) are

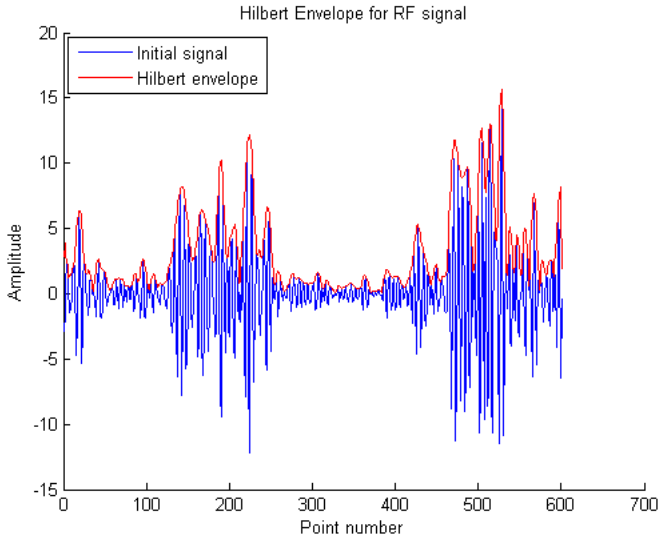

Figure 3.4: The examples of RF signal and its Hilbert envelope

shown in the Fig. 3.4.

4. The data were averaged with respect to each line $\tilde{s}_{av}(x, \cdot, t_0) = \dfrac{\tilde{s}(x, \cdot, t_0)}{E(\tilde{s}(x, \cdot, t_0))}$, where $E(\tilde{s}(x, \cdot, t_0))$ is a mean value with respect to variable x for each $t_0 \in T$.

5. In order to have enough high number of values in the statistical ensemble the data of each line had been considered together. The 361 "long", signals with length equal to 300969 points had been constructed: $\overline{S}(x, t) = \overline{S}_x(t)$, $t \in T$, $x \in X'$, $X' = \{0, \cdots, 300969\}$.

6. "Long" signals has been normalized with respect to variable x:

$$S(x, t) = S_t(x) = \frac{\overline{S}_t(x)}{\max\limits_{x \in X'} \overline{S}_t(x)}.$$

The result of the pre-transformation steps for the image $t = 160$ is shown in the Fig. 3.5. These data are concerned as initial for the following wavelet and statistical analysis.

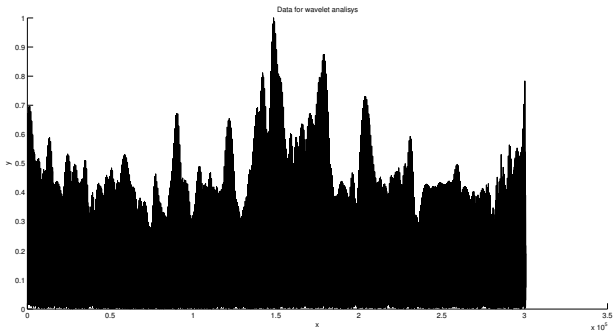

Figure 3.5: Signal function after pre-transformations

3.1.2 Temperature Increase Detection

As it have been stated in section 1.4.3, the Daubechies 6 family had been chosen as the analyzing wavelets. The choice of the analyzing wavelet was based on the shape of the impulse which was used in the described above experiment.

There was performed a decomposition by the Daubechies 6 wavelet of $S_t(x)$, for each $t \in T$ up to the 10th level, then there was obtained the reconstructed signal and the approximation coefficients up to the 10th level. The 5th level was chosen as the most informative one. Fig. 3.6 represents the example of the wavelet decomposition of the signal for $t = 120$.

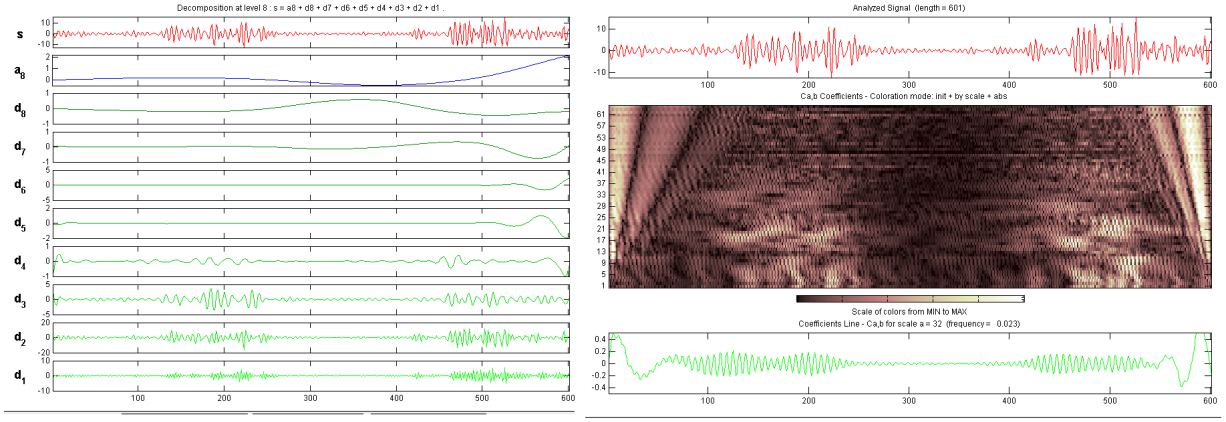

Figure 3.6: Example of Daubechies 6 wavelet decomposition and coefficients distribution for frame $t = 120$

The goal of this algorithm is to separate in time the period when the phantom was heated, when its temperature continued to arise and then it was decreasing.

The parameters α_0, b_0 of K-statistics were calculated by (1.63)–(1.64) for the approximation of signal $S_t(x)$ on the 5th level by Daubechies 6 wavelets for each $t \in T$ as well as for the reconstruction of the signal $S_t(x)$ for the 5th level by Daubechies 6 wavelets for each $t \in T$. The dependence of $b_0(\alpha_0)$ on time and on temperature was visualized as a three-dimensional graph, the dependence of the parameter α_0 on time and temperature were build also (see Figs. 3.7–3.8).

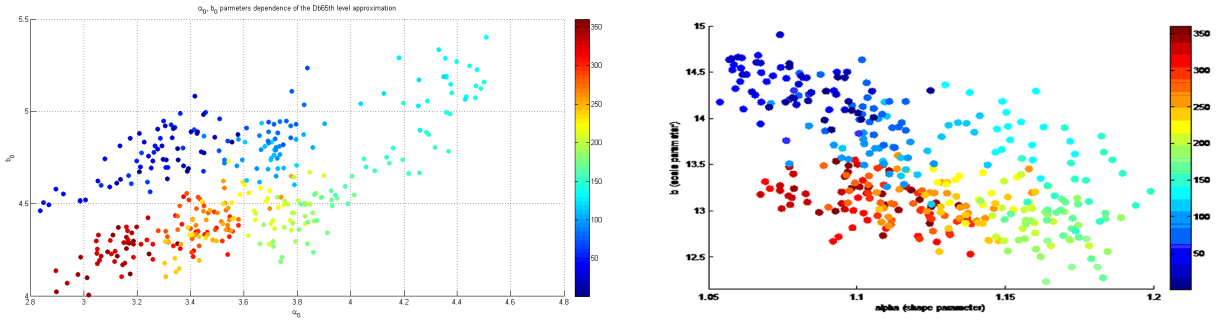

Figure 3.7: K-statistics parameters dependence $b_0(\alpha_0)$ on time for the 5th level approximation and for the initial experimental data

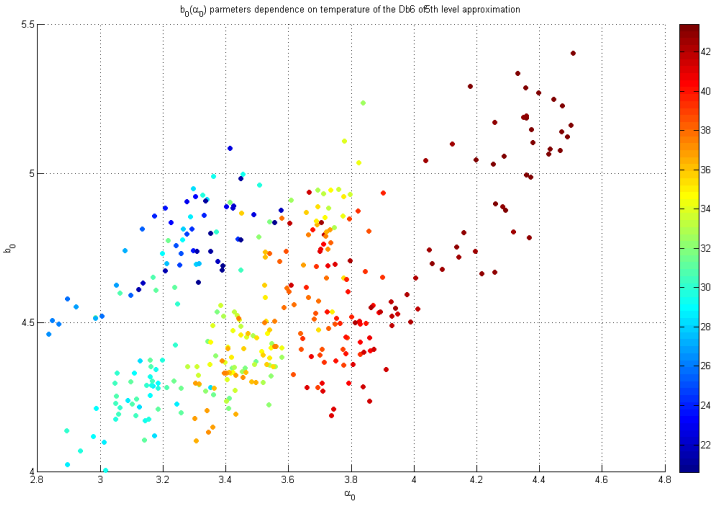

Figure 3.8: K-statistics parameters dependence $b_0(\alpha_0)$ on temperature for the 5th level approximation

Fig. 3.7 shows two approaches to find the dependence for K-statistics parameters $b_0(\alpha_0)$ for the considered experiment. Left image displays the $b_0(\alpha_0)$ dependence on time for 5th approximation level, and the right image shows

this dependence for initial data obtained in [42] without using wavelet approximation. Horizontal line corresponds to the scale parameter α_0, vertical axis corresponds to shift parameter b_0 and time scale is represented by color. It may be noticed performing the 5th level of Daubechies 6 approximation allows to separate areas of different time intervals with the same temperature value that marked in the Fig. 3.7 by blue and red colors.

Fig. 3.8 visualizes the dependence of the statistical parameters b_0 and α_0 on temperature. As in previous image, the horizontal axis corresponds to the scale parameter α_0, vertical axis corresponds to shift parameter b_0. The temperature values are indicated by color and they changes from dark blue (corresponding to the coldest area) to dark red (corresponding to the hottest area).

As a result the whole area of graph have been decomposed into 4 regions corresponding to the different phases of the heating process (Fig. 3.9):

$$\begin{aligned} S_1 &= \{(\alpha_0, b_0) : 2.8 \leq \alpha_0 \leq 4, 4.5 \leq b_0 \leq 5.5\}, \\ S_2 &= \{(\alpha_0, b_0) : 4 \leq \alpha_0 \leq 4.6, 4 \leq b_0 \leq 5.5\}, \\ S_3 &= \{(\alpha_0, b_0) : 3.6 \leq \alpha_0 \leq 4, 4 \leq b_0 \leq 4.5\}, \\ S_4 &= \{(\alpha_0, b_0) : 2.8 \leq \alpha_0 \leq 3.6, 4 \leq b_0 \leq 4.5.\} \end{aligned} \tag{3.1}$$

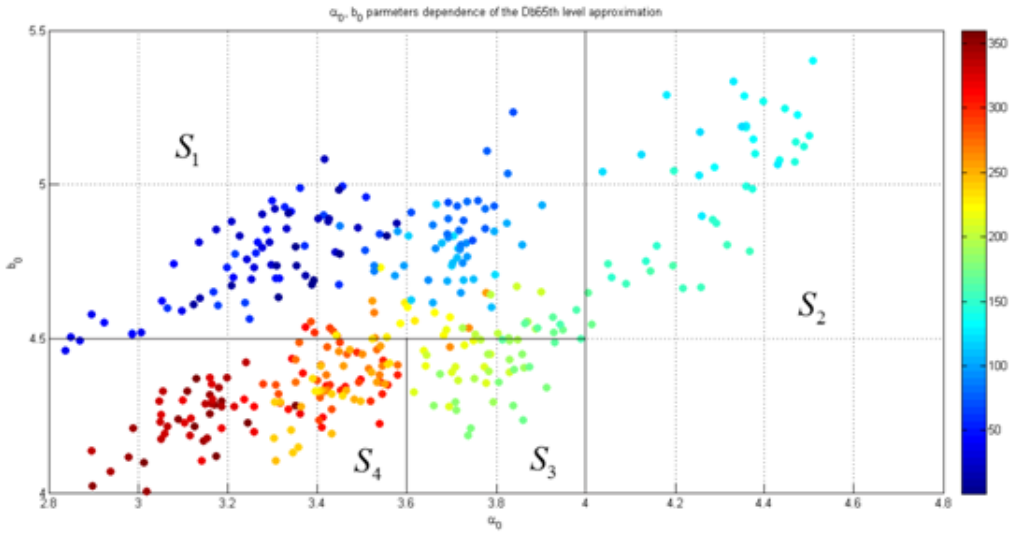

Figure 3.9: Separation the regions of different temperature during the heating/cooling process

Region S_1 contains 114 of 138 points corresponding to the time period of 1 hour heating when the temperature changed from 20.6°C to 42.37°C according to Fig. 7. The temperature range of 21.73°C in this region can be

divided into some smaller ranges. From practical point of view to investigate the area of temperature higher then 42°C in useless, because it is not safe for living tissues. Thus greater resolution is not needed.

Region S_2 contains 40 points corresponding to the time values from the interval when the heating process was finished but the temperature inside phantom was still increasing due to its physical properties. These are points of the highest temperature from 42.37°C till 43.16°C that should be distinguished.

S_3 is an intermediate region. It contains 60 points from the time period of 1/2 hour.

Points in the region S_4 correspond to the end of the experiment. The temperature does not reach the initial value (the start temperature was equal to the 20.6°C, the final equal to the 25.8°C). And this fact may be explained by the changes of physical state of the phantom under the heating.

There are important differences between two images in Fig. 3.7 e.g. the statistical parameters of the original signals the values of parameters (points) with the highest temperature level are not well localized as it takes place in area S_2 on Fig. 3.9. Similarly, the other ranges of temperature have worse "resolution" than resulting from the right image of Fig. 3.7.

The same trend may be also stated for the dependence α_0-parameter of K-statistics on time (Fig. 3.10).

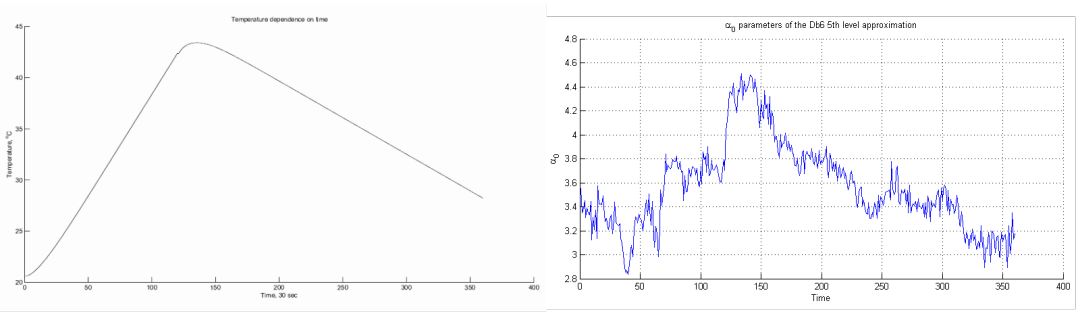

Figure 3.10: Temperature-time dependence and α_0-time dependence for 5th approximation level

Left image of Fig 3.10 displays the numerically modelled temperature dependence on time, right image shows dependence of the parameter $\alpha_0(t)$ on time for 5th approximation level using Daubechies 6 wavelets. Both graphs reach a maximal value at the same point.

3.2 Experiment 2. Tissue Sample

3.2.1 Experiment Description and Pre-transformations

The pork sample has been heated by the ultrasound beam produced by spherical transducer with irradiation with 2 different powers: of 4W and 6W. During 10 minutes of heating and 10 minutes of cooling the temperature changes were recorded using thermocouples and registered by the USB module-TEMP. The temperature values had been written each 5 seconds.The shape of the obtained scanned image is a rectangle 36 mm x 16 mm. The detailed description of the experiment is given in [21] and its parameters of are represented in table 3.2.

Power, W	4	6
Tension, mVpp	454	588
Max temperature increase, ΔT, °C,	17.6	25.6
Achieved max temperature, T, °C,	36.6	46.6
Transducer distance, mm	25	25

Table 3.2: Parameters of the soft tissue heating experiment

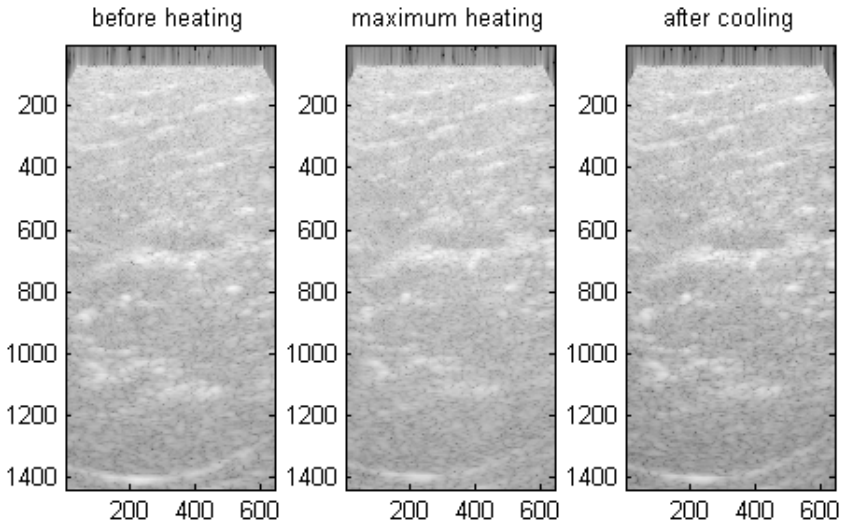

Figure 3.11: B-modes of the tissue sample in 3 different temperature phases.

Examples of experimental B-modes are shown in Fig. 3.11. The left image corresponds to the initial phase of heating process, image in center displays

the B-mode registered after 10 minutes of heating and the last B-mode is registered after 10 minutes of cooling.

3.2.2 Temperature Increase Detection

Initial data may be treated as three-dimensional array 1441 points (variable x), 641 lines (variable y), 241 images or time moments (variable t). The pre-processing procedure was analogous to one used for PVA phantoms in previous section. Fig. 3.12 displays the example of prepared for wavelet and statistics analysis signal.

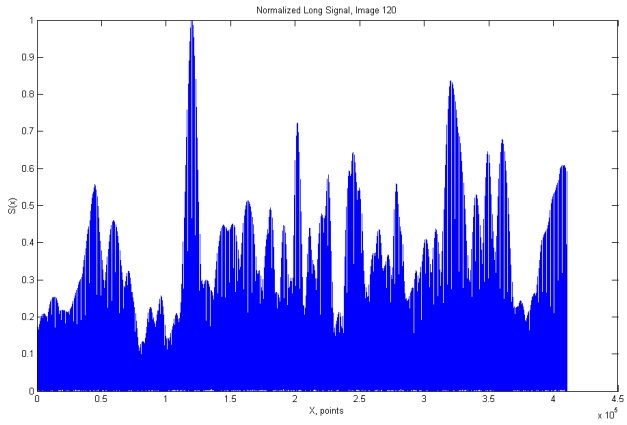

Figure 3.12: Example of analysed signal

Fig. 3.13 shows the temperature distribution on α_0 and time dependence for Daubechies 6 wavelet approximation (left) and with wavelet reconstruction (right). The difference between the reconstruction of signal and the initial signal itself are of order 10^{-12}–10^{-13}, so the reconstruction may be considered as the pure signal.

Following the scheme used for the PVA phantom above there was evaluated the dependence of scale parameter α of K-statistics on time (3.14).

Fig. 3.14, left, shows the simulated temperature using Abaqus 6.12 software (DS Simulia Corp.) (see [42]). The right graph represents the dependence of α_0 on time. Green line corresponds to the power value of 6W and blue — to the power of 4W. As is may be seen, the general trend preserves and all curves reach their maximal values at the same time point.

Looking for other characterization of the temperature changes in heating-cooling process there was also made an attempt to investigate the polynomial approximation of 10th degree of the Fourier transform absolute value of 6th-level Daubechies 6 approximation for different phases of experiment. The

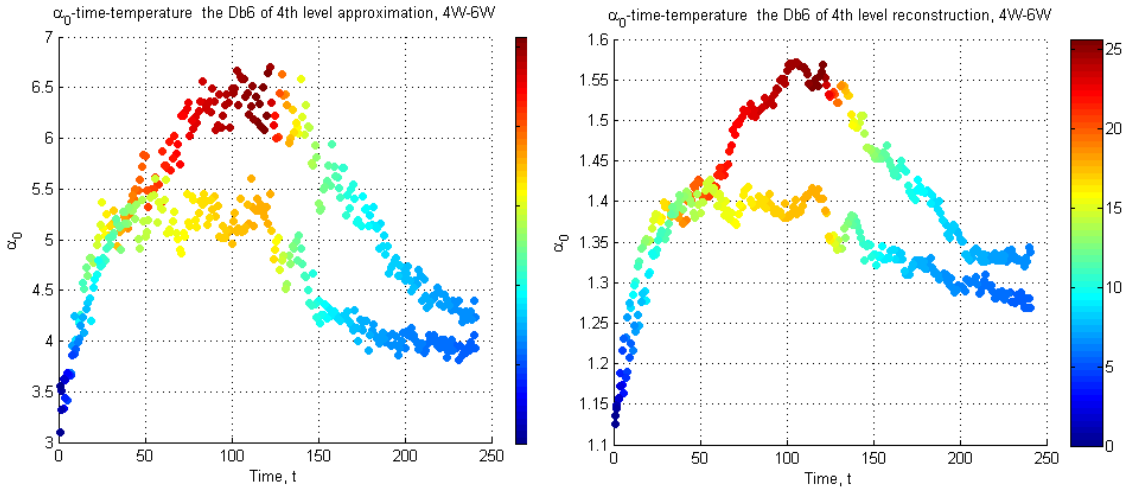

Figure 3.13: Temperature distribution: for wavelet approximation and for wavelet reconstruction

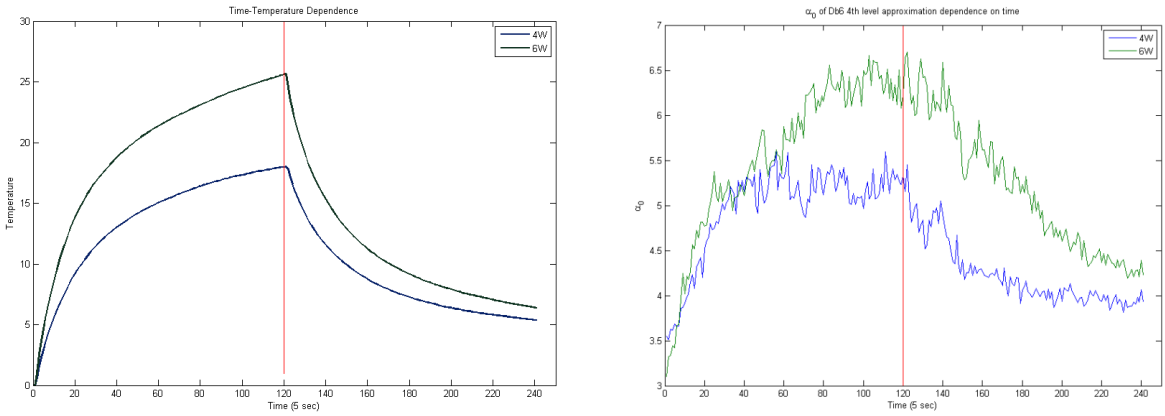

Figure 3.14: Temperature-time dependence and $\alpha_0(t)$ dependence for 5th approximation level

result is shown in Fig. 3.2.2. The signals were taken with step of 60 images, their accordance with the temperature value during the experiment is given in table 3.3.

Image number	1	61	121	181	241
Temperature, ^{o}C	20	35,2	38	27.6	25.6

Table 3.3: Temperature values for several images

The right image of Fig. 3.3 shows the polynomial approximation of 10th degree of the Fourier transform absolute value of 6th-level Daubechies 6 ap-

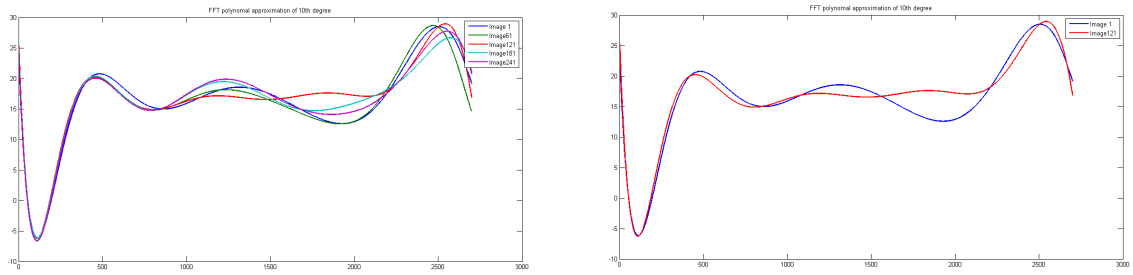

Figure 3.15: Polynomial approximation of 10th degree for the6th-level approximation of absolute value of Fourier transform

proximation for image 1 (20^oC), and middle time of the heating process, Image 121 (38^oC).

3.3 Results

The results of this subsection can be summarized as follows:

1. The dependence of parameters α_0 and b_0 of K-statistics on tome allow to separate the regions with different temperature levels.

2. The fact that to obtain final result we have used about 13% of data which are contained in the whole envelope but still retains the important signal characteristics is very important for further study when we would like to operate with much more numerable data.

3. The functional dependence on temperature of both statistical parameters illustrated on the 2D image with coloured points correlated to temperature scale allow to track the direction of rising up and following down of points (equivalently, of rising up and following down of parameter values) in agreement with heating process. This was not possible in the case when the results are obtained in the analogous way by using data from signal envelope without wavelet transformations. Summing up, the obtained results are more close to real heating-cooling process at least in analyzed range of temperature.

4. The process of compression is just a special low-filtering process of initial signal. The 6th and higher levels of approximation did not provide to acceptable results.

4 Differentiation of Scatterers' Randomness Type Through Numerical Model of Random Structures

The aim of this Chapter is to study the wavelet transformation of backscattered signal numerically generated from different types of scattering media. The random scattering media are also numerically generated. I follow the numerical program constructed by J. Wócik [85] and the calculations in this Chapter were performed with the use of Engineering Math Software, Mathcad 14.0 (PTC Inc.).

4.1 Numerical Models of Random Media

4.1.1 Construction Medium with Random Structure

The medium which we can generate is assumed to be composed of scatterers embedded in a homogeneous 3d matrix, called host medium. First, the periodic distribution of points in three-dimensional space is generated. The points are located in the centers of cubic cells which fills the space. The cells form parallelogram in the Cartesian coordinate system (X, Y, Z), consisting from 41 cells in Z direction and 11 cells in each X and Y direction. Each cube of dimension 0.0005 m contains one spherical scatterer, which is situated in the cell center and has the diameter of $a1 = 0.00005$ m. The local physical properties of the obtained two-phase medium such as, the density and sound velocity of the host medium and of scatterers are defined. The example of the medium is shown in Fig. 4.1 on the left.

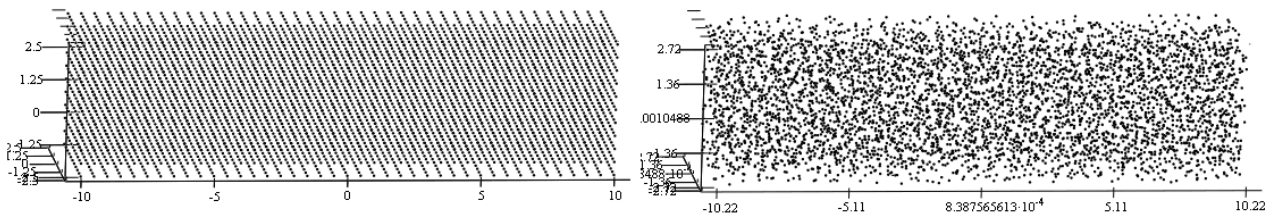

Figure 4.1: Examples of constructed media without random geometry and with random geometry component

Media which are not periodic but random are constructed by adding random fluctuations of the scatterers position in the periodic cell, scatterer's

size, their density and sound velocity. We define four types of the media:

1. *Without random components*, i.e. the periodic structure. The principle of construction is described above.

2. *With random geometry component.* The numerical model of the medium is generated by moving the scatterer from the center of the periodic cell by the random vector defined below

$$\delta X_j = \begin{pmatrix} \delta z_j \\ \delta x_j \\ \delta y_j \end{pmatrix},$$

   where δz_j, δx_j, δy_j are independent random variables, uniformly distributed in the intervals

$$[-0.45 z_j, 0.45 z_j],\ [-0.45 x_j, 0.45 x_j],\ [-0.45 y_j, 0.45 y_j]$$

   correspondingly and $j = 0, \ldots, 4960$ is index of scatterers numbering. The one realization of such medium is presented in Fig. 4.1, on the right.

3. *With random physics component.* The media s generated by the scatterers possessing

   - the random radius $ar_j + \delta ar_j$,
   - the random density $qr_j + \delta qr_j$,
   - the random speed of sound $cr_j + \delta cr_j$.

   where $j = 0, \cdots, 4960$. The random fluctuations are normally distributed with mean value $\mu_{qr_j} = \mu_{cr_j} = \mu_{ar_j} = 0$ and standard deviations $\sigma_{qr_j} = 0.05 qr_j$, $\sigma_{cr_j} = 0.05 cr_j$, $\sigma_{ar_j} = 0.025 ar_j$, where ar_j, qr_j, cr_j are initial values of scatterers' radius, density and speed of sound respectively.

4. *With random geometry and physics component.* It is a combination of type 2 and type 3, i.e. has both randomly distributed geometrical and physical properties.

Let us notice, that the random radius of scatterer classified here as "physical" property is not a geometrical one, because it is proportional to the scatterer cross-section and it is not connected with geometrical distribution of scatterers' centers.

4.1.2 Backscattered Signals from the Random Media

Next step is to simulate numerically the transmission of ultrasounds waves coming from the transducer, being scattered in all directions and propagating through the inhomogeneous structure.

Initial impulse is formed from three sines and triangular envelope, as follows $Env(t, dur, n) = 1 - 2\left(\frac{t - 0.5dur}{dur}\right)^n$ as a polynomial power n and duration time dur with time-variable t :

$$Fe(t, w, dur, n) = Sign \cdot Env(t, dur, n) \sin(w(t - 0.5dur)),$$

where $Sign$ is equal 1 or -1, parameter w depends on the carrier frequency $N_{car} = \frac{\lambda_0}{\lambda_{car}} = 330$, the duration time $T_{dur} = \frac{LC \cdot 2\pi}{N_{car}}$, where LC is number of cycles of the impulse, which is supposed here to be equal to 3. The obtained impulse (denoted by black line) and its Hilbert envelope (denoted by dotted red) are visualized in Fig. 4.2.

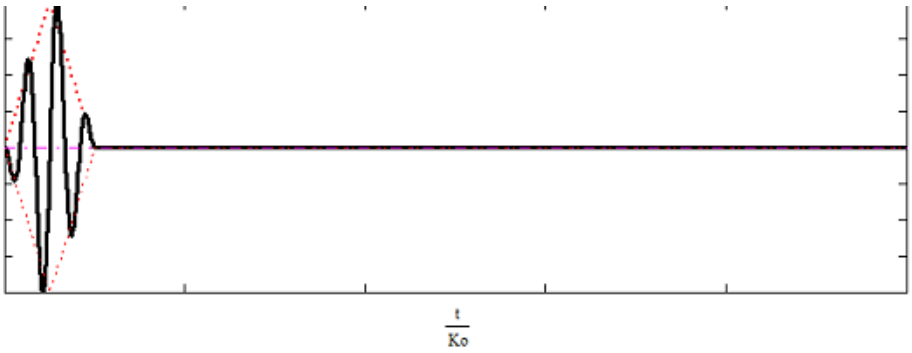

Figure 4.2: The initial impulse and its Hilbert envelope

The incident wave is assumed as a plane wave, backscattered signal is formed under the assumption of the physical quantities having the values:

- the speed of sound in host medium $c_0 = 1500$ m/s,
- the speed of sound in the scatterers $c_1 = 1600$ m/s,
- the density of the host medium $q_0 = 1000$ kg/m^3,
- the density of the scatterers' material $q_1 = 1200$ kg/m^3,
- repetition in space $\lambda_0 = 0.099$ m,

- the dimensionless wave vector is $K_0 = \dfrac{\pi}{\lambda_0} = 31.3$.

We examine the very simple case in order to find in the backscattered signal fundamental parameters depending only on the sample properties, making of possible to distinguish between the randomness of scatterers distribution. It is assumed that a wave incident on a sample of "material" is a plane wave, and backscattering signal from the sample is received by point receiver, symmetrically located with respect the sample cross-section. Effects of echoes waves summation (integration) on the transducer face, which always appear when the signals are received by the imaging linear ultrasonic transducers, or any other transducer with finite face area are excluded. Taking into account in the model only plane waves also the effect of beam focusing is omitted.

Such idealization of backscattered echo can be more useful under the following interpretation. When the actual ultrasound echo signal is registered from a certain depth, we can assume that near the focus the signal consists of a sum of plane waves and, additionally, if the distance of the imaging tissue to the transducer face is sufficiently large (the far field approximation), the signal reception can be approximated by the point receiver.

Examples of backscattered signals from periodic medium and the three randomly inhomogeneous media and the are presented in the Fig. 4.3.

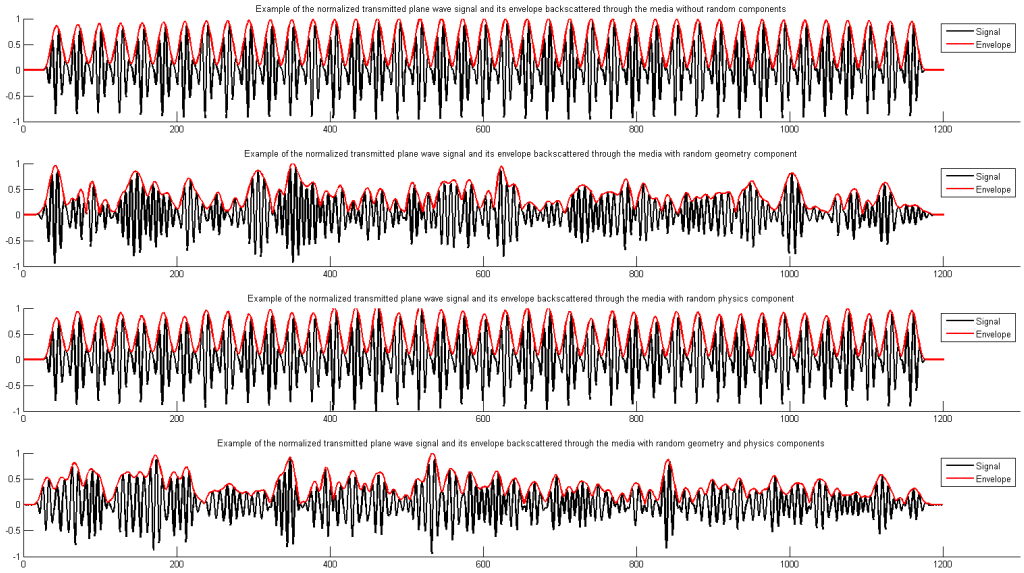

Figure 4.3: Examples of signals for transmitted plane wave backscattered by randomly inhomogeneous media

The black line in each picture denotes the Hilbert envelope of the signal that will be considered further as data for the spectral and wavelet analysis. We will denote the type I signal corresponding the the 1st medium, type II — to the 2nd medium and type III — to the 3rd medium, IV — for the 4th medium. The image corresponds to I, II, III, IV types of media from the top to the bottom, red line indicates the corresponding Hilbert envelope.

4.2 Differences Detecting

4.2.1 The Spectral And Wavelet Analysis

First the spectral analysis of three type of signals was performed. The spectrograms corresponding to the I, II, III types of signals are presented in the top row of Fig. 4.4, from left to right. There horizontal axis denotes time, the vertical axis denotes the frequency range, and the color shows the quantity of the Fourier coefficients. As one may notice, the are visible difference between the medium 2, but for media 1 and 3 the spectrogram gives no distinguishing features. Fig. 4.5 shows the spectrum lines for every signal.

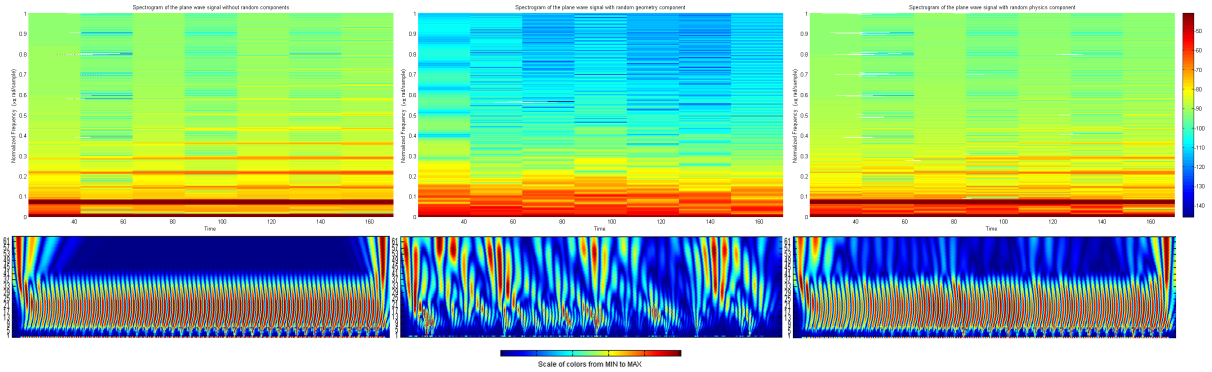

Figure 4.4: Spectrogram and scalograms for envelopes

On the horizontal axis in bottom row of Fig. 4.4, there are values of the wavelet transform shift coefficient b_k that mean time, on the verticals axes are values of the scale coefficient a_k, the colors represent the percentage of energy from dark color to light. Coefficients a_k and b_k are obtained form the reconstructed signal according to equality (A.14).

Then we start to analyse the signals were decomposed by the wavelet analysis. The graphs which represents the distribution of signals' energy for each coefficients (scalograms) were obtained (see Fig. 4.6, center and right images) that present the other method of computing frequency ranges.

Diffusion of the frequencies in signal of type II, means that the less energy is transported by the signals compare to the signals scattered from regular, periodic structure of the medium 1.

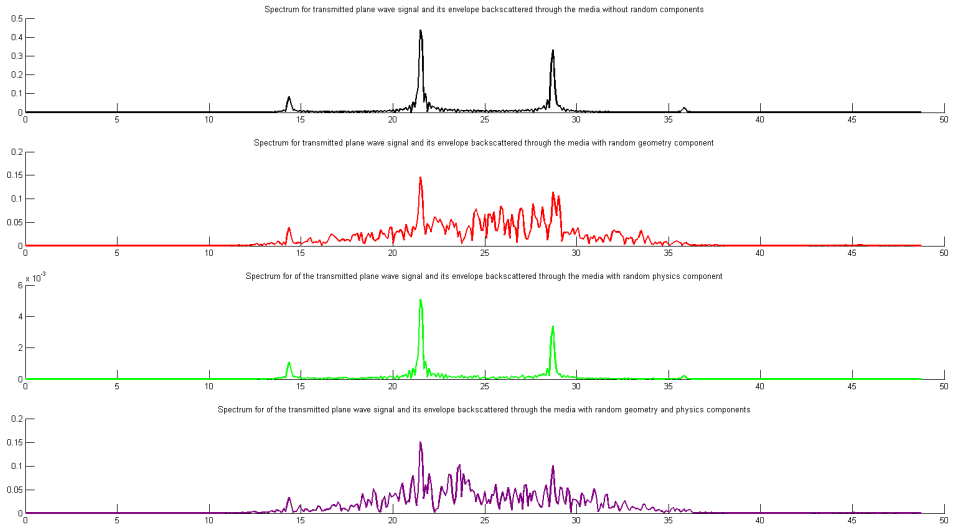

Figure 4.5: One-sided spectrum of the signals and the part one-sided spectrum of their 5th level of wavelet approximation

The geometry component makes a small impact on the backscattered signal, that is why the results of spectral analysis on fig. 4.4 and 4.5 did not show visible difference. But the scalogram, being the graph of the wavelet coefficients distribution indicates that on the very right image (corresponding to the backscattered signal through the type 3 media) there exists the violation of the periodic structure of the distribution as it is seen in the left image. It is evident that the periodic structure of the scatterers of the medium without random geometry component is preserved in all levels of the wavelet coefficient distribution.

Fig. 4.6 represents the signals' Hilbert envelopes and $a5$ coefficient (left), signals and coefficients distribution (center) and coefficients distribution in more detailed mode (right). It also may be noticed that

- Type III signal has more irregular structure in comparison with type I signal, so the geometric random components have an influence on the periodicity of backscattered signal.

- Type II signal has more irregular structure in comparison with type I and type III signals. Here it may be concluded that random components

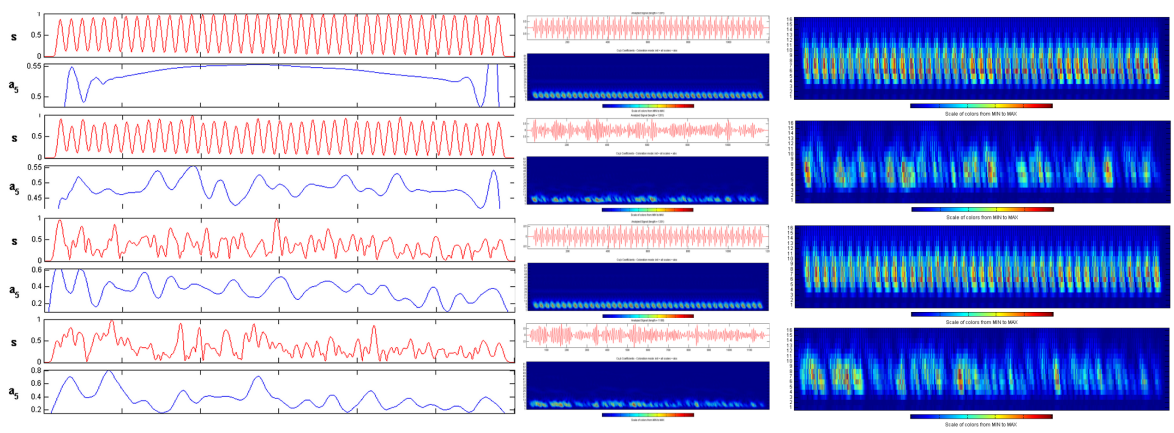

Figure 4.6: Signals' envelopes and $a5$ coefficient, signals and coefficients distribution and coefficients distribution

of physics characteristics have greater influence on the periodicity of backscattered signal.

- These differences started to be visible from the level 5th of wavelet approximations.

4.2.2 Statistical Analysis of Simulated Signals' Wavelet Decomposition

For the numerical experiment there were generated 10 signals of the each of four types of plane wave signals according to the previously stated random characteristics of the media. The initial length of the signals was set to 1200 points, then they were cut to the 1000 points with cut 100 points at the beginning and at the end. There was used a pre-processing procedure which is analogous to the descried in Section 3:

- Hilbert envelopes were calculated, $\tilde{S}(x) = |S(x)+jH(x)|$, where $H(x) = \frac{1}{\pi} p.v. \int_{-\infty}^{\infty} \frac{\tilde{S}(x)}{x - x'} dx$ and normalized $S(x,t) = S_t(x) = \frac{\overline{S}_t(x)}{\max\limits_{x \in X'} \{\overline{S}_t(x)\}}$;
- approximations by Daubechies 6 wavelet functions were performed;
- mean and standard deviation were calculated for 8 approximation levels and visualized (fig. 4.7).

Fig. 4.7 shows the mean and standard deviation's dependence on the wavelet approximation level for every type of signal. In both images blue

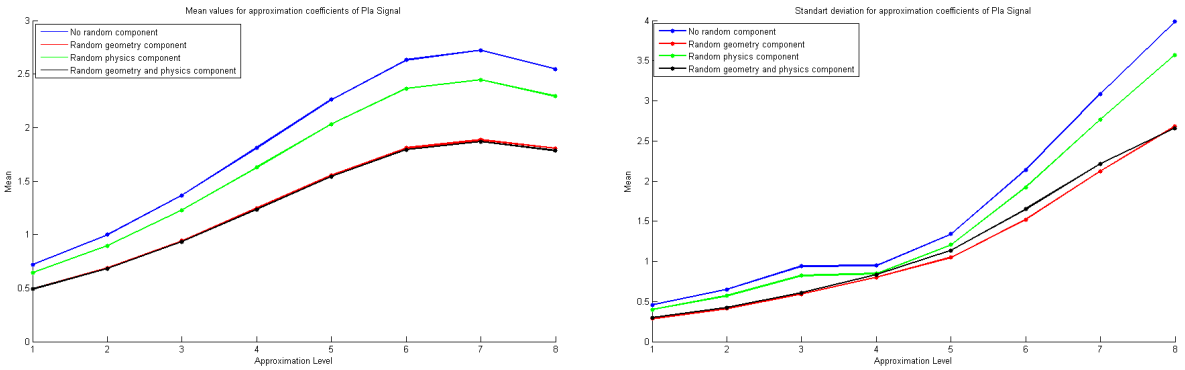

Figure 4.7: Mean and standard deviation for 8 levels of wavelet approximation

graphs correspond to the type I signal, red graphs — to the type II signal, green graphs — to the type II signal and black graphs correspond to the type IV signal. The mean graphs for signals of type II and IV almost coincide, so the physical random component has greater influence at it was noticed above. The most significant distance belongs to the 6th approximation level.

4.2.3 Scale Index for Periodicity Detecting

There considered problem was to answer the question does the obvious periodicity of obtained signal preserves if there are stochastic components in the media. To investigate the numerically generated signals there was used the absolute values of simulated plane wave signals (see fig. 4.3). The general procedure is described in section 1.4.4.

Inner part of calculating the energy (1.52) for each signal is from 300 till 900, the index values are obtained from (1.55) for each type of signal and is presented in table 4.1.

The central part of fig. 4.6 shows the coefficients distribution for 8 levels by wavelet decomposition for each type of signal, the plot on atop shows the signal itself. As it been described above and proved in [8] values of coefficient, i.e. the signals' energy is equal to zero. It formulated a hypothesis of the periodic kind of every signal.

To prove this assumption the scale index introduced in subsection 1.4.4 by formula (1.55) was calculated. Table 4.1 represents the scales with maximum and minimum energy values and the obtained values of scale index.

According to the table 4.1 the value of scale index for pure periodic signal (type I, having no random components) is equal to $2.5121 \cdot 10^{-6}$ and may be treated as zero. The signal of type III having only random physics component has the smaller value of the scale index, than signals of type II and IV. This

Signal Type	a_{max}	a_{min}	**index value**
I	7	56	$2.5121 \cdot 10^{-6}$
II	6	64	0.0035
III	7	58	$7.3322 \cdot 10^{-4}$
IV	7	61	0.0045

Table 4.1: Scale index value for each type of signal with random characteristics

signal is the most close to the periodic one, so the random physics has not very strong influence on the structure periodicity as we reported above by other quantitative parameters, like mean and standard deviation of wavelet energy on all calculated levels. But it should be noticed that even it is not strong influence the scale index value was changed of two orders of magnitude. This means that this index is very fine tool to detect even weak random noise in periodic signal. Signals of type II and IV have larger value of scale index and besides, this index is ordering the degree of the randomness. Namely, the index value is greater for signal IV where randomness is a sum of both random physics and random geometry factors.

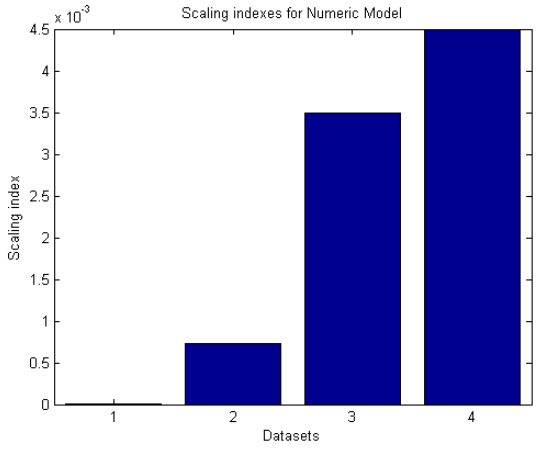

Figure 4.8: Bar diagrams for index value distribution for each type of signal with random characteristics

Fig. 4.8 visualizes the values of scale index in the bar diagram. Here the signals are ordered with the growth of values of scale index. The horizontal axed denotes the signal types as follows: the first bar correspond to the type I signal having the least value of scale index that is near 0 and is invisible on the image scale; the second bar corresponds to the type III signal having random physics component that enlarge index value but not significantly,

because its value is still very near 0. The third bar corresponds to type II signal scattered from the medium with random geometry. And the last, fourth bar corresponds to the most "unperiodic" signal in this set, containing information of scatterer structure with random geometry and random physics together and as we can expect it has the largest value of scale index.

But it should be noticed that the absolute numerical value of the scale index classifies theoretically all signals as periodic, since the values are more close to 0 than to 1. This is consistent with the made by us assumptions during generation of the random media that the medium is weak stochastically periodic, cf. Appendix B. Namely, we assumed, that the locations, sizes and physical properties of the scattering objects differ weakly from their average values. For us, however, it is important that the scale index orders the degree of signal blurring by randomness, taking a role of a quantitative parameter that is suited to measuring chaoticity of the scattering structure.

Summing up the scale index is a quantitative parameter of structure periodicity and randomness degree and is very fine tool which can be used to discover qualitative differences in the random structure.

The concept of the physically and geometrically random medium is not a new one. It was already used in the mathematical theory of composites (e.g. [46]) in the context of effective properties of two-phase composite.

Signal Type	Energy Std	Total energy
I	0.3382	502.5
II	2.4588	320.8
III	0.8388	493.1
IV	2.5375	317.6

Table 4.2: Energy interval distribution for each type of signal with random components

There was also examined energy distribution of the Daubechies 6 coefficients up to the 8th level divided by 41 intervals according to the number of scatterer along the wave propagation axis. Fig. 4.9 represents the distribution of energy for each type of signal and table 4.2 gives the values of total energy and its standard deviation, fig 4.10 shows the boxplots, the horizontal axes denotes the signal's type: 1 — type I, 2 — type II, 3 — type III, 4— type IV. Here it may be concluded that signals having more strong random components, namely, type II and type IV, have the lager value i.e. the larger energy dispersion.

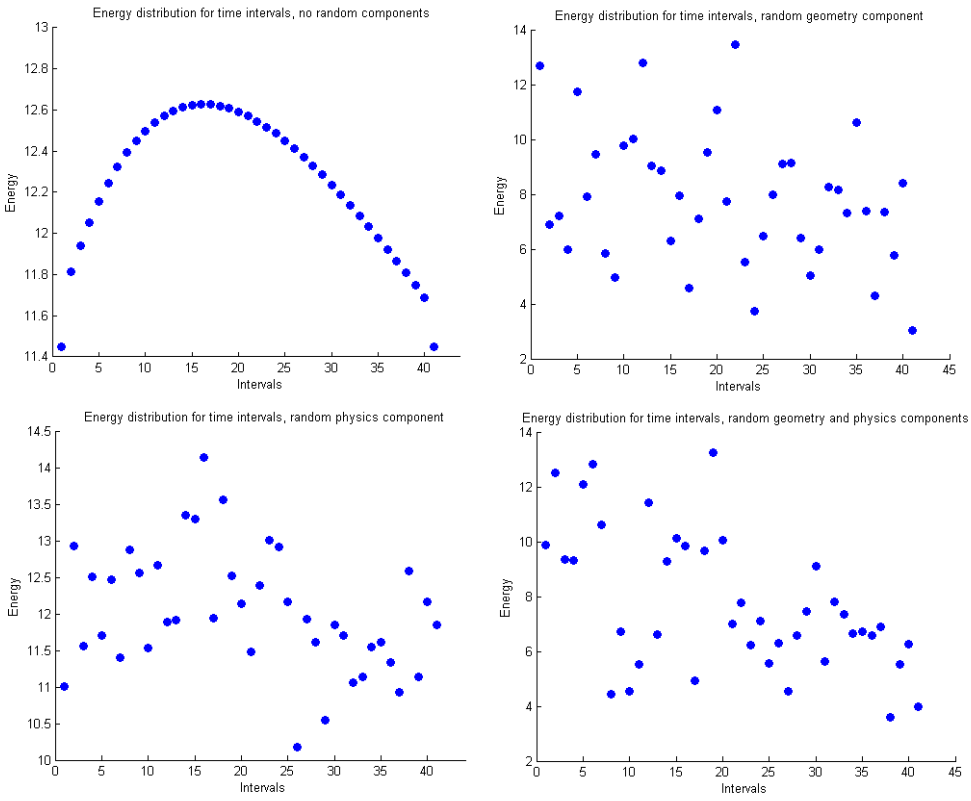

Figure 4.9: Energy interval distribution for each type of signal with random components

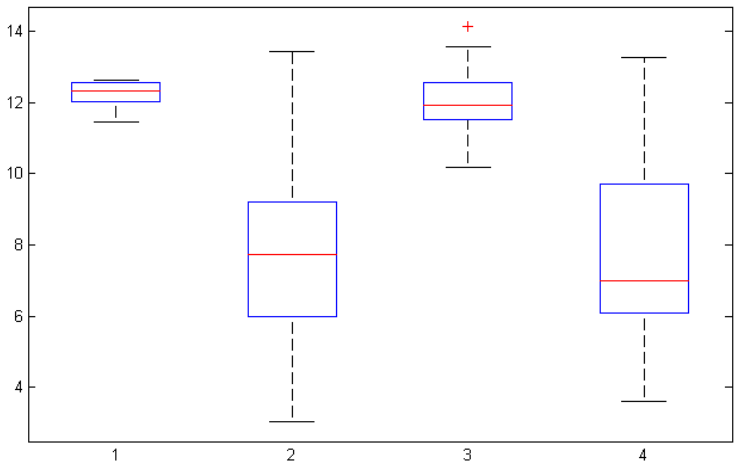

Figure 4.10: Boxplots for energy intervals for each type of signal with random components

4.3 Results

1. Mean and standard deviation for 4th level of Daubechies 6 decomposition of Hilbert envelope allow to separate the backscattered signals for media with different random distribution of scatterers.

2. The scale index shows the strictly periodic structure for media with regular distribution of scatterers. The larger value of scale index corresponds to the media with random distribution of scatterers. It also allows to order the randomness type.

3. The larger energy dispersion indicates to the media with more strong random components.

5 Threads Phantoms Study

As it have been already mentioned, the soft tissue structure possess the multi-scale anatomical inhomogeneities. There are many types of tissues, where one can recognize at least two main scales: millimeter scale and micrometer scale which are the basic scattering structures for an ultrasound wave of the diagnostic frequency range penetrating the tissue. The millimeter scale is due to the existence of quasi-periodic blocks of cells forming semi-regular lobules e.g.in the anatomical units of the liver tissue, and the micrometer scale is formed with many small scatterers like cell walls or large cell nuclei. The breaking of anatomical structure is often caused by the beginning of the cancer process. It is very important and unresolved problem to find any tools to recognize this two type of scattering. Quantitative ultrasound (QUS) provides quantitative data in an attempt to overcome the high subjectivity of ultrasonography. Scatterers spacings (SS) are one of the parameters investigated. The wavelet transform techniques has been considered as the most proper way to search of signal singularities. In [45] it was discussed how to evaluate the effect of signal noise level and scatterers positions variability (jitter) on periodicity characterization using continuous wavelet transform (CWT). US signals were simulated with mean scatterer spacing (MSS) values of 1.0, 0.99, 0.9, 0.8, 0.7, and 0.6 mm as well as with several jitters. Also, in this paper ([45]), there is a comprehensive discussion of other spectral methods applied to modelling the regularity or pseudo-regularity of real tissue structure. Usefulness of wavelet transformation to assessment of scattering medium characterization by RF backscattered signal analysis was presented in [19] and [25]. But in these papers the diffusive scattering distribution was studied alone without additional signals coming back from periodic scatterers.

To confirm the utility of the wavelet method for structural regularity recognition in backscattered ultrasound signals it was decided that a series of experiments with phantoms with pre-defined periodic properties should be performed to clarify the meaning of all applied procedures.

5.1 Materials and Methods

Experiment 1. As the first phantom there was taken the three-dimensional thread structure in the form of 6×7 lattice made from nylon threads of a thickness 0.1 mm (see Fig. 5.1, left image). The threads were placed at regular periodic structure with distances of 1 mm and the phantom had been immersed in the water.

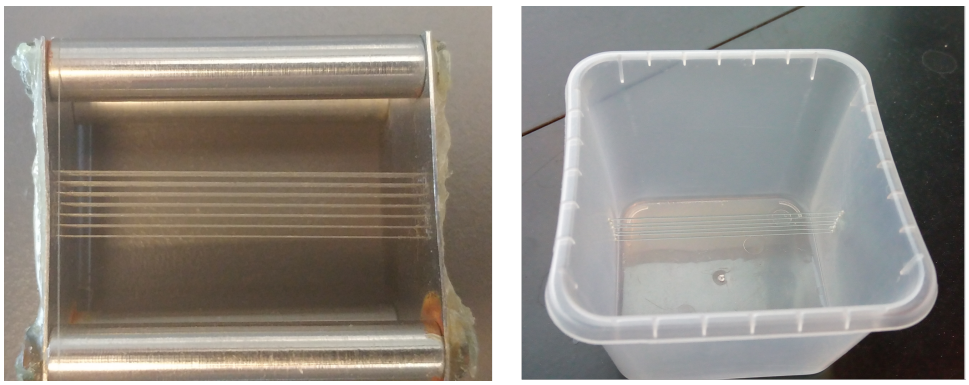

Figure 5.1: Constructed phantoms for experiments

Experiment 2. The second phantom had a linear structure with nylon threads of 0.35 mm thickness, which were located in distances of 1.5 mm. The phantom was immersed in water as in the previous phantom, but additionally oil and starch gel were used to study the influence of the background medium properties on the ultrasound backscattering signals from the same structure.

This structure was used as a model to analyze the properties of ultrasound signal echoes registered with the use of different transducers, focusing and plane ones:

1. The measurements were made with 20-MHz SonixTouch-Research ultrasound scanner (Analogic Corporation, Peabody, MA, USA) with a 20-MHz linear probe. The example of this scanner is shown in Fig. 5.2.

   The measurements were made at central frequencies 6.6, 10 and 13.3 MHz and the depth 20 mm. The initial dataset was composed of 510 lines and 1040 point, later it has been cut according to the region of phantom's location.

   Examples of B-modes of the phantoms are presented in the Fig. 5.3. On the left there is a B-mode of the phantom of lattice form, on the right — the phantom with linear structure.

2. Measurements of a transmitted single ultrasound pulse by the transmitter, Panametrics Computer Controlled Pulser/Receiver Model 5900PR, were performed on 5 mm and 10 mm depths from the transducer face with the use of a high quality hydrophone. The range of carried frequencies for used transducers were of 1 MHz to 20 MHz. The following characteristics were obtained:

   (a) The measured carried frequency is 16.6 MHz at both depths can be considered approximately equal to 17 MHz.

Figure 5.2: SonixTouch-Research ultrasound scanner

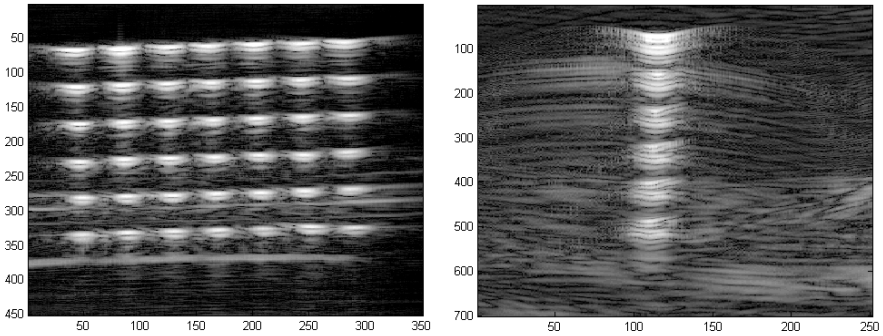

Figure 5.3: B-modes of RF signals from constructed phantoms

(b) The frequency band, calculated for 6 dB of energy averaged from two depths, is approximately 11–20 MHz.

(c) The wavelength for the carried frequency is c/a 0.01 mm and is determined from the duration of 1 period equal to 60 ns and speed of sound in the water is equal to 1500 m/sec.

(d) The pulse length is estimated as $5 \times 0.01 = 0.05$ mm.

The summary of the experiment's characteristics are given in table 5.1.

Characteristics	Value
Main frequency, MHz	15
Wavelength, mm	0.01
Sampling distance, mm	0.02
Depth, mm	260

Table 5.1: Characteristics of the experiment

Having measured the pulse properties and applied the wavelet analysis to the registered signals the identification of the threads positions in space, namely MSS (Mean Scatterer Spacing) could be calculated. The example of the B-mode of this structure in the water in shown in the Fig. 5.3, to the left.

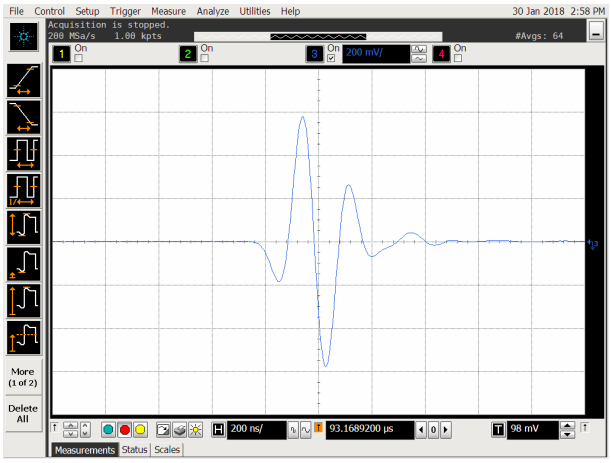

Figure 5.4: Example of the initial impulse

Distance between reflector and transducer was equal to c/a 7 cm. The precise distance can be calculated from the images of pulses registered by the oscilloscope (Digital Storage Oscilloscope DS09104A Agilent Technologies), Fig. 5.4.

5.2 Periodicity Detecting

5.2.1 Scale Index Determination

Following the idea of establishing a marker to identify the degree of signals periodicity for both experiments and each transducer type there were calculated a scale indexes (1.55). Also the random component had been added into backscattering media by replacing in the second experiment the water

by more noisy media, namely, oil and starch gel. From the whole dataset obtained from the scanners there had been chosen data corresponding to the area where threads had been located (it is noted as region of interest, ROI). And the analyzed signal was treated as a mean for all signals from ROI.

Table 5.2 represents the values of scale index and the values for a_{max} and a_{min} used in formula (1.55) corresponding to different transducers. These values are of the same order. They are not strictly equal to 0, but very small. So it may be concluded that the obtained backscattered signals are close to periodic.

Transducer	a_{max}	a_{min}	**index value**
Linear	4	32	0.0224
6F	85	256	0.0499
3.5F	58	228	0.0689
6P	22	224	0.0446

Table 5.2: Scale index for RF signal from the thread phantom measured by different transducers

Table 5.2 represents the values of scale index according to the media of phantom. The data was taken as a mean values from all data of chosen region of interest. Additionally there was obtained the value for the pure starch gel media without phantom inside it with assumption that it is the most far from periodic-structured medium.

Media type	**Index value**
Water	0.0312
Oil	0.0635
Starch gel	0.0855
Pure starch gel	0.3153

Table 5.3: Scale index for the RF signal from thread phantom measured with different medium

Table 5.3 shows that the scale index value increases with each new surroundings. It is also visualized in the bar diagrams (Fig. 5.5).

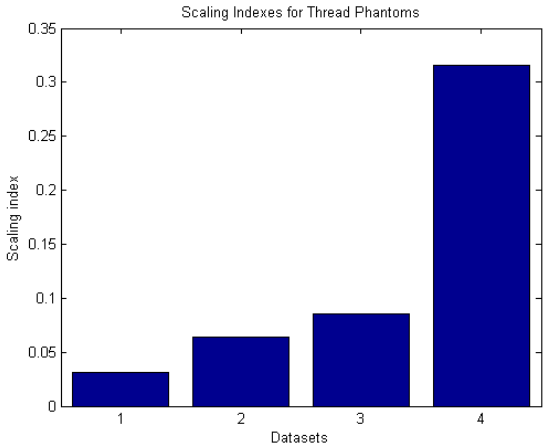

Figure 5.5: Bar diagram for index values for the thread phantom

5.2.2 Mean Scatterer Spacing Estimation

Experiment 1. The whole dataset has 510 lines and 1352 sampling points. To reduce the additional effects this dataset was cut to the 350 lines and 450 sampling points. From equality (1.57) the parameter $J = 1$, so we consider the 1st wavelet approximation level as the best one. In Fig. 5.6 it is placed the initial dataset and its first level approximation with Daubechies 6 wavelets.

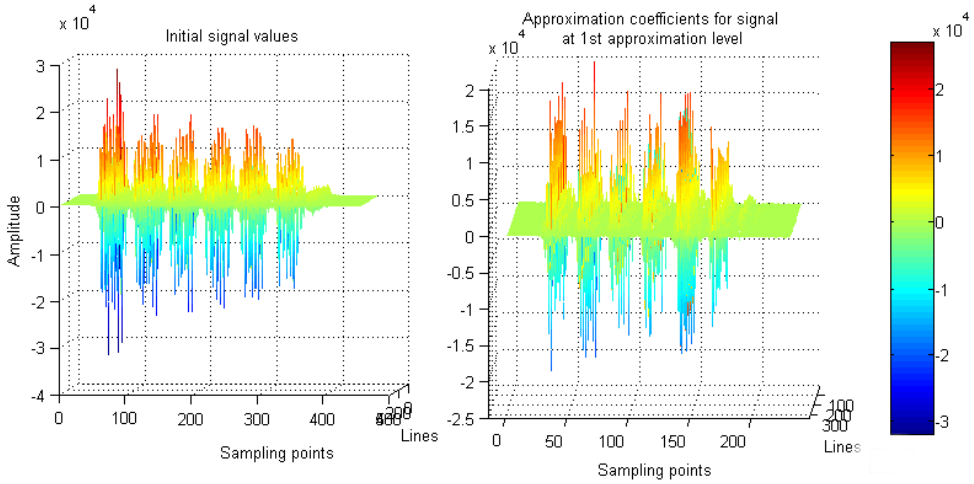

Figure 5.6: Initial data and 1st level wavelet approximation for RF signal from thread phantom

The coefficients distribution of Daubechies 6 wavelet for one chosen line, namely 320, are shown in the Fig. 5.7. The red graph on the top indicated the initial signal and the colored graph shows the distribution of wavelet

coefficients.The horizontal axed corresponds to the time axis (or the wavelet shift coefficient b), the vertical axis corresponds to the wavelet scale coefficient a and the energy value for each coefficient b and a is indicated by color, from blue to red.

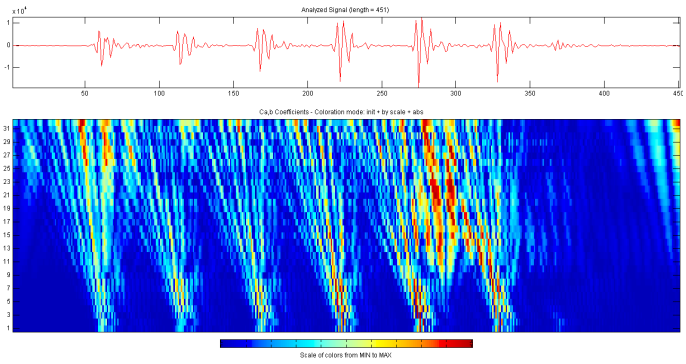

Figure 5.7: Wavelet coefficient distribution for one line of a RF signal from periodic structure

The concept of Mean Scaterrer Spacing (MSS) was introduced in subsection 1.4.5. For initial experimental data it was calculated from equation (1.56) the mean values for all lines $MSS_r = 0.9$ mm, from the experiment it follows that $MSS_e = 1.1$mm. Thus the error e would be equal to 22% (from equality (1.59)).

To calculate the MSS for the approximation level the was preformed the discrete wavelet transform with Daubechies 6 wavelet and then there were taken the mean values for all lines. The obtained dataset was divided onto 6 parts of 55 points, which will be bisected for each level and using the following equation

$$MSS = \frac{1}{6} \cdot h \cdot 2^n \sum_{i=1}^{6} \text{dist}_i, \tag{5.1}$$

where dist_i are the distance between the positions of neighboring points with maximal absolute value, h is sampling distance, n is the level of wavelet approximation. There were computed MSS values as distance between coordinates of maximal absolute values equal to $MSS = 1.08$, $e = 1.82\%$ for initial signal data. For the 1st wavelet approximation level these parameters were obtained also: $MSS = 1.096$ and $e = 0.36\%$. As it may be noticed the error decreases after wavelet filtering.

Experiment 2. The scalogram structure supposed that it would be possible to separate each scatterer (thread of the phantom). In the initial

(0-level) to each thread correspond 480 initial points as the MSS of phantom is equal to 1.85 mm that is 2.4 msec of wave travelling.

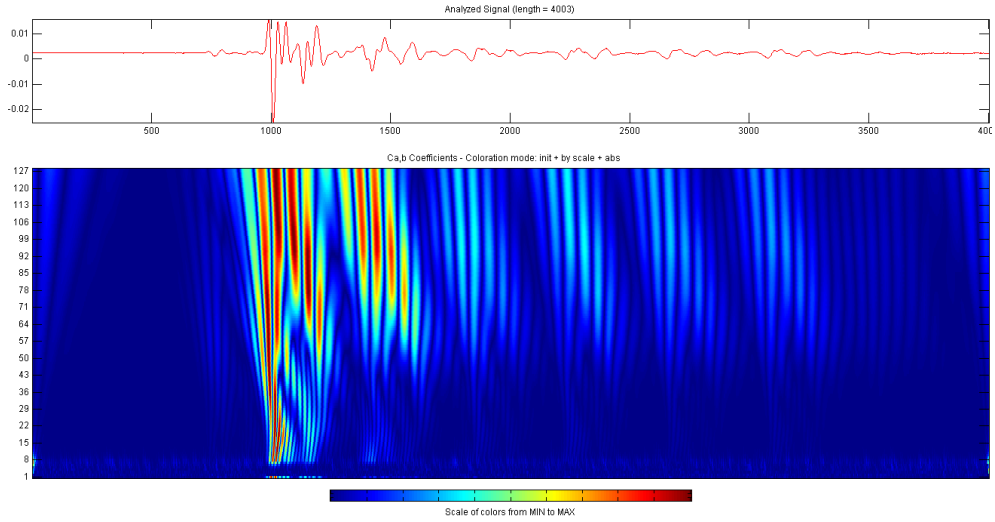

Figure 5.8: Wavelet coefficient distribution for RF signal from phantom with periodic structure and impulse frequency 6MHz

Using the sampling frequency and the central frequency of Daubechies 6 wavelets $f_0 = 0.7273$ it is possible to recalculate the scale coefficients and sampling distance and to juxtapose the real frequencies (table 5.4).

Level	2^N	Frequency, MHz	Sampling, ns
1	2	72.73	13.75
2	4	36.36	27.5
3	8	18.18	55
4	16	9.09	110
5	32	4.5	220
6	64	2.27	440
7	128	1.14	880
8	256	0.57	1760
9	512	0.28	3520

Table 5.4: Frequencies and sampling distance for wavelet approximation of RF signal from phantom with periodic structure

According to the equality (1.57) the best level $J = 5$ that lays in the third approximation level. So we chose $j = 3$ for the MSS calculations. There was also used equality (5.1) with $h = 3.9$ μm. In Fig. 5.9 there is presented the

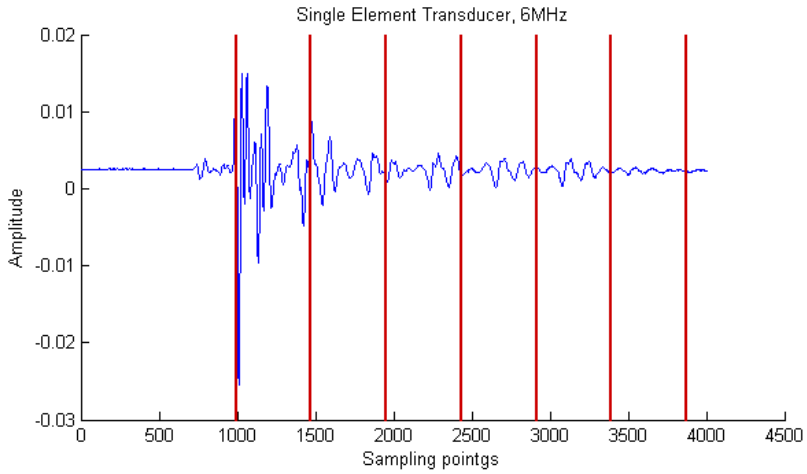

Figure 5.9: Dividing into intervals RF signal from phantom with periodic structure

Transducer name	MSS for initial data	Error for initial data	MSS for chosen level	Error for chosen level
6F	1.99	7%	1.81	1.85%
3.5F	1.94	4.9%	1.77	4.2%
6P	2.1	12.7%	1.98	7.2%
1P	1.82	1.6%	1.64	12%

Table 5.5: MSS and error for RF signal from phantom with periodic structure, different transducers

Media Type	MSS for initial data	Error for initial data	MSS for chosen level	Error for chosen level
Water	1.88	0.14%	1.848	0.11%
Oil	2.1	13.4%	1.89	1.9%
Starch gel	1.89	2.4%	1.8480	0.11 %

Table 5.6: MSS and error for RF signal from phantom with periodic structure, different media

signal obtained with transducer 6F and the intervals of 480 points for each scatterer.

The obtained values for MSS and its error for signals and their approximation of 3rd level with Daubechies 6 wavelet functions are placed in the tables 5.5 and 5.6. It follows that the wavelet approximation of the initial data improves the MSS error.

5.3 Results

- The scale index value was increasing with increasing of environment noise. The scales of the noises (oil structures and starch particles) although very different, for oil the scale of inhomogeneities was less than micrometers and for starch-gel the scale was at least one order greater, both had a diffusive random character. The value of the scale index was sensitive to the environment scatterers size, and the value of index ordered the size of environmental scatterers size.

- The application of wavelet approximation reduces the error of Mean Scatterer Spacing (MSS) value.

6 Liver Structure Investigation in Vivo

The World Health Organization announced that With more than 782,000 new cases diagnosed in 2012, liver cancer is the sixth most common one. It accounts for 6% of all cancers worldwide. Cancer is the second leading cause of death globally and is estimated to account for 9.6 million death in 2018.

As we previously repeatedly underlined the emitted ultrasound beams interact with scatterers in the tissue, so particularly, backscattered signals from liver tissue in vivo should information about weak diffuse subresolution scatterers in tissue cells and also about stronger pseudo-periodic lobules formed from ordered cell groups.

The preferred imaging method for screening is ultrasonography (USG) which is well tolerated and widely available. However, the sensitivity of USG for the most popular primary cancer is low because small nodules can be missed in a cirrhotic liver. Any kind of additional parametric diagnostics-enhanced classical USG improves the diagnostic performance of USG for liver cancer. A large number of methods for the diagnosis of liver tumors is descried and discussed in a review paper [73].

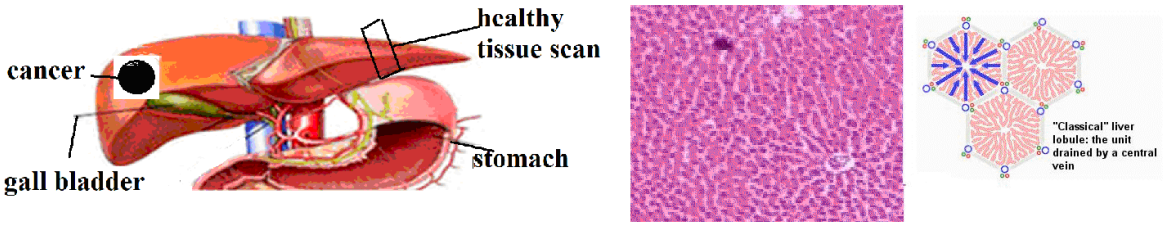

Figure 6.1: Example of liver and lobules

Images for Fig. 6.1 are taken from the open network sources and demonstrate the human liver (left image) and the liver lobule structure (right image).

In [22] the lobule structure is described as roughly hexagonal and the liver can be considered as composite of periodically distributed lobules, in which the plane normal to the central vein direction can be considered as the isotropic plane only at sufficiently long wavelengths (low frequencies) of acoustic excitation. But the ultrasound excitation having wavelength of less than millimeter can "see" the lobules as the periodic scatterers.

Fig. 6.2 ([22]) shows the scheme of liver (left image) and the lobule hexagonal structure (right image), where CV here denotes the central vine.

Our hypothesis is that the histological periodicity of liver tissue is preserved in the periodicity of the backscattered signal. The structure changes

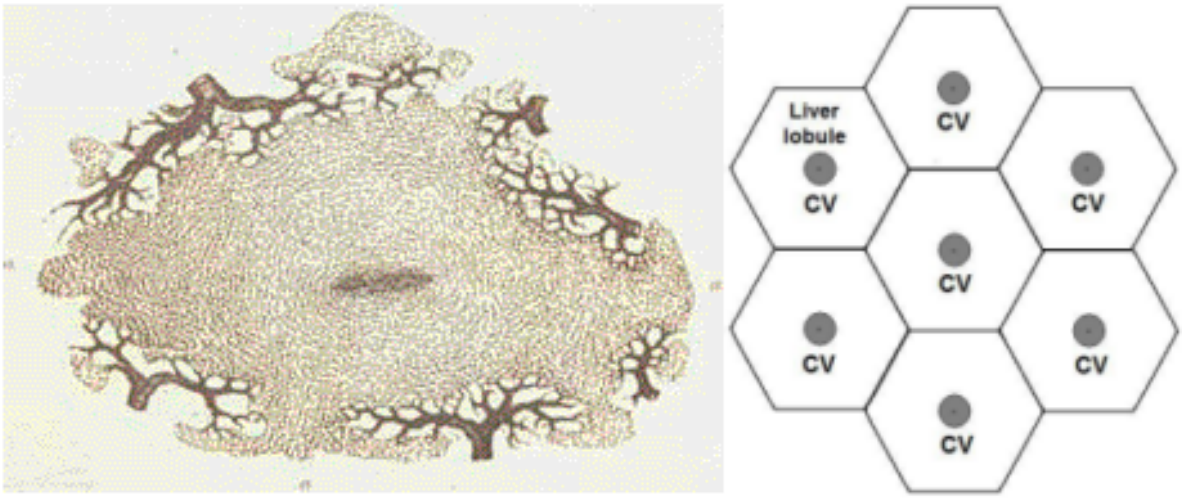

Figure 6.2: Liver lobule geometry [22]

caused be liver diseases, e.g. cancer, should break the periodicity of backscattered signal.

6.1 Experiment Description

B-mode images (scans) and RF (Radio Frequency) signals have been recorded from a patient with primary liver tumor, located in the left lobe of the liver. The tumor was imaged in two perpendicular planes. Data were recorded from cancerous tissue, and from healthy liver parenchyma in both the left and right lobes.

The examination was carried out by a physician (radiologist) in the Central Hospital Clinical Banach using Ultrasonix Sonix Touch-Research, Medical Corporation, Richmond, BC, Canada and convex C5-2/60 linear transducer at a central frequency of 3.3 MHz. The example of such USG apparatus is presented in the Fig. 5.2. The region of tumour had been also outlined by physician, they e.g. have the size $46 \times 42 \times 51$mm (fig. 5.2, left image, the cancerous part is situates on the tpo of the B-mode).

The RF data were collected with sampling rate of 40 MHz and digitized with 16-bit resolution. The width of each scan corresponded to 512 lines, the depth of 16 cm, the focus location was situated in the middle of scan c/a and equal to 8 cm. Each lines contained 5200 sampling points with sampling distance $h = 0.038$ mm, so 1 mm contained 26 points.

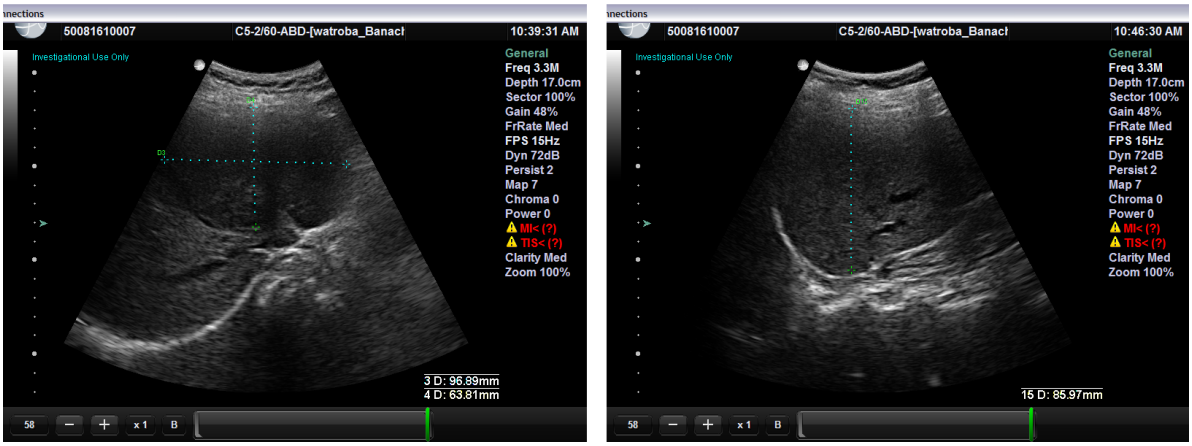

Figure 6.3: B-modes of liver experiment, samples of area with tumor and healthy

6.2 Choosing Regions of Interest

Besides the information obtained from the B-mode image, used usually by physician, the collection of RF signals registered during imaging procedure contains the extra information which should be analysed and which are often filtered before image is displayed on the screen. We constructed our own B-mode image using raw RF signals without any preprocessing and than this B-mode image was the base for physician to mark the region of the lesion in liver. To determine areas there were used cut rectangular parts of the image called regions of interest (ROI). This is the common technique in such kind of study (see, e.g. [57], [58]).

The chosen region on interest in there the rectangular areas 500×50 sampling points (19.2×1.92 mm) taken from the same depth for each RF signal, which is equal to 48.1 mm.

Examples of these regions is shown in figure 6.4, they are marked with colored rectangles; examples of B-mode for fixed ROI is presented in Fig. 6.5. The left image indicates the part with tumor and right — the environment part healthy tissue.

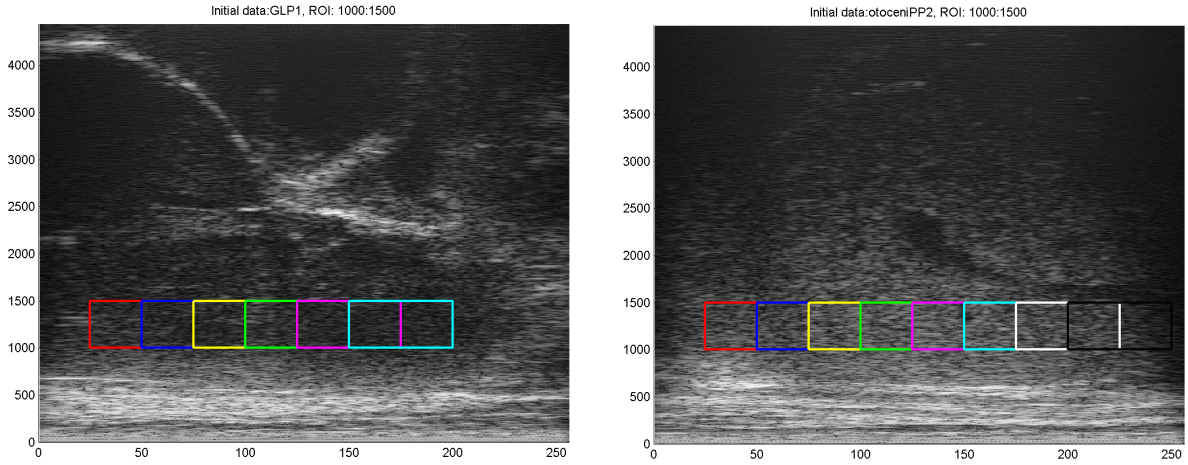

Figure 6.4: Example of B-mode with chosen ROI, samples of area with tumor and healthy

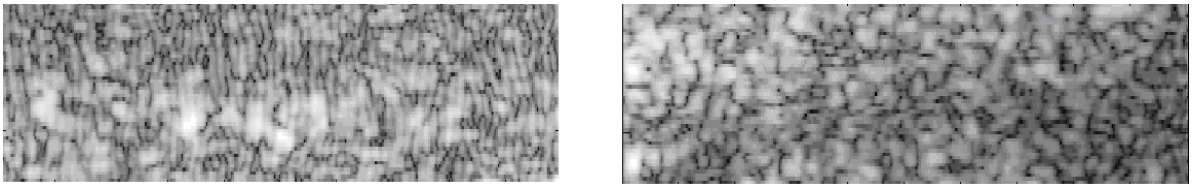

Figure 6.5: Example ROI area, samples of area with tumor and healthy

6.3 Scale Index Determination

As lobule structure of the liver are supposed to have periodical structure, the backscattered echo signal should also preserve this property.

Using formula (1.55) there were obtained the values of scale index for every dataset for chosen ROI and than the mean values had been calculated. Inner part of calculating the energy 1.52 for each signal is from 200 till 800, the index values are obtained from (1.55), section 1.4.4 for each type of signal.

Left image of the Fig. 6.6 represents the distribution of index values, red line here corresponds to the data from tumorous areas and the blue line displays the scale indexes for environment area.

Table 6.1 shows the values for the first order statistics for both datasets and in fig. 6.6 there are boxplots of scale index value for each dataset.

From table 6.1 and Fig. 6.1 and 6.7 it may be concluded that for the areas with more periodic structure of scatterers, i.e. for the healthy environment areas the value of scale index is less than for the areas where this periodicity are broken by cancerous changes. Fig. 6.7 shows the values of scale index

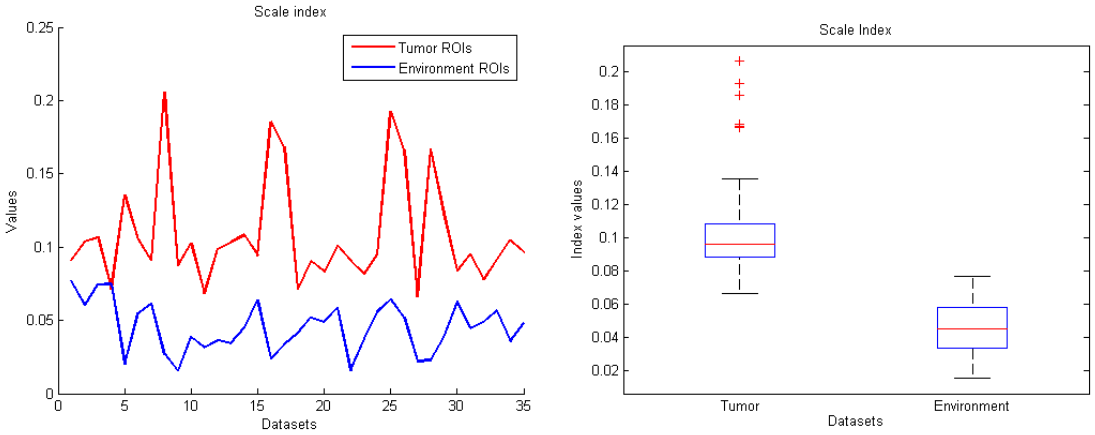

Figure 6.6: Mean values for tumor and environment areas and boxplots for scale index values distribution

	Tumor ROIs	Environment ROIs
Min	0.0665	0.0157
Max	0.2061	0.0768
Mean	0.1087	0.0451
StD	0.0367	0.0171

Table 6.1: Values of scale index for tumorous and healthy liver areas

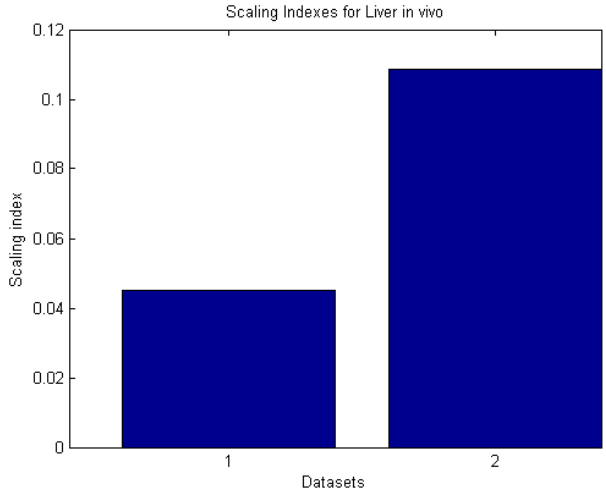

Figure 6.7: Bar diagram for scale index values distribution.

in the form of bar diagram. The first bar corresponds to data taken from the healthy regions and it has the value that is less then the second bar that corresponds to the areas of liver with tumor.

6.4 Mean Scatterer Spacing Estimation

The mean scatterer spacing (MSS) can be used for effective evaluation of microstructural changes of those biological tissues with semi-regular distribution characteristics, such as the liver, which is divided histologically into lobules. The lobules are the main scatterers for ultrasonic scattering, and pathological changes of the liver can be reflected by the changes of the MSS. Therefore, the MSS may be used as the parameter to characterize the liver tissue having some kind of diseases that cause the infraction of its initial periodicity [37], [45].

The inter scatter spacing of the liver supposed equal to 1 mm [74], that is why the intervals for calculating MSS were supposed to be equal to 1 mm too. Each interval contained 26 points. For each wavelet decomposition level this interval decreased by half. According to formula (1.57), section 1.4.5 the optimal level for mean scatterer spacing for liver sample is $J = 2$. The MSS was computed for each ROI from the data set and then there was calculated mean value.

The obtained result quantities for mean scatterer spacing are given in table 6.2 and their boxplots are shown in Fig 6.8.

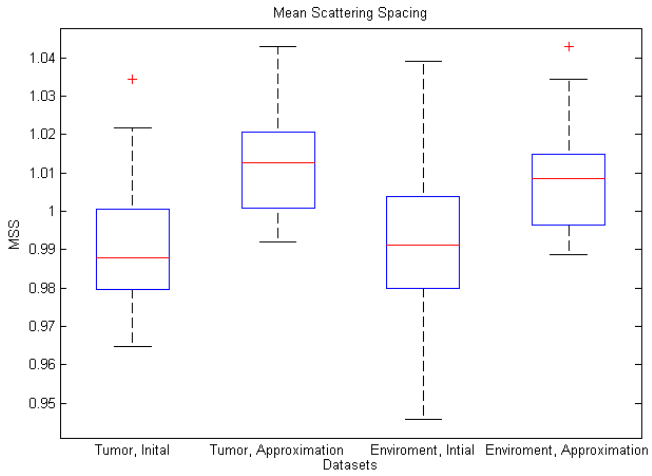

Figure 6.8: Boxplots for MSS for human liver tissue

Here it is obvious that the greatest value of MSS belongs to the dataset corresponding to the tumour areas, i.e. to the tissue samples with the less periodic structure and the error for the second approximation level is less than for initial data.

The evaluation of the obtained results was made by comparing them with the test made on measurements of pork liver tissue sample ex vivo. The data

	MSS for initial data	Error for initial data	MSS for chosen level	Error for chosen level
Tumor ROIs	0.9919	1.5%	1.01302	1.4%
Environment ROIs	0.9912	1.8%	1.009	1.14%

Table 6.2: MSS and error for human liver tissue

were collected by the ultrasound scanner SonixTouch-Research with linear head. The optimal level for the wavelet decomposition was given by formula (1.57), section 1.4.5, $J = 1$. The obtained results are presented in table 6.3 and they confirmed the previous statements.

Initial data	MSS	0.9718
	Error	2.8%
Chosen level	MSS	0.9918
	Error	0.82%

Table 6.3: MSS and error for pork liver tissue ex vivo experiment

6.5 Results

- The scale index quantifies the structure of liver as more periodic in healthy areas than in tumor areas.
- Wavelet approximation clearly reduces the error of mean scatterer spacing (MSS) value for liver tissue experiments ex vivo and in vivo.

7 Conclusions

The thesis presents several issues in which the using of the wavelet transform of the ultrasonic echo signals allowed to determine new, quantitative parameters — in relation to the existing methods – characterizing tissue scattering structures.

- It was shown that from the wavelet distribution of the RF signal envelope, it is possible to determine the diffusive scatterers number markers. It turned out that selected levels of wavelet approximation of signals envelopes show quantitative differences in statistical parameters of distributions such as Gamma, Nakagami and K-distribution. Nonparametric statistics of selected level of wavelet approximation of ultrasound echoes measured the differences between the spatial distribution of scatterers.

- The method of tracking temperature changes by K-distribution shape parameter values of a wavelet level decomposition statistics was proposed. This method significantly reduces the amount of processed data in comparison with use of raw RF echo for this purpose.

- It was shown that the values of the MSS quantitative parameter (mean scatterers spacing), often used in tissue characterization, determined on the basis of the selected level of wavelet approximation of echo signals, improved the parameter estimation accuracy.

- A measure of structure chaoticity (or a measure of distance from periodicity) called "scale index" defined on the base of signal wavelet transform properties was here for the first time used in the processing of the ultrasonic RF signals. As a result, using the scale index it was possible to arrange the scattering structures from a strictly periodic to completely chaotic structure. This indicator was used to distinguish in vivo areas of healthy liver tissue from the tumour areas.

- The usefulness of the MSS parameter and the scale index for the classification of scattering structures was verified twice, analyzing echoes collected from specially constructed phantoms and analysis of numerically generated signals, describing the scattering by various types of random structures.

Below it is given a list of publications concerning the PhD thesis. The full list of author's papers is given in appendix C.

Papers in Scientific Journals

1. B. Gambin, **O. Doubrovina**, Statistical properties of wavelet transform coefficients of backscattering signal from soft tissues and their phantoms *Hydroacoustics*, **16**, Gdansk, 59–66 (2013).

2. **O. Doubrovina**, B. Gambin, E. Kruglenko, Temperature level and properties of wavelet approximations of backscattered ultrasound. *Hydroacoustics*, **17**, 37–46 (2014).

3. **O. Doubrovina**, B. Gambin, J. Wòjcik, Detection of variations in random characteristics of scattering medium by the wavelet analysis, 10th EAA International Symposium on Hydroacoustics, May 17–20, 2016, Jastrzebia Gora, Poland. *Archives of Acoustic* **41**, No 2, p. 360 (2016).

4. B. Gambin, J. Wòjcik, **O. Doubrovina**, Differentiation of random structure properties using wavelet analysis of backscattered ultrasound. *Hydroacoustics*, **19**, 121–128 (2016).

5. B. Gambin, M. Byra, E. Kruglenko, A. Nowicki, *O. Doubrovina*, Ultrasonic measurement of temperature rise in breast cyst and in surroundings regions *Archives of Acoustic* **41**(4), 791-798 (2016).

Chapters of Books

1. B. Gambin, **O. Doubrovina**, Wavelet analysis for temperature increase detection from acoustic backscattered signal. In: Complex Analysis and Potential Theory with Applications (T. Aliev Azerogly, A. Golberg, S.V. Rogosin Eds.). Cambridge Scientific Publishers, 63–76 (2014).

2. **O. Doubrovina**, R. Tymkiewicz, H. Piotrzkowska-Wròblewska, B. Gambin Linking of structural parameters to properties of ultrasound backscattered signals by the threads phantoms study, Aktualnoci Inynierii Akustycznej i Biomedycznej, Polskie Towarzystwo Akustyczne, Oddzia w Krakowie, Red. K. Suder-Dębska, Krakw, 67–79 (2018).

Conference Proceedings

1. **O. Doubrovina**, J. Litniewski, B. Gambin Wavelet approximation and statistical approach to random fluctuations of amplitude in backscattered ultrasonic signal. *Forum Acousticum*, Sept. 7–12, 2014, Krakow, 2014, 205–206 (2014).

2. B. Gambin, M. Byra, **O. Doubrovina** Nonparametric statistics in indirect temperature estimation by ultrasound imaging. *Abstracts of reports of the 8th international scientific seminar, 14-19 September 2015, Minsk, Belarus*, p. 25 (2015).

3. J. Wójcik, B. Gambin, **O. Doubrovina**, Randomness characteristics of scattering medium by the wavelet analysis. *Abstracts of the 3rd International Workshop "Boundary Value Problems, Functional Equations and Applications", Rzeszow, Poland, April 20–23, 2016*, p. 64 (2016).

4. **O. Doubrovina**, B. Gambin, H. Piotrzkowska-Wrblewska, The backscattered ultrasound signal wavelet decomposition applied to recognize of regular positioning of scatterers in a sonicated medium. Materials of the 9th international scientific seminar, 17-21 September 2018, 64–65 (2018).

References

[1] U.R. Abeyratne, X. Tang, Ultrasound scatter-spacing based diagnosis of focal diseases of the liver *Biomedical Signal Processing and Control* **2**, 9–15, (2007).

[2] D.A. Abraham, A.P. Lyons, Reliable methods for estimating the K-distribution shape parameter, *IEEE Journal of Oceanic Engineering*, **35**(2), 288-302, (2010).

[3] Addison P. *The Illustrates Wavelet Transform Handbook*, IoP, Bristol-Philadelphia, (2002).

[4] C.E. Agnew, P.K. Hamilton, A.J. McCann, R.C. McGivern, G.E. McVeigh, Wavelet Entropy of Doppler Ultrasound Blood Velocity Flow Waveforms Distinguishes Nitric Oxide-Modulated States, *Ultrasound in Medicine & Biology,* **41** 1320–1327, (2015) doi.org/10.1016/j.ultrasmedbio.2014.12.013.

[5] A Practical Guide to Wavelet Analysis, *Christopher Torrence and Gilbert P. Compo Bull Am Meteorol Soc*, **79**, 61–78, (1998).

[6] R.M. Arthur, W.L. Straube, J.W. Trobaugh, E.G. Moros, Non-invasive estimation of hyperthermia temperatures with ultrasound, *Int. J. Hyperthermia*, **21**(6), 589–600, (2005).

[7] N.M. Astaf'eva, Wavelet analysis: basic theory and some applications (in Russian), *Uspekhi Fizicheskikh Nauk Russian Academy of Sciences* **39**(11), 1145–1170 (1996).

[8] R. Benítez, V.J. Bolós, M.E.Ramírez A wavelet-based tool for studying non-periodicity *Comput. Math. Appl.* **60** 634–641 (2010).

[9] M. Byra *Klasyfikacja zmian nowotworowych piersi na podstawie wasności statystycznych ech ultradźwiękowych.* Praca doctorska. IPPT, Warszawa (2017).

[10] C. Cattani, O. Doubrovina, S. Rogosin, S.L. Voskresensky, E. Zelianko On creation of a new diagnostic model for fetal well-being on the base of wavelet analysis of cardiotocograms, *J. Med. Systems* **30**, Springer, 489–494 (2006).

[11] W. Chen, S. Holm, Modified Szabo's wave models for lossy media obeying frequency power law, *J. Acoust. Soc. Am.* **114**(5), 2570–2575 (2003).

[12] W. Chen, S. Holm, Fractional Laplacian time-space models for linear and nonlinear lossy media exhibiting arbitrary frequency power-low dependency, *J. Acoust. Soc. Am.*, **115**(4), 1424–1430, (2004).

[13] F.S. Cohen, G. Georgiou, Wold-decomposition of the backscatter echo in ultrasound images of soft tissue organs, *IEEE Trans. Ultrason. Ferroelect. Freq. Contr.* **44**, 460–472, (1997).

[14] B.E. Treeby, B.T. Cox, Modeling power low absorbtion and dispertion for acoustic propagation using the fractional Laplacian, *J. Acoust. Soc. Am.* **127**(5), 2741–2748, (2010).

[15] F. Davignon, J.-F. Deprez, O. Basset, A parametric imaging approach for the segmentation of ultrasound data, *Ultrasonics*, **43**, 789–801, (2005).

[16] O.V. Doubrovina, S.V. Rogosin, On Linear and Nonlinear Equations on Finite Intervals, *Fractional Calculus and Applied Analysis*, **5**(4), 461-478, (2002).

[17] G. BalOlivier, P Ryzhik, Random Media in Inverse Problems, Theoretical Aspects, in *Encyclopedia of Applied and Computational Mathematics*, DOI: 10.1007/978-3-540-70529-1 50, (2015).

[18] B. Gambin, M. Byra, O. Doubrovina, Nonparametric statistics in indirect temperature estimation by ultrasound imaging. Abstracts of reports of the 8th international scientific seminar, 14-19 September 2015, Minsk, Belarus, p. 25, (2015).

[19] B. Gambin, O. Doubrovina, Statistical properties of wavelet transform coefficients of backscattering signal from soft tissues and their phantoms *Hydroacoustics*, **16**, Gdansk, 59–66, (2013).

[20] B. Gambin, O. Doubrovina, Wavelet analysis for temperature increase detection from acoustic backscattered signal. *Complex Analysis and Potential Theory with Applications (T. Aliev Azerogly, A. Golberg, S.V. Rogosin Eds.)*, Cambridge Scientific Publishers, 63–76, (2014).

[21] B. Gambin, E. Kruglenko, Temperature Measurement by Statistical Parameters of Ultrasound Signal Backscattered from Tissue Samples, *Acta Physica Polonica A*, ISSN: 0587-4246, DOI: 10.12693/APhysPolA.128.A-72, **128**, No. ;1-A, A-72–78, (2015).

[22] B. Gambin, E. Kruglenko, A.A. Gałka, R. Wojnar, Macroscopic thermal properties of quasi-linear cellular medium on example of the liver tissue, *Computer Assisted Methods in Engineering and Sciense*, **22**(4), 329–346, (2015).

[23] B. Gambin, T. Kujawska, E. Kruglenko, A. Mizera, A. Nowicki, Temperature fields induced by low power focused ultrasound during gene therapy. Numerical predictions and experimental results. *Archives of acoustics*, **34**(4), 445–460, (2009).

[24] B. Gambin, E.;Kruglenko, T. Kujawska, M. Michajłow, Modeling of tissue in vivo heating induced by exposure to therapeutic ultrasound, *Acta Physica Polonica A*, **119**, 950–956, (2011).

[25] B. Gambin, J. Wòjcik, O. Doubrovina, Differentiation of random structure properties using wavelet analysis of backscattered ultrasound. *Hydroacoustics*, **19**, 121–128, (2016).

[26] M.J Daniels., T. Varghese, E.L. Madsen, Zagzebski J.A. Non-invasive ultrasound-based temperature imaging for monitoring radiofrequency heating–phantom results. *Phys. Med. Biol.*, **52**, 4827–4843, (2007).

[27] I. Daubechies *Ten Lectures on Wavelets*, SIAM, Philadelphia (1993).

[28] F. Davignon, J.-F. Deprez, O. Basset, A parametric imaging approach for the segmentation of ultrasound data, *Ultrasonics*, **43**, 789-801, (2005).

[29] O. Doubrovina, B. Gambin, E. Kruglenko Temperature level and properties of wavelet approximations of backscattered ultrasound. *Hydroacoustics*, **17**, 37–46, (2014).

[30] O. Doubrovina, B. Gambin, J Wòjcik, Detection of variations in random characteristics of scattering medium by the wavelet analysis, 10th EAA International Symposium on Hydroacoustics, May 17-20, 2016, Jastrzebia Gora, Poland.*Archives of Acoustic* **41**(2), p. 360, (2016).

[31] O. Doubrovina, R. Tymkiewicz, H. Piotrzkowska-Wròblewska, B. Gambin Linking of structural parameters to properties of ultrasound backscattered signals by the threads phantoms study, Aktualnoci Inynierii Akustycznej i Biomedycznej, Polskie Towarzystwo Akustyczne, Oddzia w Krakowie, Red. K. Suder-Dębska, Krakw, 67–79, (2018).

[32] O. Doubrovina, B. Gambin, H. Piotrzkowska-Wróblewska. The backscattered ultrasound signal wavelet decomposition applied to recognize of regular positioning of scatterers in a sonicated medium. Matherials of the 9th international scientific seminar, Minsk, Belarus, 17-21 September 2018, 64–65, (2018).

[33] V. Dutt and J.F. Greenleaf, Ultrasound echo envelope analysis using a homodyned K-distribution signal model, *Ultrasonic Imaging*, **16**(4), 265–287, (1994).

[34] B.S. Everitt, T. Hothorn, *A Handbook on Statistical Analysis Using R*, CRC Press, (2010).

[35] M. Farge, J. Lewalle, K. Schneider, Wavelet transforms. Section D.6.1. *Handbook of Experimental Fluid Mechanics*, Springer, 1378–1395, (2007).

[36] L.L. Fellingham, F.G. Sommer, Ultrasonic characterization of tissue structure in the in vivo human liver and spleen. *IEEE Trans Son Ultrason.* **31**, 418–428, (1984).

[37] G. Georgiou, F.S. Cohen, Tissue Characterization Using the Continuous Wavelet Transform. Part I: Decomposition Method *IEEE Transactions on Ultrason., Ferroelect. Freq. Contr.* **48**(2) (2001), 355–363.

[38] G. Georgiou, F.S. Cohen, Tissue Characterization Using the Continuous Wavelet Transform. Part II: Application on breast RF data, *IEEE Transactions on Ultrason., Ferroelect. Freq. Contr.* **48**(2) (2001), 364–372.

[39] K. Najarian, R. Splinter *Biomedical Signal and Image Processing*, CRC Press, (2006).

[40] R. Kucl, K. Haghkerdar, M. O'Donnel, Presence of Cepstral Peak in Random Reflected Ultrasound Signals, *Ultrasonic Imaging* **8**, 196–212, (1986).

[41] Z. Klimonda, *Obrazowanie parametryczne tłumienia fali ultradźwiękowej w tkance miękkiej*. Praca doctorska. IPPT, Warszawa, (2013).

[42] E. Kruglenko, B. Gambin, RF signal amplitude statistics during temperature changes in tissue phantoms, *Hydroacoustics*, **17**, 115–122, (2014).

[43] E. Kruglenko, A. Mizera, B. Gambin, R. Tymkiewicz, B. Zienkiewicz, J. Litniewski, Nagrzewanie ultradźwiękami tkanek miękkich in vitro i własności akustyczne wytworzonych wzorców tkanek miękkich, *59th Open Seminar on Acoustics, 2012-09-10/09-14, Boszkowo (PL)*, 129–132 (2012).

[44] V.P. Kuznetsov, Equations of Nonlinear Acoustics, *Akust. Zh.* **16**, 548–553 (1970).

[45] Ch.B. Machado, M. Meziri, G. Cortela, C.A. Negreira, W.C.A. Pereira. Continuous wavelet transform for tissue periodicity estimation: effect of noise and scatterers position variability. *Proceedings of the 22nd International Congress on Acoustics, Buenos Aires, September 5–9, 2016*, 10 p.

[46] G. Milton, *The Theory of Composites*, Cambridge University Press, (2002).

[47] S. Mallat, *A Wavelet Tour of Signal Processing*, Elsevier, (1999).

[48] Math. Graphics. *MATLAB* Programming. https://se.mathworks.com/products/matlab.html

[49] A. Mizera, B. Gambin, Stochastic modeling of the eukaryotic heat shock response, *Journal of Theoretical Biology*, **265**(3), 455–466, (2010).

[50] A. Mizera, B. Gambin, Modelling of ultrasound therapeutic heating and numerical study of the dynamics of the induced heat shock response, *Communication in Nonlinear Science and Numerical Simulation*, **16**)(5), 2342–2349, (2011).

[51] K.V. Mogatadakala, K.D. Donohuea, C.W. Piccoli, F. Forsberg, Detection of breast lesion regions in ultrasound images using wavelet sand order statistics, *J. Med. Phys.*, **33**(4), 840–849, (2006).

[52] M. Nakagami, The m-Distribution, a general formula of intensity of rapid fading. *In: William C. Hoffman, editor, Statistical Methods in Radio Wave Propagation: Proceedings of a Symposium held June 18-20, 1958*, 3–36, (1958).

[53] A. Nowicki, *Ultradźwięki w medycynie*. Warszawa. (2010).

[54] W.C.A. Pereira, S.L. Bridal, A. Coron, P. Laugier, Singular spectrum analysis applied to backscattered ultrasound signals from in vitro human cancellous bone specifimens, *IEEE Trans. Ultrason. Ferroelect. Freq. Contr.* **51** (3), 302–312, (2004).

[55] W.R. Pestman, I.B. Alberink, *Mathematical Statistics Problems and Detailed Solutions*, De Gruyter, (1998).

[56] H. Piotrzkowska-Wróblewska, *Wyznaczanie parametrów skóry ludzkiej in vivo za pomocą ultradźwięków wysokiej częstotliwości.* Praca doctorska. IPPT, Warszawa (2013).

[57] H. Piotrzkowska, J. Litniewski, E. Szymańska, A. Nowicki, *Ultrasonic Echosignal Applied to Human Skin Lesions Characterization*, *Archives of Acoustic*, **37**, 103–108, (2012).

[58] H. Piotrzkowska, J. Litniewski, E. Szymańska, M. Lewandowski, A. Nowicki *Statistics of envelope of high frequency ultrasound signal backscattered in human dermis*, Hydroascoustic, **13**, 205–214, (2010).

[59] Y. Povstenko Signalling problem for time-fractional diffusion-wave equation in a half-space in the case of angular symmetry, *Nonlinear Dyn.***59** 593–605, (2010).

[60] *Quantitative Ultrasound in Soft Tissues*, Ed. J. Mamou, M.L. Oelze, Springer, (2013).

[61] M. Ramaraj, S. Raghavan, A Survey of Wavelet Techniques and Multiresolution Analysis for Cancer Diagnosis, *International Conference on Computer, Communication & Electrical Technology*, 109–114, (2011).

[62] J. Rafiee, M.A. Rafiee, N. Prause, M.P. Schoen, Wavelet basis functions in biomedical signal processing, *Expert Systems with Applications*, **38**(5), 6190–6201, (2011).

drop

[63] J.M. Reid, F. Forsgber, E.J. Halpern, C.W. Piccoli, Molthen R.C., Shankar P.M., Goldberg B.B. Comparisons of the Rayleigh and K-distribution models using in vivo breast and liver tissue. Ultrasound Med. Biol., **24** (1), 93–100, (1998).

[64] O.A. Rosso, M.T. Martin, A. Figliola, K. Keller, A. Plastino, EEG analysis using wavelet-based information tools, *Journal of Neuroscience Methods*, **153** 163–182, (2006).

[65] N. Rubert, T. Varghese, Mean Scatterer Spacing Estimation in Normal and Thermally Coagulated Ex Vivo Bovine Liver, *Ultrasonic Imaging*, **36**(2), 79–97, (2014).

[66] N. Rubert, T. Varghese, Mean Scatterer Spacing Estimation Using Multi-Taper Coherence. *IEEE Trans Ultrason Ferroelectr Freq Control*, **60**(6), 1061–1073, (2013).

[67] S. Samko, A.A. Kilbas, O. Marichev *Fractional Integrals and Derivatives*, Taylor & Francis, (1993).

[68] N. Saiko, Basics of Analytic Signals. (2014) https://www.math.ucdavis.edu/ saito/courses/ACHA.w14/analytic_signal.pdf

[69] J. Sanii, N.M. Bilguta, Quantitative grain size evaluation using ultrasonic backscattered echoes, *J. Acoust. soc. Am.*, **80**(6), 1816–1824, (1986).

[70] P.M. Shankar A model for ultrasonic scattering from tissues based on K-distribution. *Phys. Med. Biol.*, **40**, 1633–1649, (1995).

[71] P.M. Shankar, A general statistical model for ultrasonic backscattering from tissues, *IEEE Transactions on Ultrasonics, Ferroelectrics, and Frequency Control*, **47**, No. 3, 727–736, (2000).

[72] L. Shenga, G. Wangb, F. Lic, J. Luoc, J. Liu, Ultrasound signal wavelet analysis to quantify the microstructuresof normal and frozen tissues in vitro, *Cryobiology*, **68**, 29-34, (2014).

[73] V.K. Sudarshan, M.R. Krishnan Mookiah, R. Acharya, V. Chandran, F. Molinari, H. Fujita, K.H. Ng Application of wavelet techniques for cancer diagnosis using ultrasound images: A Review *Computers in Biology and Medicine* **69** 97-111, (2016).

[74] X. Tang, U.R. Abeyratne, Wavelet transforms in estimating scatterer spacing from ultrasound echoes. *Ultrasonics*, **38**, 688–692, (2000).

[75] P.-H. Tsui, Y.-Ch. Shu, W.-Sh. Chen, H.-L. Liu, I.-T. Hsiao and Y.-T. Chien, Ultrasound temperature estimation based on probability variation ofbackscatter data, *J. Med. Phys.* **39** (5), 2369–2385, (2012).

[76] K.W.A. Van Dongenaand, M.D. Verweij, Sensitivity study of the acoustic nonlinearity parameterfor measuring temperatures during High IntensityFocused Ultrasound treatment, *Acoustics* 2615–2620, (2008).

[77] R.F. Wagner, S.W. Smith, J.M. Sandrik, and H. Lopez, Statistics of speckle in ultrasound B-scans, *IEEE Transactions on Sonics and Ultrasonics*, **30**(3), 156–163, (1983).

[78] K.R. Waters, M.S. Hughes, J. Moobley, J.G. Miller, Differential forms of the Kramers-Kr$\acute{}$ooning dispertion relations, *IEEE Translations on Ultrasonics, Ferroelectronics and Frequency Control*, **50**(1), 687–72, (2003).

[79] K.R. Waters, M.S. Hughes, J. Moobley, G.H. Brandenburger, and J.G. Miller. On the applicability of Kramers-Kr$\acute{}$ooning relations for ultrasonic attenuation obeying a frequency power low, *J. Acoust. Soc. Am.* **108**, 556–563, (2000).

[80] D.R. Wijayaa, R. Sarnoa, E. Zulaikac, Information Quality Ratio as a novel metric for mother wavelet selection *Chemometrics and Intelligent Laboratory Systems*, **160**, 59–71, (2017).

[81] J. Wójcik, Conservation of energy and absorbtion in acoustic fields for linear and nonlinear propagation. *J. Acoust. Soc. Am.*, **104**(5), 2654–2663, (1998).

[82] Analyze and synthesize signals and images using wavelets, *WaveToolbox*, https://www.mathworks.com/products/wavelet.html

[83] J.A. Zagzebski, J.-F. Chen, F. Dong, Th. Wilson, Intervening Attenuation Affects First-order Statistical Properties of Ultrasound Echo Signals, *IEEE Translations on Ultrasonics, Ferroelectrics, and Frequency Control*, **46**(1), 35–40. (1999).

[84] E. Zelianko, S.L. Voskresensky, O. Doubrovina, S. Rogosin, The method of determining the chronic distress of the fetus in the antenatal period: patent BY 9249, C1 2007.04.30.

[85] N. Żołek, J. Wójcik, Optimized Acoustic Echoes Simulator in Fourier domain, IUS 2017, *IEEE International Ulltrasonics Symposium*, 2017-09-06/09-09, Washington (US), DOI: 10.1109/ULTSYM.2017.8092654, 1–3, (2017).

[86] Z. Zhou, W. Wu, S. Wu, K. Jia, P. H. Tsui A Review of Ultrasound Tissue Characterization with Mean Scatterer Spacing. *Ultrasonic Imaging*, **39**, Issue 5, 263–282, (2017).

Appendix A.
Theory of Wavelet Transforms

Integral Wavelet Transform

A function $\psi(x)$ is called a *wavelet* if it obeys the following conditions:

$$\int_{-\infty}^{+\infty} |\psi(x)|^2 dx < \infty, \tag{A.1}$$

$$C_\psi = \int_{-\infty}^{+\infty} \frac{|\hat{\psi}(\omega)|^2}{|\omega|} d\omega < \infty, \tag{A.2}$$

where $\hat{\psi}(\omega) = \int_{-\infty}^{\infty} \psi(t) \exp^{-i2\pi\omega t} dt$ is a Fourier transform of the function $\psi(x)$. As the condition (A.1) means that $\psi \in L_2(\mathbb{R})$ (i.e. it and its square are integrable), it also means that $\hat{\psi}(x)$ exists and is called a finite energy condition. Equation (A.2) is called and admissibility condition, its sense is that in the wavelet function at zero frequency component should satisfy the equality $\hat{\psi}(0) = 0$ or should have zero mean value in the other case. The constant C_ψ is called wavelet admissible constant and is often used as a normalizing coefficient for the integral and discrete wavelet transforms.

The *continuous wavelet transform* for the function $f(x) \in L_2(\mathbb{R})$ can be represented by means of wavelet function $\psi(x)$ as follows

$$W_\psi(a,b) = \frac{1}{C_\psi} \int_{-\infty}^{\infty} f(x) \overline{\psi\left(\frac{x-b}{a}\right)} dx, \tag{A.3}$$

where $a \in (-\infty, 0) \bigcup (0, \infty)$ is a scale parameter and $b \in (0, \infty)$ is a shift parameter, $\overline{\psi}$ is a complex conjugate to the function ψ and C_ψ is the admissible constant defined in (A.2) (see e.g. [3]). Usually it is taken $C_\psi = \frac{1}{a}$ or $C_\psi = \frac{1}{\sqrt{a}}$, we will consider the second equality. In the space $L_2(\mathbb{R})$ there is the inverse wavelet transform defined by equation

$$f(x) = \frac{1}{C_\psi} \int_{-\infty}^{+\infty} \int_{0}^{+\infty} (W_\psi)(a,b) \psi\left(\frac{x-b}{a}\right) \frac{dadb}{a^2}. \tag{A.4}$$

Multiresolution Analysis

The construction of orthogonal wavelet bases is on the concept of multiresolution analysis (MRA) [27]. In this case special families of wavelets ψ_{ji} such that $\langle \psi_{ji}, \psi_{lk} \rangle = \delta_{jl}\delta_{ik}$, where $\langle \cdot, \cdot \rangle$ denotes a scalar product and δ is the Kronecker symbol, are considered. This means that the wavelets ψ_{ij} are orthogonal with respect to their shifts by discrete steps b_j and their scaled versions by discrete steps a_j. In this case the formula (A.3) is exact with $C = 1$ and $R(x) = 0$.

The idea of the application of discrete orthogonal wavelet transform is to consider the approximations f_j of the signal $f(x)$ at different scales j. This allows to pass from the approximation f_j to the higher resolution approximation f_{j+1} and to encode the difference between the approximation into the wavelets.

The filter is constructed with the help of scaling functions which are paired to each wavelet functions. The scaling function $\phi(x)$ is normalized, i.e. $\int_{-\infty}^{\infty} \phi(x)dx = 1$. The set of functions ψ_{jk} consists of scaled and dilated modifications of the function ϕ:

$$\phi_{ji}(t) = 2^{j/2}\phi\left(2^j t - i\right).$$

The basis $\phi_{ji} \in L_2(\mathbb{R})$ is orthonormal at a given scale j with respect to its translations by the step $\dfrac{i}{2^j}$

$$\langle \phi_{ij}, \phi_{jk} \rangle = \delta_{jk}.$$

In general the explicit expression for the scaling function does not exist but it may be constructed be means of the refinement equation

$$\phi_{j-1,i}(x) = \sum_{n=-\infty}^{\infty} h_{n-2i}\phi_{jn}(x), \tag{A.5}$$

where $h_i = \langle \phi_{ji}\phi_{j-1,0} \rangle$.

The corresponding wavelet function ψ is a linear combination of the scaling function ϕ

$$\psi_{ji}(x) = \sum_{n=-\infty}^{\infty} g_{n-2i}\phi_{jn}(x)$$

with coefficients $g_n = \langle \phi_{jn} \phi_{j-1,0} \rangle$ which also may be calculated from the filter coefficients h_k be means of the relation $g_n = (-1)^{1-n} h_{1-n}$, which also may be written in the form

$$\psi_{j,k} = 2^{j/2} \psi \left(2^j x - k \right). \tag{A.6}$$

Then wavelet and a scaling function are connected by the following relations

$$\begin{aligned} \phi(x) &= \sqrt{2} \sum_k h_k \phi(2x - k), \\ \psi(x) &= \sqrt{2} \sum_k g_k \phi(2x - k), \end{aligned} \tag{A.7}$$

the coefficients h_k and g_k are calculated from the following system of equities:

- the orthogonality of the scaling functions

$$\sum_k h_k h_{k+2m} = \delta_{0,m}, \tag{A.8}$$

- the orthogonality of the scaling and wavelet functions

$$\sum_k h_k g_{k+2m} = 0, \tag{A.9}$$

- the condition which is derived from the refinement condition (A.5) in this case

$$\sum_k (-1)^k h_k = 0, \tag{A.10}$$

- the condition for M vanishing moments

$$g_k = (-1)^k h_{2M-k-1} \tag{A.11}$$

- the normalization condition

$$\sum_k h_k = \sqrt{2}. \tag{A.12}$$

For any chosen wavelet family, i.e. for the known functions $\phi(x)$ and $\psi(x)$, the coefficients h_k and g_k can be found and the approximation and reconstruction for the given function f can be obtained.

Let us denote $\overline{f}_{ji} = \langle f, \phi_{ji} \rangle$, $\tilde{f}_{ji} = \langle f, \psi_{ji} \rangle$. Then for the level N with respect to the scale k we will obtain the approximation formula

$$f_k(x) = \sum_{i=-\infty}^{+\infty} \overline{f}_{ki} \phi_{ki}(x) + \sum_{j=k}^{N} \sum_{i=-\infty}^{+\infty} \tilde{f}_{ji} \psi_{ji}(x). \tag{A.13}$$

In discrete case any function that is integrable with its square may be presented in a form

$$f(x) = \sum_{k} a_{j_n} \phi_{j_n,k} + \sum_{j \geq j_n} d_{j_n,k} \psi_{j_n,k} \tag{A.14}$$

with wavelet functions $\psi_{j,k}$ and scaling functions $\phi_{j,k}$. Amplitude coefficients a_k and detail coefficients d_k are calculated. Formula (A.14) represents the wavelet decomposition of $f(x)$ up to the level j_n.

Signal's decomposition at 0-level represents the signal itself, the next levels show the approximation of the signal. The more level number gives the less exact signal but there is the possibility of filtering, denoising and compression [47].

Appendix B.
Wave Propagation in Random Medium

Mathematical Model

Let (Ω, Σ, μ) be probability space, where Σ is a complete σ-algebra, μ is the probability measure. Assume that Ω is acted on by an *n-dimensional dynamical system* $T(x) : \Omega \to \Omega$, such that for each $\mathbf{x} \in \mathbb{R}^n$, both $T(\boldsymbol{x})$ and $T(\boldsymbol{x})^{-1}$ are measurable, and such that:

- $T(\mathbf{0})$ is the identity map on Ω and for $\boldsymbol{x}_1,\ \boldsymbol{x}_2 \in \mathbb{R}^n,\ \ T(\boldsymbol{x}_1+\boldsymbol{x}_2) = T(\boldsymbol{x}_1)T(\boldsymbol{x}_2)$;
- for each $\boldsymbol{x} \in \mathbb{R}^n$ and measurable set $F \in \mathcal{F}$, $\mu(T(\boldsymbol{x})^{-1}F) = \mu(F)$, i.e., μ is an invariant measure for T;
- for each $F \in \Sigma$, the set $\{(\boldsymbol{x}, \omega) \in \mathbb{R}^n \times \Omega \,|\, T(\boldsymbol{x})\omega \in F\}$ is a $d\boldsymbol{x} \times d\mu$ measurable subset of $\mathbb{R}^n \times \Omega$, where $d\boldsymbol{x}$ is the Lebesgue measure on $\mathbb{R}^n$. $T(\boldsymbol{x})^{-1} = T(-\boldsymbol{x})$. So we may consider dynamical system as system *with measure preserving flow.*

Stationary Random Process

Random homogeneous fields, starting from the random variable $f \in L^1(\Omega)$,

$$\tilde{f}(\boldsymbol{x}, \omega) \equiv f(T(\boldsymbol{x})\omega).$$

where $\tilde{f}$ is the statistically homogeneous (i.e. stationary) random process. *Statistical homogeneity* means that two geometric points of the space are *statistically indistinguishable*, the statistical properties of the medium invariant under the action of translations.

A group $\{U(\boldsymbol{x}) : \boldsymbol{x} \in \mathbb{R}^n\}$ of isometries on $L^2(\Omega) = L^2(\Omega, \Sigma, \mu)$ defined by $(U(\boldsymbol{x})f)(\omega) = f(T(\boldsymbol{x})\omega),\ \boldsymbol{x} \in \mathbb{R}^n, \omega \in \Omega,\ f \in L^2(\Omega)$. The function $\boldsymbol{x} \to U(\boldsymbol{x})$ continuous in the strong topology, i.e., for each $f \in L^2(\Omega),\ U(\boldsymbol{x})f \to f$ strongly in $L^2(\Omega)$ as $\boldsymbol{x} \to 0$. The strong convergence holds provided that the probability space is separable. A dynamical system is *ergodic*, if every invariant function, i.e. satisfying $f(T(\boldsymbol{x})\omega) = f(\omega)$, is *constant* almost everywhere in Ω.

Statistically periodic media

Statistically periodic media are modelled by a probability space (Ω', Σ', μ') on which acts a measure preserving $\mathbb{Z}^n$ is group $T'(\boldsymbol{z}),\ \boldsymbol{z} \in \mathbb{Z}^n$, which is a set of bijective maps from Ω into itself satisfying the group property in $\mathbb{Z}^n$ and the following invariance property:

$$\forall \boldsymbol{z} \in \mathbb{Z}^n, \forall F \in \Sigma',\ T'(-\boldsymbol{z})F = \{\omega T'(-\boldsymbol{z})\omega \in F\}$$

and $\mu'(T'(\boldsymbol{z})F) = \mu'(F)$, $\mathbb{Z}$ is the set of integers.

A statistically periodic medium is ergodic if constants are the only real random variables such that:

$$\forall \boldsymbol{z} \in \mathbb{Z}^n,\ f \circ T'(\boldsymbol{z}) = f \text{ a. s. (almost surely).}$$

Statistically periodic media is a special case of statistically homogeneous media. Indeed, it suffices to take $\Omega = \Omega' \times Y$ with $Y = [0,1)^n$, Σ to be $\Sigma' \otimes \mathcal{L}(Y)$, the completion with respect to $\mu = \mu' \otimes d\boldsymbol{y}$ of the σ-algebra product of Σ' and Borel σ-algebra on Y. Now $T(\boldsymbol{x})$ defined by:

$$\forall \boldsymbol{x} \in \mathbb{R}^n,\ \forall\, \omega' \in \Omega',\ \forall \boldsymbol{y} \in Y,\ T(\boldsymbol{x})(\omega', \boldsymbol{y}) = (T'[\boldsymbol{x}+\boldsymbol{y}]\omega', \boldsymbol{x}+\boldsymbol{y}-[\boldsymbol{x}+\boldsymbol{y}])$$

is a measure preserving flow on (Ω, Σ, μ); moreover, the medium is ergodic if and only if T' is ergodic.

Periodic and quasiperiodic media

Periodic media is a special case of statistically homogeneous ergodic media. Y is the set $Y = [0,1)^n$ (the unit basic cell), whilst Σ and μ are the Borel σ-algebra and Lebesgue measure on Y, respectively. Then $T(\boldsymbol{x})$ acts on Y as follows

$$\forall \boldsymbol{x} \in \mathbb{R}^n,\ \boldsymbol{y} \in Y,\ \ T(\boldsymbol{x})\boldsymbol{y} = \boldsymbol{x} + \boldsymbol{y} - [\boldsymbol{x} + \boldsymbol{y}],$$

where $[\boldsymbol{x}]$ is the integer part of $\boldsymbol{x}$.

In this particular case, a random variable is identified with a measurable map on Y, $\tilde{f}$ is identified with the periodic continuation of f to the whole space whilst the expectation is identified to the volume average on Y and $d\mu = d\boldsymbol{y}$.

Quasiperiodic media $\Omega = \mathbf{T}^m,\ m > n$ is an m-dimensional torus endowed with the Lebesgue measure. To define the dynamical system $T(\boldsymbol{x})$ we fix an $(m \times n)$-matrix $\boldsymbol{\Lambda} = (\Lambda_{ij})$ and set

$$T(\boldsymbol{x})\omega = \omega + \boldsymbol{\Lambda}\boldsymbol{x} \mod \mathbb{Z}^n.$$

The map $T(\boldsymbol{x})$ preserves the measure μ. For $T(\boldsymbol{x})$ to be ergodic, it is necessary and sufficient that $\boldsymbol{\Lambda k} \neq \mathbf{0}$ for any $\boldsymbol{k} \in \mathbb{Z}^n,\ \boldsymbol{k} \neq \mathbf{0}$. Any measurable function f on Ω may be identified with a unique measurable 1-periodic function on $\mathbb{R}^n$. However, in this case we have a lot of essentially different realizations $f(\omega + \boldsymbol{\Lambda}\boldsymbol{x})$. Realizations of this type are called *quasiperiodic functions*, if $f(\omega)$ is continuous.

Waves in randomly inhomogeneous medium

The wave propagation in randomly inhomogeneous medium is described by the equation **??** where the spatially fluctuating coefficients are random fields, i.e. functions $\mu(\mathbf{r}, \omega)$ and $\gamma(\mathbf{r}, \omega)$ depend on $\omega \in \Omega$ and Ω is a probability space. If we assume that pressure has harmonic time dependency, i.e. $p(t) = pe^{iw_0 t}$, and w_0 denotes an angular frequency, we get:

$$\left(\nabla^2 + k_0^2\right) p + \frac{\partial}{\partial x_i}\left(\frac{\rho_0}{\rho} - 1\right)\frac{\partial}{\partial x_i} p + \hat{\omega}^2 \frac{\rho_0}{K_0}\left(\frac{K_0}{K} - 1\right) p = 0,$$

where $k_0^2 = \dfrac{\omega - 0^2\rho_0}{c_0^2}$, where c_0 speed of sound in a homogeneous medium

Abbreviated notion is introduced as follows.

$$L \equiv L_0 + L_1^\omega + L_2^\omega, \text{and } \mathrm{Lp} = 0,$$

where

$$L_0 \equiv \left(\nabla^2 + k_0^2\right)$$
$$L_1^\omega \equiv \nabla \cdot (\mu^\omega(\mathbf{x})\nabla(\mathbf{x})),$$
$$L_2^\omega \equiv \gamma^\omega(\mathbf{x})$$

where $\omega \in (\Omega, \Sigma, P)$ is probability space. If the incident wave p^i is assumed to be a plane wave and assuming that $p = p^i + p^s$, we the equation for p^s reads as (cf. equation 1.16):

$$p^s(\omega, \cdot) = L_o^{-1}\left(L_1^\omega + L_2^\omega\right)\left(p^i(\cdot)\right)$$

This equation relates the randomness of the medium with the randomness of the scattered signals. Principally if we know right hand side of the above equation we can approximate the randomness of the scattered field. But what it means "to know" the randomness? It is clear that one has only some information about the random fields, there are no explicit formulae, information is given at least by the infinite numbers of moments. So, to find answer to the inverse problem: how the known randomness of the scattered field is related to the randomness of random media is even more complicated problem, cf. short introduction to this problem given in [25]. This is our own version of explanation the decision why there should be used the numerical methods and try to get an "approximatly answer" to the question of quantifying random properties of the medium from scattered acoustic signals.

Appendix C.
Papers and background of PhD student

Cooperation and Grant

1. The co-operation agreement between Belarussian State University and Institute of Fundamental Technological Research of Polish Academy of Sciences.

2. National Science Center of Poland, research project 2011/03/D/ST7/03347.

List of Publications in Cooperation with IPPT

Papers in Scientific Journals

1. B. Gambin, **O. Doubrovina**, Statistical properties of wavelet transform coefficients of backscattering signal from soft tissues and their phantoms *Hydroacoustics*, **16**, 59–66 (2013).

2. **O. Doubrovina**, B. Gambin, E. Kruglenko, Temperature level and properties of wavelet approximations of backscattered ultrasound. *Hydroacoustics*, **17**, 37–46 (2014).

3. **O. Doubrovina**, B. Gambin, J Wòjcik, Detection of variations in random characteristics of scattering medium by the wavelet analysis, 10th EAA International Symposium on Hydroacoustics, May 17-20, 2016, Jastrzebia Gora, Poland. *Archives of Acoustic* **41**, No 2, p. 360 (2016).

4. B. Gambin, J. Wòjcik, **O. Doubrovina**, Differentiation of random structure properties using wavelet analysis of backscattered ultrasound. *Hydroacoustics*, **19**, 121–128 (2016).

5. B. Gambin, M. Byra, E. Kruglenko, A. Nowicki, **O. Doubrovina**, Ultrasonic measurement of temperature rise in breast cyst and in surroundings regions *Archives of Acoustic* **41**(4), 791–798 (2016).

Chapters of Books

1. B. Gambin, **O. Doubrovina**, Wavelet analysis for temperature increase detection from acoustic backscattered signal. In: Complex Analysis and Potential Theory with Applications (T. Aliev Azerogly, A. Golberg, S.V. Rogosin Eds.). Cambridge Scientific Publishers, 63–76 (2014).

2. **O. Doubrovina**, R. Tymkiewicz, H. Piotrzkowska-Wròblewska, B. Gambin Linking of structural parameters to properties of ultrasound backscattered signals by the threads phantoms study, Aktualnoci Inżynierii Akustycznej i Biomedycznej, Polskie Towarzystwo Akustyczne, Oddzia w Krakowie, Red. K. Suder-Dębska, Krakw, 67–79 (2018).

Conference Abstracts and Proceedings

1. Gambin B., **Doubrovina O.**, Litniewski J., Piotrzkowska H. Wavelet approach for skin tussue in-vivo analysis, *Abstracts of the 7th International Conference "Analytic Methods of Analysis and Differential Equations" (AMADE-2012), Minsk, Belarus, 10–14 September 2012*, p. 21 (2012).

2. Gambin B., **Doubrovina O.**, Wavelet approach for the problems of discerning samples obtaining from acoustic measurements // *Abstracts of 9th International ISAAC Congress, August 5-9, 2013 Krakow, Poland*, p. 74.

3. **O. Doubrovina**, J. Litniewski, B. Gambin, Wavelet approximation and statistical approach to random fluctuations of amplitude in backscattered ultrasonic signal. *Forum Acousticum, Sept. 7–12, 2014, Krakow, 2014*, 205–206 (2014).

4. B. Gambin, M. Byra, **O. Doubrovina**, Nonparametric statistics in indirect temperature estimation by ultrasound imaging. *Abstracts of reports of the 8th international scientific seminar, Abstracts of the 9th International Workshop "Analytic Methods of Analysis and Differential Equations" (AMADE-2015), Minsk, Belarus, 14–19 September 2015*, p. 25 (2015).

5. J. Wójcik, B. Gambin, **O. Doubrovina**, Randomness characteristics of scattering medium by the wavelet analysis. *Abstracts of*

the 3rd International Workshop "Boundary Value Problems, Functional Equations and Applications", Rzeszow, Poland, April 20–23, 2016, p. 64 (2016).

6. **O. Doubrovina**, B. Gambin, H. Piotrzkowska-Wròblewska, The backscattered ultrasound signal wavelet decomposition applied to recognize of regular positioning of scatterers in a sonicated medium. *Materials of the 9th Internationall Workshop "Analytic Methods of Analysis and Differential Equations" (AMADE-2018), Minsk, Belarus, September, 17–21, 2018*, 64–65 (2018).

7. B. Gambin, **O. Doubrovina** A new index of non-periodicity degree of the scattering media structure based on the ultrasonic backscattered RF signals multiresolution analysis *Archive of Acoustics*, **44**(2), p. 405, (2019).

Conference Reports

1. *Cardiotocographical study of the fetal condition: from the wavelet analysis to a new diagnostic model*, Seminar of Ultrasound Department, IPPT, Warsaw, January, 2011.

2. *Viscosity and non-classical absorption of soft tissue described by fractional derivatives* (with B. Gambin), 31th International Symposium "Acoustical Imaging", Warsaw, April, 10–13, 2011.

3. *Wavelet approach for skin tissue in-vivo analysis* (with B. Gambin, J. Litniewski, H. Piotrzkowska), International Conference "Analytic Methods of Analysis and Differential Equations" (AMADE-2012), Minsk, Belarus, September, 10–14, 2012.

4. *Wavelet approach to RF signals for structural characterization of soft tissue phantom* (with B. Gambin), 59th Open Seminar on Acoustic, Poznan-Boszkowo, Poland, September, 10–14, 2012.

5. *Analysis of the backscattered signal from pulse/echo ultrasound in tissue mimicking phantoms utilizing statistical properties of wavelet transform coefficients* (with B. Gambin), XX Conference of Acoustic and Biomedical Engineering, Krakow-Zakopane, April, 15-19 2013.

6. *Statistical properties of wavelet transform coefficients of backscattering signal from soft tissues and their phantoms* (with B. Gambin, E. Kruglenko), XXX Symposium on Hydroacoustics, Gdansk-Gdynia, May, 13–16, 2013.

7. *Wavelet analysis for temperature increase detection from acoustic backscattered signal* (with B. Gambin), 9th ISAAC Congress, August 5–9, 2013.

8. *Temperature level and properties of wavelet approximations of backscattered ultrasound*, XXXI Symposium on Hydroacoustic, Świnoujście, May, 12–16, 2014.

9. *Wavelet approximation and statistical approach to random fluctuations of amplitude in backscattered ultrasonic signal*, 7th Forum Acusticum 2014, Krakow, September, 7–12, 2014.

10. *Nonparametric statistics in indirect temperature estimation by ultrasound imaging*, International Conference "Analytic Methods of Analysis and Differential Equations" (AMADE-2015), Minsk, Belarus, September, 14–19, 2015.

11. *Randomness characteristics of scattering medium by the wavelet analysis* , (with B. Gambin, J. Wójcik), 3rd International Workshop "Boundary Value Problems, Functional Equations and Applications" (BFA-2016), Rzeszów, April, 19–23 2016.

12. *Detection of variations in random characteristics of scattering medium by the wavelet analysis* (with B. Gambin, J. Wójcik), 10th EAA International Symposium on Hydroacoustics, Jastrzębia Góra, May, 7–10, 2016.

13. *Wavelet analysis of ultrasonic signals in soft tissue structure differentiation* Seminar of Ultrasound Department, IPPT, Warsaw, November, 20, 2017.

14. *Linking of structural parameters to properties of ultrasound backscattered signals by the threads phantoms study* (with R. Tymkewicz, H. Piotrzkowska-Wróblewska, B. Gambin), XXII Conference on Acoustic and Biomedical Engineering, April, 10–13, 2018.

15. *The backscattered ultrasound signal wavelet decomposition applied to recognize of regular positioning of scatterers in a sonicated medium* (with B. Gambin, H. Piotrzkowska-Wróblewska), International Workshop "Analytic Methods of Analysis and Differential Equations" (AMADE-2018), Minsk, Belarus, September, 17–21, 2018.

16. *Wavelet analysis of ultrasonic signals in soft tissue structure characterization* W. Olszaks and A. Sawczuks Mechanics Seminar of Institute of Fundamental Technological Research, Warsaw, February, 28, 2019.

17. *A new index of non-periodicity degree of the scattering media structure based on the ultrasonic backscattered RF signals multiresolution analysis* (with B. Gambin), International Symposium on Fluid Acoustics, Sopot, May, 20–22, 2019.